

NONLINEAR AMPLIFICATION AND GENERATION OF VERY
LOW FREQUENCY WAVES IN THE NEAR-EARTH SPACE
ENVIRONMENT

A DISSERTATION
SUBMITTED TO THE DEPARTMENT OF ELECTRICAL
ENGINEERING
AND THE COMMITTEE ON GRADUATE STUDIES
OF STANFORD UNIVERSITY
IN PARTIAL FULFILLMENT OF THE REQUIREMENTS
FOR THE DEGREE OF
DOCTOR OF PHILOSOPHY

Justin D. Li
July 2015

© Copyright by Justin D. Li 2015
All Rights Reserved

I certify that I have read this dissertation and that, in my opinion, it is fully adequate in scope and quality as a dissertation for the degree of Doctor of Philosophy.



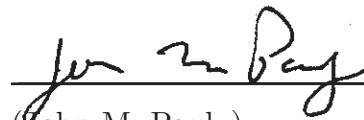
(Umran S. Inan) Principal Adviser

I certify that I have read this dissertation and that, in my opinion, it is fully adequate in scope and quality as a dissertation for the degree of Doctor of Philosophy.



(Maria Spasojevic)

I certify that I have read this dissertation and that, in my opinion, it is fully adequate in scope and quality as a dissertation for the degree of Doctor of Philosophy.



(John M. Pauly)

Approved for the Stanford University Committee on Graduate Studies

Abstract

Whistler-mode waves are intense electromagnetic radio waves that are known to be key drivers of energetic particle dynamics in the Earth’s radiation belts. Despite many decades of active research, fundamental questions still remain concerning the interaction of whistler-mode waves with energetic electrons, especially in regard to nonlinear phenomena including wave amplification. The Siple Transmitter Experiment, which operated in Antarctica from 1973 to 1988, provided researchers a rare opportunity to perform controlled experiments on nonlinear wave-particle interactions. Very low frequency waves in the few kilohertz range radiated by the transmitter at Siple Station propagate into the magnetosphere where they interact with energetic electrons. The interactions modify the waves, amplifying them and generating new frequency components. The modified waves are then observed with radio receivers on the ground at the magnetic conjugate point in the northern hemisphere. The Siple Experiment produced many new and fascinating observations of wave-particle interactions; however, during the experiment, available data analysis tools allowed for only a fraction of the data collected to be analyzed. Moreover, theoretical understanding of the physical processes driving the interactions was limited at the time.

We present statistical analysis of data collected in 1986 from the Siple Experiment to quantify nonlinear growth rates and total nonlinear growth of very low frequency waves injected into the magnetosphere, which are useful for bounding theoretical discussion and numerical simulation of wave-particle interactions. We consider a specific amplification phenomenon, termed preferential magnetospheric amplification, by quantifying the preferential effect of injected rising versus falling swept-frequency waves and by examining the theoretical mechanism involved using a Vlasov-Maxwell

numerical simulation. The modeling efforts, validated by the data, reveal that the total amplification depends on the linear growth rate and the onset and duration of nonlinear growth, which for typical hot plasma parameters favors injected rising swept frequency waves. In addition to the amplification process, wave-particle interactions can also generate new very-low frequency waves called triggered emissions. These triggered emissions have not been yet well characterized and pose significant challenges for theoretical interpretation and numerical modeling. We present a comprehensive description of triggered emission behavior observed in 1986 by quantifying time and frequency changes and demonstrating the significant dependence of the emission behavior on the frequency-time format of the injected signal. The triggered emission characteristics can be used to evaluate the validity of current numerical models and provide a framework for describing wave behavior in the magnetosphere. Finally, we demonstrate the application of modern machine learning techniques for predicting observations of transmissions from the Siple experiment as a suggested approach to further study of the large sets of data in the field of space physics.

Acknowledgments

There are many people whose support and guidance were crucial for this dissertation. First of all, I would like to thank my advisor, Professor Umran S. Inan for the opportunities I have had here at Stanford in studying the Siple data and for his keen insights and thoughts regarding scientific challenges available in the data. Second, I would like to thank Dr. Maria Spasojevic for all of her advice and for her willingness to answer any of my questions and for her weekly meetings with me, lending her experienced perspective to my research results and to writing and revising my manuscripts for publication. And third, I would also like to thank an additional number of mentors who shared their insight and wisdom with me, in particular Professor Morris Cohen at Georgia Tech and Professor Mark Golkowski at CU Denver for encouragement and counsel in my work and career and also Dr. Timothy Bell and Professor Don Carpenter for their long experience in the field and the fascinating historical and scientific knowledge they have imparted to me. I would also like to thank Professor Umran S. Inan and Professor Morris Cohen for the chance to travel for field work for the group to Oklahoma, Alaska, and Antarctica. Finally, I would like to thank Dr. Bob Marshall and Dr. Ivan Linscott for their advice and encouragement, insights and comments, and their always open doors.

My time at Stanford has also been supported tremendously by the staff members in the VLF group, and I would like to thank our group administrators, Helen Niu and Shaolan Min, for all of their dedicated administrative work and for making sure all of our forms and reimbursements were processed on time. Although I did not travel on field work for my own research, the field work was an incredible experience and so I would like to thank our lab manager and engineering, Jeff Chang, for his support and

guidance on preparing and carrying out my field work. Finally, I would like to extend my sincere thanks to our data manager, Dan Musetescu, for all of his work receiving, archiving, and organizing all of the data generated at our field sites and especially for his trips to our data warehouse on the hills of the Stanford Dish in order to digitize the magnetic tapes containing the Siple data.

These five years at Stanford have also been considerably richer because of my colleagues, friends, and compatriots in the VLF group. I would like to thank Fadi Zoghzoghy, Rasoul Kabirzadeh, Patrick Blaes, Austin Sousa, Chris Young, Kevin Graf, George Jin, Naoshin Haque, Forrest Foust, and Dan Golden, Drew Compston, and Salman Naqvi for being part of my time here in the VLF group at Stanford. And, I am particularly grateful to Vijay Harid for his early work on the Siple data and all of his theory and modeling work that complemented my own work, and I am especially grateful for his efforts and time spent explaining the theory and his simulations to me. I would also like to thank the undergraduate students who worked with me in our group as REUs, Blane Wilson, Dominic Delgado, Jonathan Wilkins, Cedric Yue, Adekunle Awojinrin, and Josh Lauderdale.

Given the historical component of this work, I would also like to thank the many predecessors who worked at Siple and on Siple data in whose path I have followed. Furthermore, I would like to thank Dr. Paul Kossey for his support in helping make this work and dissertation possible.

Finally, I want to thank the community I've experienced here at Stanford in the InterVarsity Graduate Christian Fellowship and my church community of Chinese for Christ Church of San Jose for their helping me to persevere through graduate school. And especially and most importantly, I want to thank my family, my parents, Alice and John, and my brother, James, for their loving encouragement and support.

JUSTIN D LI
Stanford, California
July 2015

This research has been supported by the Air Force Research Laboratory through award FA9453-11-C-0011 to Stanford University.

Contents

Abstract	iv
Acknowledgments	vi
1 Introduction	1
1.1 The Near-Earth Space Environment	2
1.1.1 The Plasmasphere	3
1.1.2 The Radiation Belts	4
1.1.3 Whistler-Mode Electromagnetic Waves	4
1.2 Whistler-Mode Wave Injection Observations	9
1.2.1 Early Experiments	10
1.2.2 Siple Station	11
1.2.3 Later Experiments	13
1.3 Thesis Organization	14
1.4 Scientific Contributions	15
2 Scientific Background	17
2.1 Experimental Review	17
2.1.1 Related Past Work	18
2.1.2 Other Interesting Phenomenon	22
2.2 Theoretical Background	28
2.2.1 Plasma Theory	28
2.2.2 Numerical Approaches to Wave-Particle Interactions	30
2.2.3 Other Theory	32

2.3	Experimental Archival Challenges	35
2.3.1	Original Experimental Setup	35
2.3.2	Archival Challenges and Digitization	36
2.3.3	Timing Correction and Alignment	39
2.3.4	Transmission Log Transcription	41
3	Characteristics of ELF/VLF Wave Amplification	44
3.1	The Mini-Diagnostic (MDIAG) Format	45
3.2	Reception Statistics	47
3.3	Amplification Statistics	48
3.4	Discussion	55
3.5	Conclusions	60
4	The Preferential Amplification Phenomenon	62
4.1	Statistical Observations of Preferential Amplification	63
4.2	Theory and Modeling of Preferential Amplification	66
4.2.1	Numerical Model	69
4.3	Conclusions	73
5	Observational Behavior of Triggered Emissions	75
5.1	Past Observations and Modeling Efforts	76
5.2	The 1986 MDIAG and STACO Data Set	78
5.3	Statistical Characterization of Triggered Emissions	84
5.4	Discussion and Model Validation	93
5.5	Conclusions	99
6	Predicting Conditions for Siple Receptions	101
6.1	Machine Learning Techniques for Prediction of Receptions	104
6.2	Classification Methodologies	105
6.2.1	The MDIAG Data Set	105
6.2.2	Naive Bayes with Laplace Smoothing	107
6.2.3	Support Vector Machines	107

6.3	Classification Results	108
6.4	Conclusions	111
7	Conclusions and Suggestions for Future Work	112
7.1	Summary of Contributions	112
7.2	Suggestions for Future Work	114
A	1986 Data Spectrograms	116
A.1	Mini-Diagnostic (MDIAG) Data	116
A.2	Staircase Coherence (STACO) Data	123
B	Spectral Forms of Triggered Emissions	129
B.1	Riser	129
B.2	Faller	129
B.3	Hooks	132
B.4	Band-Limited Impulse (BLI)	132
B.5	Early Riser	133

List of Tables

3.1	1986 MDIAG Reception Statistics	48
5.1	Table of MDIAG and STACO Triggered Emission Counts in 1986 . .	82
5.2	Table of MDIAG and STACO Triggered Emission Frequency Behavior in 1986	94
6.1	Confusion Matrix Results of Bayesian and SVM Reception Classifiers	109

List of Figures

1.1	The Earth's Inner Magnetosphere	3
1.2	The Plasmasphere	4
1.3	The Radiation Belts	5
1.4	Wave-Particle Interactions under Resonance	6
1.5	CLUSTER Wide Band Chorus Example	7
1.6	Controlled Wave Injection Experimental Setup	8
1.7	Example of Transmission and Reception	9
1.8	Early Observations of Triggered Emissions	11
1.9	Siple Station, Antarctica	12
1.10	HAARP	14
2.1	Original Experimental Setup of the Siple Station Experiment	36
2.2	Archived Magnetic Tapes of Siple Data	37
2.3	Extent of Digitized Siple Transmitter Experiment Data	38
2.4	Demonstration of Timing Correction Results	42
2.5	Typewritten 1986 Siple Transmission Logs	43
3.1	MDIAG Format Example	46
3.2	MDIAG Superposed Epoch Kp Analysis	49
3.3	General and Subset 1 Amplification Characteristics	51
3.4	General Amplification Comparisons	53
3.5	Histograms of Nonlinear Growth Rates and Total Growth	54
3.6	Subset 1 Amplification Comparisons	56
3.7	Examples with and without Hiss	58

3.8	Nonlinear Growth Rate Dependence on Kp	59
4.1	STACO Format and Example Observations	64
4.2	STACO Preferential Amplification Statistics	67
4.3	STACO Numerical Simulations and Theoretical Interpretation	72
5.1	MDIAG Spectrogram Examples with Triggered Emissions and Summary Plots of MDIAG Triggered Emissions by Element	78
5.2	STACO Spectrogram Examples with Triggered Emissions and Summary Plots of STACO Triggered Emissions by Element	83
5.3	Triggered Emission Density 2-D Histogram	85
5.4	MDIAG Triggered Emission Frequency Change and Sweep Rate	87
5.5	MDIAG Triggered Emission Frequency Correlations	88
5.6	Kp and Total Growth Effect on the Number of Triggered Emissions	90
5.7	STACO Triggered Emission Frequency Analysis	92
6.1	MDIAG Superposed Epoch Kp Analysis	103
6.2	MDIAG Non-reception and Reception Examples	106
A.1	MDIAG 04/05/1986 11:05:30 UT	117
A.2	MDIAG 04/05/1986 12:05:30 UT	117
A.3	MDIAG 04/05/1986 13:20:30 UT	118
A.4	MDIAG 04/25/1986 13:05:30 UT	118
A.5	MDIAG 04/30/1986 13:50:30 UT	119
A.6	MDIAG 05/01/1986 12:20:30 UT	119
A.7	MDIAG 06/11/1986 13:24:00 UT	120
A.8	MDIAG 06/11/1986 15:05:30 UT	120
A.9	MDIAG 06/12/1986 15:05:30 UT	121
A.10	MDIAG 06/12/1986 15:05:30 UT	121
A.11	MDIAG 06/17/1986 15:20:30 UT	122
A.12	MDIAG 10/01/1986 12:20:30 UT	122
A.13	STACO 08/07/1986 11:49:00 UT	123
A.14	STACO 08/14/1986 11:49:00 UT	124

A.15 STACO 08/18/1986 11:49:00 UT	124
A.16 STACO 08/18/1986 12:21:00 UT	125
A.17 STACO 10/01/1986 12:17:00 UT	125
A.18 STACO 10/03/1986 12:17:00 UT	126
A.19 STACO 10/08/1986 11:47:00 UT	126
A.20 STACO 10/16/1986 14:47:00 UT	127
A.21 STACO 11/21/1986 15:47:00 UT	127
A.22 STACO 12/17/1986 14:47:00 UT	128
A.23 STACO 12/17/1986 14:47:00 UT	128
B.1 Riser 08/07/1986 15:05:30 UT	130
B.2 Riser 04/22/1986 12:50:30 UT	130
B.3 Faller 06/30/1986 16:35:30 UT	131
B.4 Faller 05/15/1986 16:59:00 UT	131
B.5 Hook 07/01/1986 16:35:30 UT	132
B.6 Hook 10/08/1986 15:35:30 UT	133
B.7 BLI 12/19/1986 11:05:30 UT	134
B.8 Early Riser 06/11/1986 12:50:30 UT	134

Chapter 1

Introduction

The Earth is not an isolated planet but is rather part of a complex space environment which reaches from the surface of the planet all the way to the Sun. Effects and interactions between the Sun and the Earth's magnetic field have tremendous ramifications for life on Earth and for the satellite and spacecraft orbiting in the region around the Earth, the so-called near-Earth space environment. The plasma that composes the vast majority of space creates an environment with a wide range of plasma phenomena that have yet to be understood. This dissertation focuses on the results of interactions between electromagnetic waves in the Extremely Low and Very Low Frequency range (300 Hz to 30 kHz) injected into space and the energetic electrons that populate the region of space in the near-Earth space environment. These interactions can result in complex modifications of the electromagnetic waves, and observations can be interpreted to provide insight into the physics of the process and the resultant effects on the space environment. In this section, we provide the relevant physical background concerning the near-Earth space environment, briefly describe the experimental transmitter used for controlled studies, and outline the primary scientific contributions presented in this dissertation.

1.1 The Near-Earth Space Environment

One approach to understanding the importance of the space environment is to understand the Earth in the context of a complex system by considering the notion of a “sun-to-mud” system by studying the physical properties and behavior from the ground up through the atmosphere and through space all the way to the Sun. Space is a tremendously complex region, filled with electromagnetic waves and plasma, and permeated by a variety of magnetic fields. Of importance to this dissertation is a region closer to Earth called the magnetosphere. The magnetosphere is defined as the region of space where the Earth’s geomagnetic field plays a dominant role in governing local physical behavior. While the Earth’s magnetic field can be approximated using a dipole model, similar to the field of a bar magnet, its overall shape is distorted by the presence of the solar wind. Pressure from the solar wind can compress the windward side of the Earth’s magnetic field and lengthen the opposite side into an extended tail.

Of primary concern for this work is a region of the magnetosphere closer to the Earth called the inner magnetosphere. The magnetic field remains dipolar in this region, within about $5 R_E$ or 31,850 km (1 Earth radius $R_E \simeq 6370$ km) around the Earth. This region is important to understand as man-made satellites typically reside in and any spaceward missions would pass through this region. Furthermore, the inner magnetosphere can be utilized as a natural plasma laboratory for improving our understanding of plasma physics by studying the plasma interactions that naturally occur. The plasma in this region, relevant to this work, can be divided into two populations based on their different particle energies, which are described in terms of temperature, as shown in Figure 1.1.

The dipole structure of the magnetic field lines are in black, and the magnetosphere is permeated by a lower energy, or cold, plasma population represented in green called the plasmasphere [Tascione, 1994, Sec 5.6]. The second plasma population of interest is the energetic, or hot, plasma population represented in red located in distinct regions called the radiation belts [Tascione, 1994, Sec 4.8-4.9]. In describing locations in the magnetosphere, we refer here to the L -shell value (L) and the magnetic

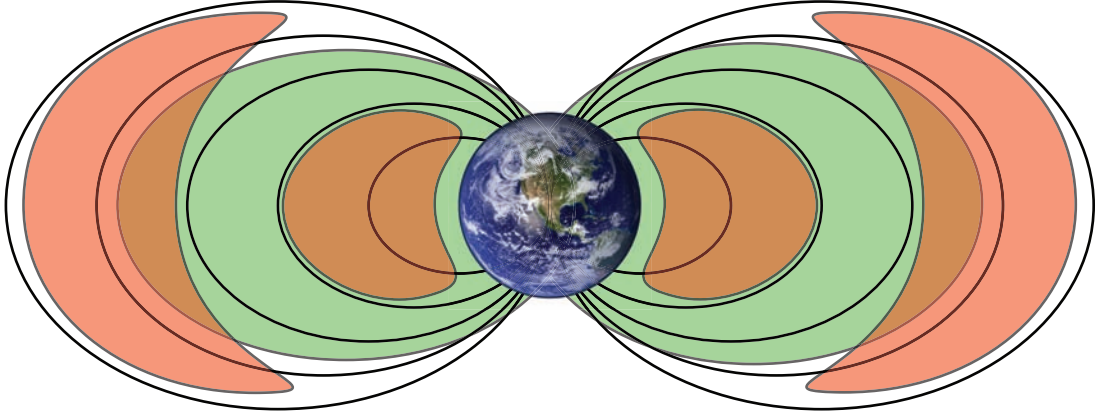


Figure 1.1: Illustration of the Earth’s inner magnetosphere, with the plasmasphere in green, the radiation belts in red, and the Earth’s magnetic field lines traced out in black.

local time (MLT). The L -shell refers to the distance, in units of Earth radii or R_E , of the equatorial crossing of the magnetic field lines in a dipole model. Tracing the field lines down to the Earth allows for a rough description of paths of propagation associated with a geographic location on the ground. MLT indicates the direction of the magnetic field relative to the direction of the sun, and here is occasionally referenced as UT–MLT to describe the offset between the temporal and magnetic local time.

1.1.1 The Plasmasphere

The plasma of the plasmasphere is cold and relatively dense. The electron energies in this region are on the order of 1 eV (10000 K), while the densities are between 100 and 1000 cm^{-3} . The plasmasphere within the inner magnetosphere is of a higher density and is separated from the rest of the magnetosphere at a boundary with a sharp drop-off in density called the plasmopause [[Carpenter, 1963, 1966](#)]. The extent of the plasmasphere, bounded by the plasmopause, ranges between $2 R_E$ and $7 R_E$.

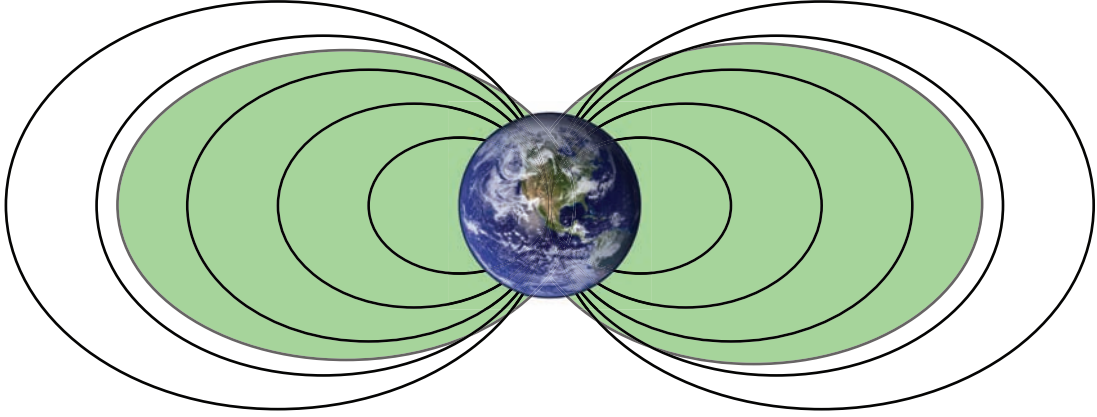


Figure 1.2: Illustration of the Earth's inner magnetosphere, showing only the cold, dense background plasma of the plasmasphere in green.

1.1.2 The Radiation Belts

Highly energetic plasma is located in several distinct regions called the radiation belts [Walt, 1994]. The charged particles gyrate around the Earth's magnetic field due to the Lorentz force and are trapped due to the magnetic field line configuration, which results in stronger fields as the particles approach the Earth's magnetic poles. The spatial magnetic field gradients in the Earth's magnetic field results in the rate of particle gyration increasing and the parallel particle velocity consequently diminishing as the particles approach the Earth. Energetic ions and electrons can then reverse their direction, resulting in “mirroring” of the particles, which traps them within the region of space called the radiation belts. There are several regions where the trapping of energetic electrons occur, resulting in an inner and an outer radiation belt and occasionally even a transient third radiation belt [Baker et al., 2013]. The electrons are much more energetic than the plasmaspheric electrons, with energies between 0.1 MeV and 10 MeV but with a lower density of less than 1 cm^{-3} .

1.1.3 Whistler-Mode Electromagnetic Waves

In addition to the plasma population, the magnetosphere also contains a wide variety of electromagnetic waves whose behavior is modified due to the existence of the

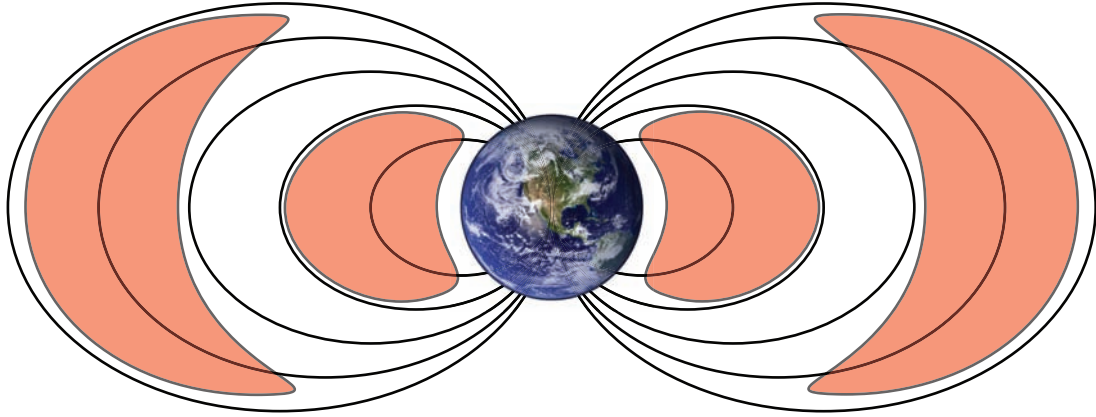


Figure 1.3: Illustration of the Earth's inner magnetosphere, showing only the two typical radiation belts, in red, which trap the energetic plasma.

plasma. These waves can be generated on the Earth, for instance naturally from lightning or from man-made sources such as power lines, and radiate into space, or they can be result from plasma interactions and occur naturally in space. In particular, the cold background plasma in the plasmasphere determines the modes of propagation for these waves, introducing dispersion effects and natural frequency cutoffs [*Bittencourt*, 2013, pp. 418-429]. The particles that constitute the hot plasma can interact with the waves and modify the wave behavior, resulting in wave amplification and the generation of new free-running plasma emissions.

Of particular importance are whistler-mode waves, which can interact with the trapped energetic electrons [*Walt*, 1994, pp. 118-128]. These whistler-mode waves propagate approximately parallel to the background geomagnetic field in the extremely and very low frequencies (ELF/VLF) between 300 Hz and 30 kHz. Under certain resonance conditions, when the parallel electron velocity v_{res} is such that the wave frequency ω and electron gyrofrequency ω_c match, as:

$$v_{\text{res}} = \frac{\omega_c - \omega}{k} \quad (1.1)$$

(with k being the wavenumber) the electrons perceive the wave as nearly stationary and interact over relatively long durations as shown in Figure 1.4. This interaction can result in the exchange of energy and momentum between the wave and energetic

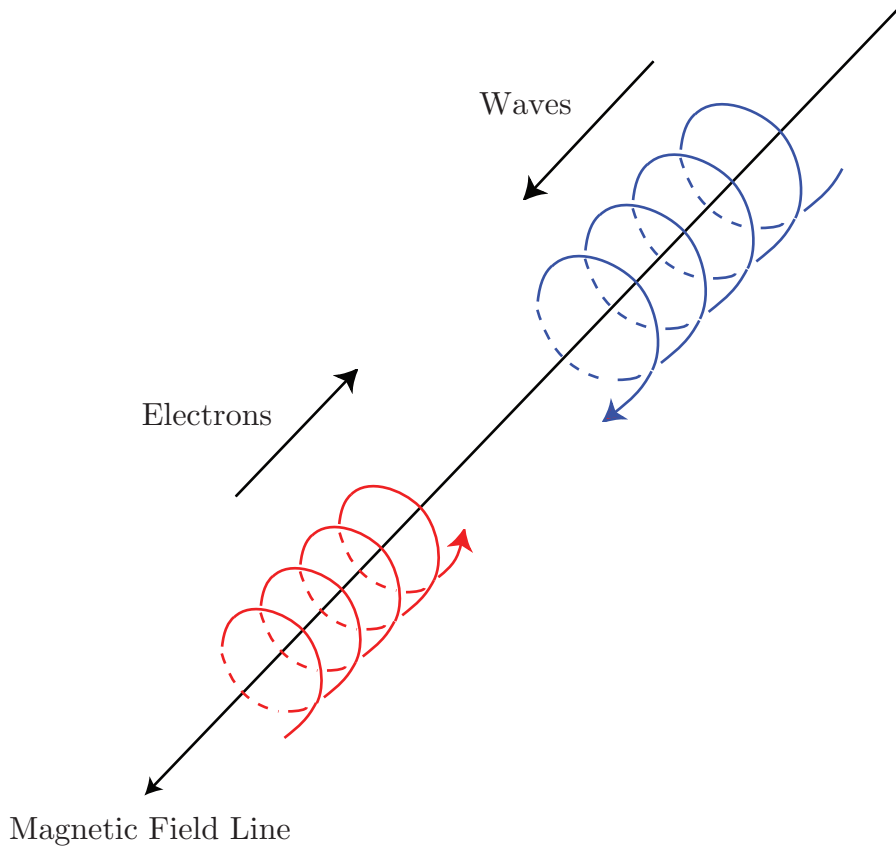


Figure 1.4: Schematic layout of the wave-particle interaction under resonance, where the traced out electric field vector (blue) of the wave and energetic electrons (red) are gyrating around the magnetic field line at the same frequency.

electrons, resulting in the waves gaining energy from the electrons and vice versa.

These whistler-mode wave-particle interactions are an important driver of the behavior of the space environment. Wave-particle interactions in the Earth's magnetosphere have been extensively studied over the last 50 years and are considered to be the cause for a number of space phenomena, including the generation of naturally occurring waves such as chorus [*Sazhin and Hayakawa, 1992*]. Chorus emissions are intense electromagnetic plasma waves that are spontaneously excited in the magnetosphere and play an important role in the behavior of the Earth's radiation belts [*Bell et al., 2009*]. An example observation from the CLUSTER spacecraft is shown in Figure 1.5.

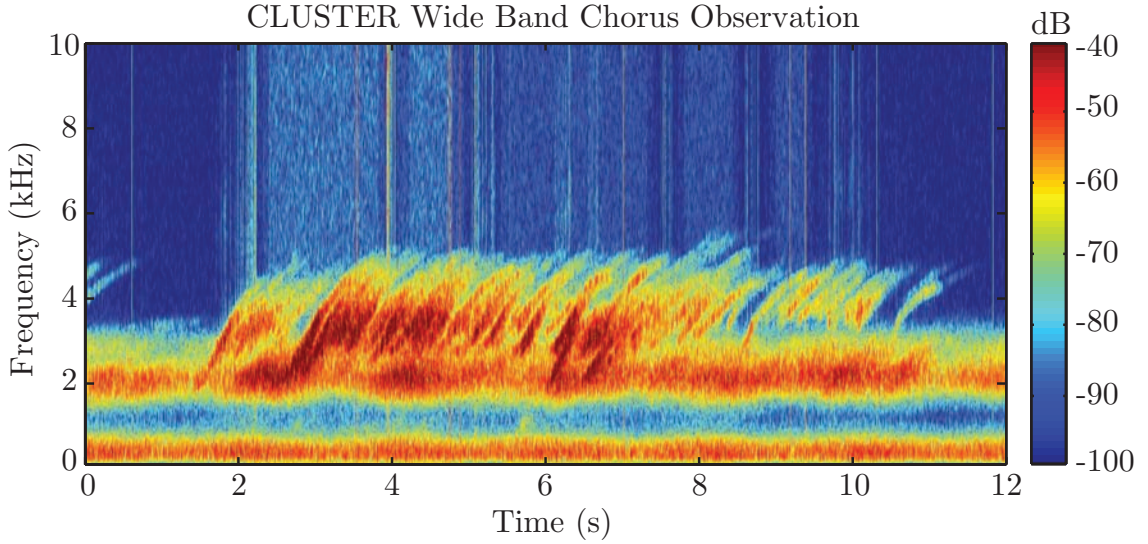


Figure 1.5: ELF/VLF chorus example observed by the Wide Band instrument aboard the CLUSTER satellite.

Directly studying wave-particle interactions in-situ has been difficult due to the limited number of satellites and the limited spatial coverage of satellite measurements. Instead, early work focused on ground based observations of ELF/VLF waves using radio receivers, which allowed for more frequent measurements of total wave modifications integrated over the path of propagation. Broadband electromagnetic impulses generated by lightning strokes, called radio atmospherics or sferics, can escape into and propagate through the magnetosphere. After propagation through the magnetosphere and the corresponding dispersive effects, the resulting signals are called whistlers. While early observations used these naturally occurring, lightning-generated whistlers as the source waves for observing wave-particle interactions [Helliwell, 1965, Ch. 4], interest developed in further studying wave-particle interactions with controlled wave injections into the magnetosphere using ground-based transmitters [Helliwell *et al.*, 1964].

The most extensive and long-lasting of these controlled experiments is shown in Figure 1.6. The VLF transmitter, located in Antarctica, injects waves into the magnetosphere that propagate in the whistler mode along paths called ducts. These waves are then modified through interactions with energetic electrons near the equator, in

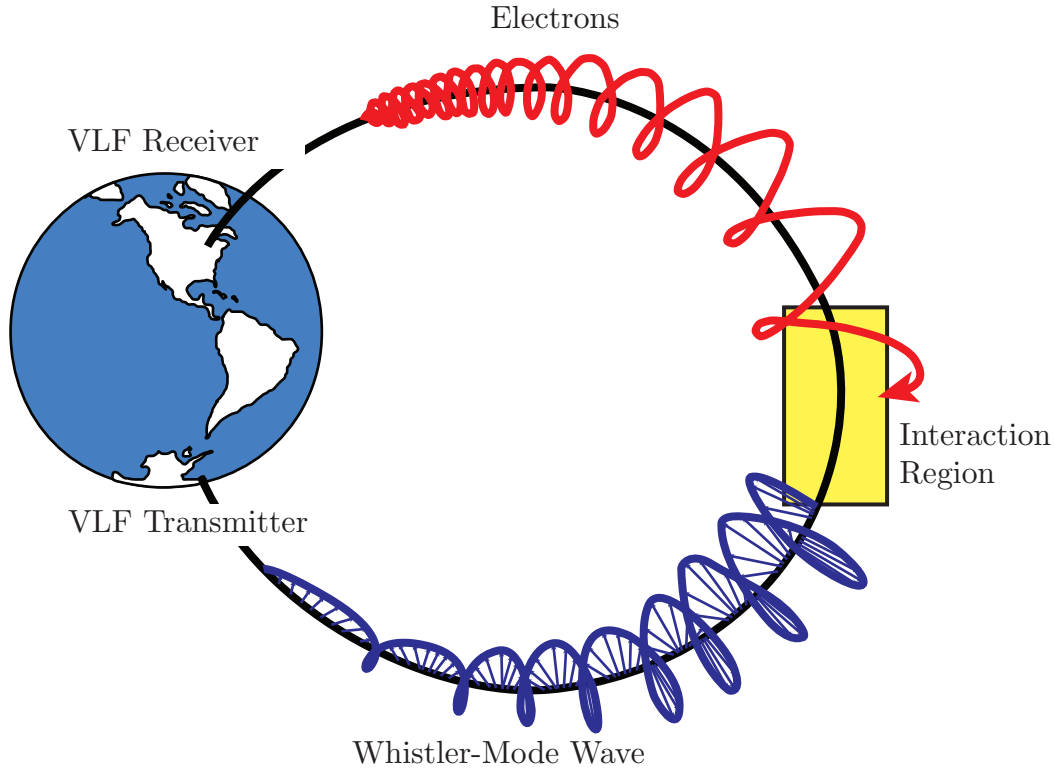


Figure 1.6: Experimental setup of a controlled wave injection experiment. The VLF transmitter injects waves (the electric field component in blue) into the magnetosphere, which are modified via interactions with energetic electrons (gyrations in red) in the interaction region (yellow) and then received by the receiver in the conjugate hemisphere.

the region so termed the interaction region. The modified waves continue to propagate along the duct and are observed by the receiver located in the conjugate hemisphere. An example of a transmission from a transmitter at Siple Station and the received observation at the Lake Mistissini receiver at the conjugate hemisphere is shown in Figure 1.7. The particular time-frequency format shown in Figure 1.7(a) is called the MDIAG format, and the reception in Figure 1.7(b) exhibits signs of amplification as well as the occurrence of new frequency components.

Ground-based observations by the receivers are also supported by indices describing geomagnetic conditions. These indices, the Kp index, the AE index, and the

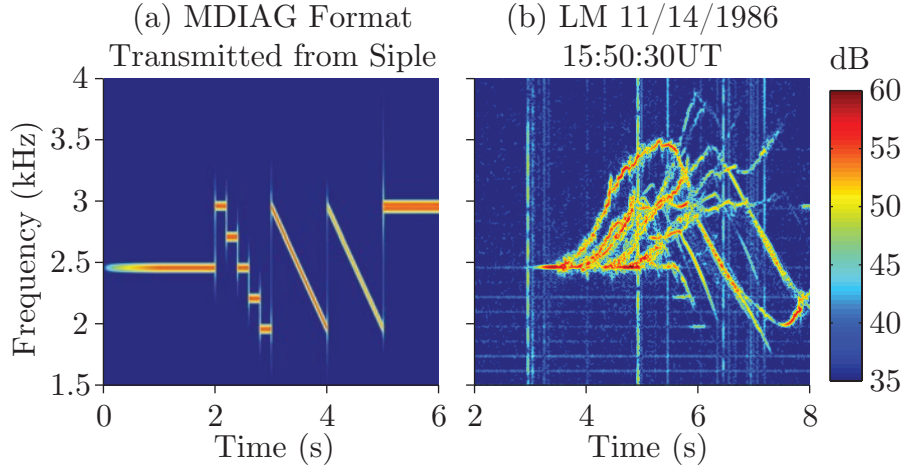


Figure 1.7: (a) A transmission of the MDIAG format by the VLF transmitter at Siple Station, Antarctica, and (b) the corresponding reception observed at the Lake Mistissini receiver located in the conjugate hemisphere.

SYM-H index, are produced through the collaboration of a number of different observatories and ground stations and were obtained here from the World Data Center for Geomagnetism, Kyoto (which is operated by the Data Analysis Center for Geomagnetism and Space Magnetism at Kyoto University). The indices differ in their intended scope and their resolution. The Kp index describes the global activity and disturbances in the geomagnetic field over 3-hour intervals. The AE index describes the global electrojet activity in the auroral zone, the current in the ionosphere at the poles, through measurements by observatories in the auroral zone in the northern hemisphere with a 1-minute resolution. And, the SYM-H index describes the mid-latitude and equatorial activity by characterizing the longitudinally symmetric disturbance in the horizontal direction with a 1-minute resolution.

1.2 Whistler-Mode Wave Injection Observations

Generating waves in the ELF/VLF bands is a significant engineering challenge, as the corresponding free space wavelength is on the order of hundreds of kilometers. A vertical antenna of sufficient length for reasonable transmission efficiencies would be

physically impractical, and a horizontal antenna suffers from significant losses due to image currents caused by the ground plane [Watt, 1967]. To mitigate the inefficiencies and losses of a horizontal antenna, it was observed that natural conditions could be leveraged to reduce ground losses. A location in Antarctica takes advantage of the Antarctic ice sheet to provide 2–3 km of natural dielectric isolation from the conducting ground. The resulting reduction in near-field image losses allowed for the operation of reasonably powerful transmitters, providing a unique opportunity to study the magnetosphere in a controlled manner [Helliwell, 1970].

1.2.1 Early Experiments

While the focus of this work is on data generated by the Siple transmitter at Siple Station, Antarctica, we provide here a brief historical summary covering some of the early work preceding the establishment of Siple Station. Observations and interest in whistler-mode waves and wave-particle interactions began nearly 60 years ago. *Helliwell and Gehrels* [1958] noted the first observations of man-made whistler-mode signals, and a referenced conference paper by *Helliwell* [1962] mentioned the first observations of VLF triggered emissions. Neither work could be located in their entirety, but are referenced and summarized in *Helliwell and Katsufakis* [1974] and *Helliwell et al.* [1964] respectively. Similarly, the 57th IGY Bulletin published in March 1962 [Helliwell and Carpenter, 1962] refers to a report published by *Helliwell and Carpenter* [1961] that could not be located, which summarizes the first descriptions of a variety of VLF phenomena, including the description of triggered emissions classified as risers, fallers, and quasi-constant tones.

Building on these earliest observations of magnetospheric phenomena, researchers continued to make observations of whistler-mode VLF signals and wave modifications resulting from wave-particle interactions. A number of observations were made using signals transmitted from VLF Navy transmitters [Helliwell et al., 1964; Lasch, 1969] as shown in Figure 1.8 and from Omega navigation transmitters [Kimura, 1968], but the inherent limitations in fixed transmitter frequencies and the transmitter locations led to interest in a more dedicated and flexible transmitter for obtaining experimental

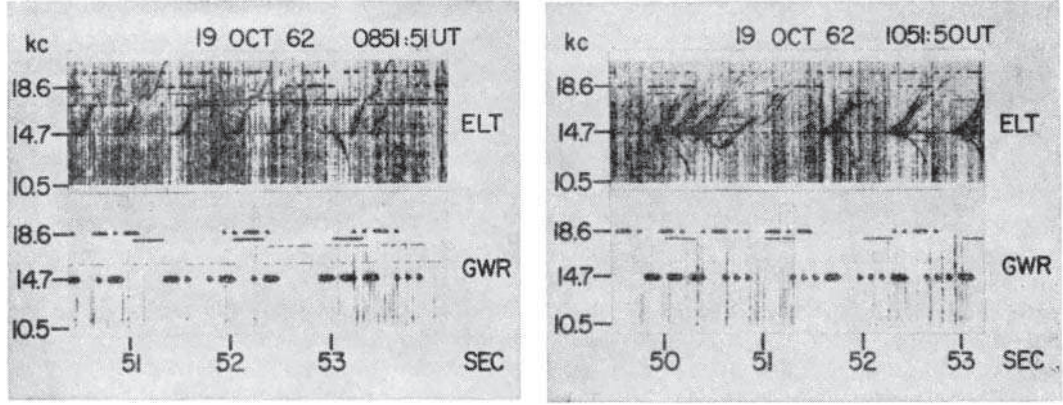


Figure 1.8: Figures 2 and 3 from [Helliwell et al. \[1964\]](#), showing examples of some of the earliest observations of triggered emissions. The emissions are triggered from Morse code dashes transmitted from the NAA VLF transmitter and recorded aboard the USNS *Eltanin* on October 19, 1962, while it was near the Palmer Peninsula at 51.5degS geomagnetic latitude.

scientific data [[Trabucco and Paschal, 1978](#)].

A first attempt led to the establishment of a transmitter at Byrd Station ($L=7.25$) by the University of Washington that operated from 1966-1969. However, wave injection experiments failed to produce detectable signals in the conjugate region due to the high geomagnetic latitude of the station and low antenna efficiency [[Helliwell and Katsufrakis, 1974](#)]. Recordings of abundant natural VLF activity near $L=4$ at Eights Station suggested that a transmitter site at a lower latitude would be more productive [[Helliwell and Katsufrakis, 1978](#)], leading to the establishment of Siple Station.

1.2.2 Siple Station

Siple Station was located at 75.93° S, 84.25° W geographic, corresponding to an invariant latitude of 60.4° S, at $L=4.2$ and with $UT-MLT=+5$. The magnetic conjugate point of the station was easily accessible, and a conjugate receiving station was deployed near Roberval, Quebec, Canada (48.52° N, 72.23° W) and then moved to Lake Mistissini (50.42° N, 73.87° W) in 1985 to reduce the increasing amount of local receiver noise due to industrial activity around Roberval [[Helliwell and Katsufrakis,](#)

1974; *Paschal*, 1988].

Construction of the station began in the austral summer of 1969/1970, and the station was named in honor of Paul Siple, an Antarctic pioneer and scientist. The original 21.2 km long dipole antenna was driven by an 80 kW transmitter until it was eventually upgraded in the austral summer of 1978/1979 to a 150 kW transmitter [*Carpenter and Bao*, 1983]. The antenna itself was extended in the austral summer of 1982/1983 to 42 km, with a second perpendicular dipole of the same length installed over two austral summers from 1984 to 1986 [*Gibby*, 2008, pp. 19-20] in order to efficiently couple into the whistler-mode. By 1986, the Siple Station transmitter could radiate over 1 kW of ELF/VLF power, with antennas driven by a 150 kW source [*Raghuram et al.*, 1974; *Carpenter and Bao*, 1983]. This level of ELF/VLF radiated power available solely for scientific research remains unmatched to date.



Figure 1.9: A composite picture showing an elevated picture of Siple Station, and inset pictures of the station signpost and the United States flag. Photo credit for these pictures goes to Jim Logan, a station operator at Siple Station, who took these pictures in 1986.

Further details on the history, facilities, and life at Siple Station can be found

in [Gibby \[2008, Section 2.2\]](#), and additional descriptions of some early experiments and observations can also be found in [Golkowski \[2009, Section 1.3\]](#). An extended history of VLF research and the VLF Group at Stanford by one of the highly involved scientists has been written by [Carpenter \[2014\]](#) and includes a number of wonderful tales concerning Siple and the researchers involved in its development and operation.

1.2.3 Later Experiments

After Siple closed in 1988, there were fewer active wave injection experiments and fewer scientific VLF transmitters. The most recent wave injection experiment was the High Frequency Active Auroral Research Program (HAARP), which modulated the ionospheric conductivity of the auroral electrojet to perform magnetospheric wave injection [[Cohen et al., 2010a](#); [Cohen and Golkowski, 2013](#)]. However, it generated fewer wave injection results as its location was less favorable for producing strong magnetospheric amplification, its conjugate point was in the ocean and difficult to access, and it yielded only 10–100 W of radiated ELF/VLF power during the most favorable geomagnetic conditions [[Platino et al., 2006](#); [Golkowski et al., 2008, 2010, 2011](#); [Jin et al., 2011](#)]. As of 2015, the HAARP facility itself is also currently closed.

In addition to HAARP, some work has continued with satellite observations of various VLF waves with additional measurements of the energetic electron distributions on the POLAR spacecraft [[Bell et al., 2000](#)]. Other experiments have been proposed to fill this gap in experimental scientific capability, either with novel methods for a practically feasible long horizontal dipole antenna or with space-borne transmitters and experiments, but no such work is in progress at the moment. While VLF Navy transmitters do remain operational, they are limited as before in frequency, format, and their present location.



Figure 1.10: A picture taken at ground level of the antenna array on site of the HAARP facility in Alaska.

1.3 Thesis Organization

This historical analysis of the data generated by Siple during fifteen years of its operation was limited to selected case studies. Now, with modern advances in computational resources, large volumes of data can be analyzed to provide a statistical understanding of the wave modifications resulting from wave-particle interactions in the magnetosphere. The focus of this dissertation is to discuss the experimental results of wave injection experiments using the Siple Station VLF transmitter, in particular focusing on wave amplification and generation effects. The dissertation is composed of 6 chapters divided into three sections covering introductory material, 3 experimental studies, and remarks on experimental and theoretical scientific implications. Chapter 1 covers briefly the space environment, with additional detail concerning the regions, the plasmasphere and the radiation belts, most relevant to this dissertation and the

whistler-mode electromagnetic waves of interest. It also describes ongoing scientific interest in studying the magnetosphere, through the use of ground-based transmitters, with a focus on the transmitter at Siple Station, Antarctica. Chapter 2 presents a literature review covering the numerous studies and results generated using data from the Siple transmitter. It addresses both experimental work conducted at Siple as well as theoretical approaches relevant to wave-particle interactions. Finally, given the historic nature of Siple Station, it provides some context for the equipment used to record and the data and the needed preprocessing steps taken in order for current work to be conducted. Chapter 3 begins the description of the analytic work with the first experimental study presenting statistical results describing amplification behavior resulting from wave-particle interactions using a diagnostic format (MDIAG) transmitted from Siple in 1986. Chapter 4 continues with the second experimental study, which considers one specific amplification phenomenon called the preferential amplification effect. This chapter uses data from a second format (STACO) to characterize the extent of this effect, and then utilizes a self-consistent numerical model of coherent wave amplification in order to provide a physical interpretation of the effect. Chapter 5 presents the third experimental study in quantifying the generation of free-running plasma emissions triggered from injected waves using both the MDIAG and STACO formats. These triggered emissions are a long-studied result of wave-particle interactions that remain unexplained, and statistical observations and bounds help constrain numerical simulations and theoretical predictions. Chapter 6 concludes with an example of how the data can be used for predictive capabilities for future experiments or applied applications and then summarizes this dissertation and provides avenues for possible future work.

1.4 Scientific Contributions

The scientific contributions presented in this dissertation are the following:

- 1) Quantified the nonlinear growth rate and the total growth of very low frequency waves injected into the magnetosphere from the Siple Transmitter Experiment
- 2) Quantified the preferential magnetospheric amplification of rising versus falling

frequency-time structures

3) Utilized a Vlasov-Maxwell numerical simulation to show that the total amplification depends on the linear growth rate and the onset and duration of nonlinear growth, which for typical hot plasma parameters favors rising frequency-time structures

4) Developed an empirical frequency-time profile of free-running plasma emissions triggered by signals injected from the Siple transmitter

5) Developed statistical models for predicting the reception of Siple transmissions in the conjugate hemisphere and a framework for evaluating the occurrence of triggered free-running plasma emissions

Chapter 2

Scientific Background

While the preceding work of [Gibby \[2008\]](#) presented an excellent overview of the history and development of Siple Station and even some insight into daily life at the station, less detail has been provided concerning the breadth of scientific work conducted at and through Siple Station in expanding the field of magnetospheric physics. Here, we present a review of papers published in the Stanford Very Low Frequency Research Group and by other researchers working with Siple data, along with several related papers from the Siple era. These prior publications were encountered in the course of this doctoral work, and this review is intended to aid future workers in this field in providing an overview of previous work. Similarly, as the theory and modeling efforts have improved dramatically over the years, selected papers describing theory and modeling efforts based on Siple experimental data and several additional papers describing general approaches in the field are also presented.

2.1 Experimental Review

This period from ~ 1950 to ~ 1990 was a time of active ELF/VLF research into wave-particle interactions in the Earth's magnetosphere. A number of other active experiments took place during this time, allowing scientists to examine data generated from a variety of signal sources, such as whistlers [[Storey, 1953](#); [Carpenter, 1978](#)], scientific transmitters (including a vertical, balloon-borne transmitter [[McPherson et al., 1974](#);

[Koons and Dazey, 1983](#); [Koons et al., 1976](#)]), and transmitters serving other purposes [[Kimura, 1968](#); [Likhter et al., 1971](#)]. Of all of these experiments, Siple was the most specific, prolific, and overall long lasting. The following review of experimental work from Siple is divided into two parts. The first section on past work considers a number of experiments most directly relevant to this work, while the second section looks at a variety of other publications focusing on other interesting phenomena observed in the Siple and pre-Siple era.

2.1.1 Related Past Work

A tremendous amount of work was published utilizing Siple data, and many individuals deserve credit for the success of this unique experiment. In terms of publications overall and related to this work, two people in particular must be highlighted.

Professor Robert A. Helliwell was the first professor of the Stanford VLF group and was a driving force in the establishment of Siple Station. He joined the Stanford faculty in 1946 and remained active in the field of very low frequency radio waves until his passing in 2011. He is the author on numerous papers and published a number of summary papers combining historical facts about Siple Station with an overview of a number of different phenomena observed from Siple data [[Helliwell, 1988a,b, 1983, 1979](#); [Helliwell and Katsufakis, 1974](#)]. Of significant value as a reference, [Helliwell and Katsufakis \[1978\]](#) covers both the schematic layout of Siple and the earlier receiving system at Roberval, as well as briefly exploring some early observations and results from Siple in terms of wave amplification, power line radiation, suppression, quiet bands, wave-wave interactions, and satellite observations. Further observations and sketched out forms of what he then termed as wave-wave interactions are provided in [Helliwell \[1979\]](#).

The other prolific Siple researcher is Professor Donald L. Carpenter, who remains active in the field today. His contributions cover papers first exploring the signal properties of observed Siple signals [[Carpenter and Miller, 1976](#)], providing early statistics on occurrence rates and conditions for one-hop signals from Siple observed at the Roberval receiver [[Carpenter and Bao, 1983](#)], and examining case studies of

observed Siple signals outside of the plasmopause [*Carpenter and Miller, 1983; Carpenter and Sulic, 1988*].

As additional background references, the details of the antenna efficiencies can be found in *Raghuram et al. [1974]*, and a brief historical note on the transmitter upgrade to Siple is presented in *Trabucco and Paschal [1978]*. Also, given the large number of different signal formats transmitted by Siple, a useful reference which surveys the various transmission formats can be found in Appendix A of *Mielke [1993]*.

In addition to its unique scientific accomplishments, we must not forget that the Siple experiment was a massive logistical undertaking. Siple Station was the only United States Antarctic base whose location was chosen for a scientific reason, and its construction and maintenance presented tremendous logistical challenges. The key person responsible for all operational aspects of Siple Station was Professor John Katsufakis, who spent more than 20 austral summers in Antarctica in the course of preparation, establishment, and logistical support of the activities of the station.

Nonlinear Wave Amplification

While most work during Siple's operation focused on the extraordinary singular events with case studies, two statistical studies laid the foundation for the present statistical study of wave amplification resulting from wave-particle interactions. These studies focused on studying properties of the hot plasma distribution by examining transmissions during a continuous nine hour period over two days in January of 1988 [*Carpenter et al., 1997; Sonwalkar et al., 1997*]. Here, they presented quantified initial amplitudes, nonlinear growth rates, and saturation thresholds based on a larger dataset than previously described, and observed evidence of possible structured irregularities in the plasma over various time scales that determined these amplitude characteristics. One other important paper of note on amplification statistics would be the early work by *Stiles and Helliwell [1977]*, who analyzed the amplification of injected whistler mode pulses as well as the resulting triggered emissions. His statistical work was limited in the amount of Siple data analyzed, but provides valuable comparison through additional analysis of transmissions from the NAA station and the Omega transmitter. Amplification characteristics have been more thoroughly

analyzed with more recent, extended statistical characterization of initial signal amplitudes, nonlinear growth rates, and saturation thresholds measured from 442 cases over a nine month period from April to December of 1986 [Li *et al.*, 2014].

As amplification of injected waves was a constant topic of study during Siple's operation, significant effort was devoted to understanding the factors that determined the characteristics of amplification. Carlson *et al.* [1985a] (with some higher contrast, corrected figures in Carlson *et al.* [1985b]) utilized the capability for transmitting variable frequency sweep rate waves and injected ± 0.125 to ± 7 kHz/s frequency-time ramps covering a 1 to 8 kHz frequency range. In addition to using the frequency ramps as a diagnostic for finding the L -shell and electron density measurements of the duct, Carlson *et al.* [1985a] found frequency dependencies with a lower cutoff frequency exhibiting rapid gain or attenuation in proportion to the ramp frequency sweep rate and an upper cutoff frequency consistent with the half gyrofrequency cutoff. Concerning wave amplification, Carlson *et al.* [1985a] observed differences in the amplitude behavior between rising and falling frequency ramps. Similarly, Mielke and Helliwell [1993] noted when considering the approximation of continuous frequency ramps with staircase tones that injected rising ramps appeared to amplify more than injected falling frequency ramps. These early observations of the effect of the frequency sweep rate on wave amplification led to more recent work which quantified the preferential amplification phenomenon, where injected rising ramps are favorably amplified over injected falling ramps, and enabled the first theoretical interpretation of the phenomenon [Li *et al.*, 2015a].

A number of other works explored other aspects of wave amplification such as initiation of nonlinear amplification and the nonlinear growth rate, as well as the saturation threshold and underlying mechanism. Helliwell *et al.* [1980] varied the transmitted amplitude to determine the effect on the resulting wave-particle interactions. By ramping the input power to Siple's antenna, he discovered a threshold power, P_t , where below P_t no amplification or triggering was observed. Similarly, Mielke and Helliwell [1992] approached this nonlinear amplification threshold effect by experimentally transmitting an additional band of noise to artificially increase the threshold power. That the noise did suppress triggering effects was taken as evidence

of the role of ambient magnetospheric noise, such as hiss, in determining the conditions suitable for coherent wave-particle interactions. Observations of nose whistlers indicated a rapid amplification of the portion of the whistler above the nose frequency, leading [Helliwell et al. \[1990\]](#) to reproduce this effect with artificial nose whistlers (the so-called NOWS, NOse Whistler Simulation, transmission format). One such example showed the NOWS signal reaching the same saturation threshold as a reference CW signal but with a peak growth rate of 1250 dB/s versus the 55 dB/s growth rate for the CW reference. The authors indicated that statistics were planned to be reported later, but no later work on this was found. The proposed interpretation for this phenomenon was in support of the second order resonance theory put forth by [Helliwell \[1967\]](#). [Gibby et al. \[2008\]](#) considered the nonlinear effects of the saturation process which causes amplification to cease and found that saturation results in long-period oscillations in the signal amplitude, short-period oscillations that look like sidebands, and the formation of an incoherent band of noise around the transmitted frequency.

Nonlinear Wave Generation

Many papers from this time included examples or mention of the generation of free-running plasma emissions, which were a major focus of study. These emissions and the phenomena they represented acquired various names such as triggered emissions (TE's), artificially stimulated emissions (ASE's), and coherent wave instabilities (CWI's), although the most commonly used term today is triggered emission. These triggered emissions take on complex forms, often appearing as some combination of risers, fallers, hooks, and other unusual forms such as band-limited impulses (BLI's) [[Helliwell, 2000](#)]. Early work observed triggered emissions from various sources such as Navy transmitters [[Helliwell et al., 1964](#); [Helliwell, 1965](#); [Lasch, 1969](#)], Omega navigation transmitters [[Kimura, 1968](#)], and natural noise such as whistlers [[Carpenter et al., 1969](#)]. With Siple specifically designed for studying wave-particle interactions, many more observations were then made of triggered emissions with examples appearing in all experimental papers. The earliest statistical work on triggered emissions compared emissions from NAA, Omega, and Siple transmissions and provided some early conclusions describing triggered emission behavior [[Stiles and Helliwell, 1975](#),

1977]. More recent work, presented in Chapter 5, has examined a longer period and a larger number of triggered emissions from Siple’s operation in 1986 to develop updated descriptions of triggered emission behavior.

Other papers also addressed other aspects of triggered emissions. *Carpenter and Lasch* [1969] also explored the dependence of triggering on the transmitter frequency, in observing a decrease in triggered emissions from the NAA transmitter as the transmitter frequency increased. Here, the difference in triggering behavior was attributed to the particular plasma properties around $L=3$ and possible influences from the timing of the solar cycle. *Carlson et al.* [1985a] observed that triggered emissions only triggered from ramps with frequency sweep rate magnitudes <1 kHz/s, suggesting an intrinsic sweep rate limit of triggered emissions. *Chang and Helliwell* [1979] ran an experimental format where the signal was artificially interrupted by suddenly shifting the frequency of the transmitter. This shift in the transmitter frequency effectively resulted in a momentary termination of the signal. These interruptions resulted in the generation of triggered emissions, with the type of emission dependent on the duration of the interruption.

2.1.2 Other Interesting Phenomenon

In addition to the above mentioned papers that laid the framework for this work, many other studies were conducted utilizing other transmission formats to characterize and interpret other related plasma phenomena. Given the wide range of very different topics, these other papers are summarized here in no particular order.

Interactions of Multiple Waves

Work by *Chang et al.* [1980]; *Helliwell et al.* [1986] looked at the effect of multiple wave interactions, primarily in observing the frequency spacing between signals for wave-wave interactions and wave-wave interactions resulting from interactions of transmitted waves with their induced sidebands. Utilizing the crossed dipole antenna setup, *Mielke et al.* [1992] examined the transmission difference attributable to signal polarization. One finding was that right-hand polarized signals were detected the most

strongly, and that observations overall agreed well with classic magneto-ionic theory. [Mielke and Helliwell \[1993\]](#) further considered the capabilities and limitations inherent to the Siple transmitter by exploring the transmitters capacity in approximating ideal transmission formats. Using variously spaced staircase tones as approximations to a frequency-time ramp, [Mielke and Helliwell \[1993\]](#) found that staircases with separations less than 25 ms provided a better approximation for a continuous ramp. A number of studies focused on the possible effects due to power lines. Lower wave intensities were observed on Sundays, termed the Sunday effect, were attributed to reduced power line activity [[Park and Miller, 1979](#)]. Observations of triggered emissions from power lines were reproduced using specifically designed Siple transmission formats [[Park and Chang, 1978](#)]. And, experiments using transmissions of the CISP (Carrier Interaction with Simulated Power line) format probed the role of power lines in interacting with transmitted waves in the generation of sidebands [[Sa and Helliwell, 1988](#)]. Sidebands were another important aspect for evaluating wave-wave interactions. [Park \[1981\]](#) observed the generation of strong sidebands from Siple long, >1 s, keydown transmissions and noted that the sidebands can spread greatly in frequency from ~ 2 Hz to 100 Hz as well as exhibit a wide range in amplitudes from -10 dB to 0 dB relative to the transmitted carrier.

Phase Analysis

Another avenue of interest was studying not only the amplitude but the phase of the received signal. [Paschal and Helliwell \[1984\]](#) laid out the idea of using signal processing techniques to extract phase information to complement amplitude measurements. An observed phase advance or delay in the signal could correspond with phases of growth and provide simultaneous insight into the process. Further work was laid out in [Paschal \[1988\]](#) and referred to as possible further avenues of research in [Carpenter \[1988\]](#).

Plasma Property Observations Using Satellites and Rockets

Studies using the Siple transmitter were also complemented by simultaneous observations of transmitted signals on various satellites [*Katsufrakis et al.*, 1980]. *Rastani et al.* [1985] used DE-1 observations to consider various propagation modes that could not be distinguished through observations on the ground, postulating a hybrid ducted and nonducted mode. *Inan et al.* [1977a] considered the properties of the background plasma using the well-known whistler based estimate and found good agreement with satellite measurements as tested on an Imp-6 pass. The use of whistler analysis for obtaining background parameters was verified once again by *Carpenter et al.* [1981], who found good agreement between measurements using whistler observations from Siple and Palmer Station, Antarctica (64.77° S, 64.05° W), and in-situ satellite measurements using the ISEE-1 satellite. Similarly, in-situ atmospheric measurements were made of Siple signals using sounding rocket measurements to estimate the amount of transmitted power that might reach the magnetosphere [*Kintner et al.*, 1983].

Observations of Magnetospheric Ducts Using Satellites

Other work utilized satellite measurements and observations to verify propagation conditions for whistler-mode waves. *Smith and Angerami* [1968] used OGO satellite data to characterize the difference in ducted and nonducted propagation of waves with observed whistlers. *Angerami* [1970] used data from an OGO-3 satellite pass on June 15, 1966 to show observations of whistlers in 5 discrete ducts. These observations provide the first direct evidence of ducting and some estimates on properties of the ducts through comparison with ray tracing models. The equatorial radiiuses of the ducts are estimated as 220 to 430 km with separations between the ducts of 110 to 1140 km. These observed ducts require electron density enhancements between 4% and 8%. *Inan et al.* [1977b] examined detections of Siple transmissions on the Explorer 45 and Imp 6 spacecraft, determining that Siple transmissions could be present over a large volume of the magnetosphere with a signal observed over a 6000 km path. Further study also considered the propagation of unducted, magnetospherically reflected whistlers such as finding upper and lower frequency cutoffs through

observations on the OGO-1 and OGO-3 satellites [[Edgar, 1976](#)].

Electron Precipitation

Studies also considered the effect of Siple transmissions on the energetic electron distribution through satellite measurements. In particular, electron precipitation driven by wave-particle interactions is an important topic to consider for understanding the radiation belts. A number of papers derived measurements of the amount of electron precipitation resulting from the energy loss of the electrons to the waves [[Imhof et al., 1981, 1983a,b, 1985](#); [Inan et al., 1985, 1989](#)]. Using the SEEP payload and the ISEE satellite, these studies found that VLF transmitters directly contributed to the precipitation of various energy bands of energetic electrons.

Chorus Observations During the Siple Era

[Burtis and Helliwell \[1975, 1976\]](#) studied related waves occurring in the magnetosphere and determined the properties of magnetospheric chorus using OGO-1 and OGO-3 data. The properties of chorus, such as exponential growth rates of 200 to 2000 dB/s and peak intensities between 1 to 100 pT ($m\gamma$), can be useful framing the general understanding of nonlinear wave-particle interaction conditions in the magnetosphere. Similarly, observations on the predominantly rising structure of chorus may lend insight to other phenomenon.

Contemporaneous Transmitter Experiments

[Dowden et al. \[1978\]](#) made observations at Dunedin, New Zealand, of linear and nonlinear amplification of VLF signals transmitted from a balloon-lofted antenna at Anchorage, Alaska. Although not directly related to the Siple transmitter, this was a contemporaneous experiment that yielded some similar measurements over a much more limited duration. This experiment also demonstrated the technical difficulties inherent in the use of vertical antennas.

The Precursor Phenomenon

Whistlers are sometimes observed to be preceded by discrete rising tone emissions, so called whistler precursors. *Park and Helliwell* [1977] made a number of observations using Siple and Roberval of these whistler precursors to link them with power line radiation. There is the first observation of a whistler precursor, which are discrete emissions occurring before two-hop whistlers are received, on a Siple transmitted signal [*Paschal*, 1990]. Application of phase analysis techniques [*Paschal and Helliwell*, 1984] reveal that the precursors result from momentary increases of amplification that allow emissions to be easily triggered even by the ambient background noise.

Amplitude Suppression

While many studies have focused on amplification and triggering effects in order to observe the results of wave-particle interactions, other experiments considered the reverse condition in looking at signal suppression. Amplitude suppression tended to occur in the presence of multiple waves and were found to depend on the frequency spacing and relative amplitude between the waves [*Helliwell et al.*, 1986]. Interesting examples found that signals could even suppress themselves in interactions with multi-hop components [*Raghuram et al.*, 1977], and that suppression could occur with natural signals in observing whistlers suppressing the amplitude of hiss bands [*Gail and Carpenter*, 1984].

Quasi-Periodic VLF Emissions

Using observations from Eights Station, Antarctica, *Ho* [1973] examined in more detail another type of naturally occurring VLF noise, called quasi-periodic (QP) VLF emissions, which are regular bursts of noise repeated over ~ 30 s intervals. Whistlers play a significant role in the behavior of QP emissions, by altering the QP period, modifying the QP noise structure, or by initiating QP emissions. The QP emissions also show the same upper cutoff frequencies of whistler trains occurring in the same duration.

Ionospheric Observations Using Siple

Unrelated to magnetospheric studies, [Carpenter et al. \[1988\]](#) also used transmissions from Siple detected at Palmer, Halley, and South Pole stations in Antarctica in 1983 for ionospheric studies. They noted that the relatively broadband horizontal antenna allowed for a multi-frequency probe of the Earth-ionosphere waveguide and observed that the subionsospheric receptions at the other stations were strongly dependent on the signal frequency and the arrival azimuth.

Whistler Studies

Further related work used whistler measurements to track plasmopause motion and behavior [[Carpenter, 1963, 1966](#); [Smith et al., 1981](#)]. Using whistler measurements from Eights and Byrd stations, [Carpenter \[1966\]](#) observed the position of the knee in plasma density and tracked its motion in order to define the sharp density boundary as the plasmopause. The plasmopause is then well behaved in inward motion on the nightside and outward motion on the dayside for moderately disturbed conditions ($K_p=2-4$). [Smith et al. \[1981\]](#) used simultaneous whistler recordings from Halley and Siple to study longitudinal variations in the plasmopause, such as the evidence from differences in VLF emission activity between Halley and Siple as the basis for hypothesizing the presence of irregular structures in the plasmopause. Also, as the whistlers observed at the two different stations tended to be excited by a single lightning flash, a lightning flash can illuminate a comparatively large area. In observing whistlers with Eights Station, Antarctica, [Carpenter \[1968\]](#) observed a near half-gyrofrequency cutoff effect that sharply attenuates higher frequency signals. He noted that given the wide conditions where this cutoff was observed, the effect was likely a propagation effect relating to conditions for ducting. To estimate the potential range of whistlers entering the magnetosphere, [Carpenter and Orville \[1989\]](#) examined two case studies from July 7 and August 18, 1986 to show that sferics in a large region can produce whistlers over a range of L -shell ducts and that stronger sferics can generate more intense whistlers.

2.2 Theoretical Background

Although this doctoral dissertation is primarily data driven, sufficient theoretical understanding is needed to provide context for understanding, interpreting, and applying the statistical results. Furthermore, in addition to more recent theoretical and numerical publications, a reasonable review of the body of work from the Siple era must also include some of the historical theoretical and numerical studies.

2.2.1 Plasma Theory

Plasma physics can be a complicated field of study, with complex phenomena and the need to account for additional factors such as relativistic effects. However, the fundamental equations that govern plasma behavior are actually quite straight-forward. A plasma is a quasi-neutral collection of charged particles that exhibit collective behavior and is often approximated using a fluid or a kinetic approach. Since the main numerical model used in this work as described in Chapter 4 utilizes a kinetic approach [Harid, 2015; Harid et al., 2014a], the primary equation that governs the plasma behavior is the Vlasov equation:

$$\frac{\partial f}{\partial t} + \vec{v} \cdot \frac{\partial f}{\partial \vec{r}} + \frac{q}{m} (\vec{E} + \vec{v} \times \vec{B}) \cdot \frac{\partial f}{\partial \vec{v}} = 0. \quad (2.1)$$

This equation describes the behavior of the plasma velocity phase space (hereafter referred to as phase space) distribution function f as a function of the particle motion, \vec{v} , and position, \vec{r} , and according to changes due to the presence of electromagnetic fields, \vec{E} and \vec{B} . The two constants based on the particle species are the electric charge, q , and the mass, m .

As mentioned in Section 1.1.3, electromagnetic waves propagating in the magnetosphere can interact with the plasma and modify the plasma distribution function. The waves are governed by the set of partial differential equations, known as Maxwell's Equations, as shown below:

$$\vec{\nabla} \cdot \vec{E} = \frac{\rho}{\epsilon} \quad (2.2)$$

$$\vec{\nabla} \times \vec{E} = -\frac{\partial \vec{B}}{\partial t} \quad (2.3)$$

$$\vec{\nabla} \cdot \vec{B} = 0 \quad (2.4)$$

$$\vec{\nabla} \times \vec{B} = \mu \vec{J} + \mu \epsilon \frac{\partial \vec{E}}{\partial t}. \quad (2.5)$$

The \vec{E} and \vec{B} terms respectively refer to the electric and magnetic components of the wave, and the quantities ρ and \vec{J} correspond with the electric charge and the current densities. Now, as the waves propagate through the plasma medium with the assumption that they propagate along the magnetic field lines in what are so-called ‘ducts’, they interact with the plasma, in particular the electrons, in the plasmasphere and in the radiation belts in two different ways. The low energy electrons in the plasmasphere support the propagation of waves at frequencies below the electron gyrofrequency in the whistler-mode, introducing a path delay and frequency dependent dispersion of the wave. The higher energy electrons in the radiation belts are much fewer in number and thus do not strongly affect the propagation of the wave but interact and exchange energy with the wave, resulting in wave amplification and the generation of new frequency components.

The traditional approach to analyzing the interactions of waves and particles as expressed by the Vlasov and Maxwell’s Equations is the application of linear theory. An early work by [Kennel and Petschek \[1966\]](#) linearizes the equations to compute two analytic solutions. The first result is the dispersion equation governing the propagation of the wave through the plasma, and the second describes an equation for the linear amplification of the wave, ‘linear’ referring here to the derivation of the underlying equations from linear theory. However, linear theory and linear amplification only hold when the underlying small-signal approximations remain valid. As a result, as the waves amplify or as waves with higher initial amplitudes are considered, a more general analysis of wave-particle interactions requires an analysis of the set of the complete governing equations, resulting in what is termed as nonlinear amplification. Because the underlying physical equations necessary for nonlinear amplification do not have an analytic form, they can only be solved with numerical methods.

As was mentioned in Section 1.1.3, there is a resonance condition required for these

wave-particle interactions, where the electrons and waves stay in resonance and can interact for a significant duration. An analysis of this resonance condition describes the numerical framework for selecting plasma conditions to simulate wave amplification and generation. Various theories have been proposed concerning the physical mechanism of wave-particle interactions and the generation of triggered emissions [Das, 1968; Kimura, 1967; Nunn, 1974; Vomvouridis and Denavit, 1979; Dysthe, 1971; Helliwell, 1967; Matsumoto and Omura, 1981; Trakhtengerts et al., 2003], but the general agreement is that the resonant electrons, said to be “phase-trapped” by the wave are largely responsible for the nonlinear growth. A thorough derivation of trapping can be found in Matsumoto [1985] and Omura et al. [1991, 2008]. The general idea is that the electrons in the trap exchange cumulatively substantial energy with the wave, resulting in wave amplification. After the electrons become untrapped, they can bunch together and radiate new waves to generate triggered emissions.

2.2.2 Numerical Approaches to Wave-Particle Interactions

Two review papers, Matsumoto [1979] and Omura et al. [1991], summarize a number of approaches to modeling wave-particle interactions, describing features of triggered emissions and the attempts to simulate them. These approaches consider the full governing equations within a simulation space on the order of megameters (Mm) and with particle resolutions on the order of millions of particles or grid points. These simulation spaces are chosen to approximate the region of interest where the interactions occur while remaining computationally feasible. The simulation approaches generate model outputs that can be compared with the actual nonlinear amplification and generation of waves observed in the Siple data. Here, we briefly address the three common types of numerical models that we evaluate later in this work: particle-in-cell (PIC) codes, Eulerian codes, and phenomenological models.

PIC codes model wave-particle interactions by implementing a large number of “super-particles” in order to describe the plasma behavior in response to the wave. Early codes considered just the hot electrons [Omura and Matsumoto, 1982], hybrid codes treat the cold plasma as a fluid [Kato and Omura, 2006], and full PIC

codes track both the cold and hot electrons with the super-particles. The particles are tracked in time under the influence of the electric and magnetic fields as specified by a fixed spatial grid. Currents and charges are calculated from the particle distribution on the spatial grid and then used to update the wave fields according to Maxwell's Equations. PIC simulations have successfully reproduced some wave-particle phenomenon, notably rising triggered emissions and some discrete chorus emissions [Hikishima *et al.*, 2010; Hikishima and Omura, 2012; Katoh and Omura, 2006; Omura *et al.*, 2008]. The primary limitation of the method is the large number of particles needed for the required resolution to properly represent the phase space distribution of particles.

An Eulerian approach models the plasma distribution directly by solving the Vlasov equation on a grid in phase space [Filbet and Sonnendrücker, 2003]. A semi-Lagrangian method falls under the Eulerian framework with the use of a fixed grid, but also includes a Lagrangian framework in how it traces out the particle trajectories. One particular such implementation is by Gibby *et al.* [2008]. Another Eulerian approach is used in the Vlasov Hybrid Simulation (VHS) code, which traces the single particle trajectories in time with the distribution function being interpolated onto the phase space grid [Nunn, 1993]. The VHS code has been used extensively to model VLF triggered emissions from injected whistler-mode waves [Nunn, 1990; Nunn *et al.*, 2003, 2005; Nunn and Omura, 2012] and to model chorus emissions [Omura and Nunn, 2011]. Finally, one last Eulerian approach mentioned here is a finite difference method, which discretizes the time derivatives to a difference equation. Harid *et al.* [2014a] implements the finite difference method with the additional inclusion of a relativistic coordinate transformation to create a uniform grid in phase space. The code developed by Harid *et al.* [2014a] has been used to model and explain the preferential amplification phenomenon observed in the Siple transmitter experiment in Chapter 4 [Li *et al.*, 2015a].

Phenomenological models approach the task of understanding and modeling wave-particle interactions more from an understanding of the overall physical process rather than a numerical solution of the underlying governing equations. Helliwell [1967] proposed the idea of a consistent-wave condition where the electron would be in maximum

resonance with the wave located in the interaction region, whose motion affects the resulting type of triggered emission. Following these conditions, a number of functions governing the behavior of the waves and particles can be obtained, resulting in a flexible model that could reproduce the triggered emissions with various frequency-time structures as observed in the data. *Helliwell and Crystal* [1973] developed this idea further by hypothesizing that the resonant electrons could be phase-bunched by the whistler-mode waves to create transverse current sheets that could re-radiate Doppler-shifted waves. *Trakhtengerts et al.* [2003] considered a similar approach with a phase bunched antenna model. *Carlson et al.* [1990] implemented a numerical model utilizing the model assumptions and formulation of *Helliwell and Crystal* [1973] in order to model the growth, saturation, and frequency drift of a whistler-mode wave.

2.2.3 Other Theory

Similar to Section 2.1.2, this section discusses a number of theoretical papers which explore the mechanisms governing other observed phenomena not directly related to the subject of this dissertation.

Particle Precipitation

One result of the energy exchange in wave-particle interactions is the pitch-angle scattering of electrons into the loss cone resulting in precipitation. Early theoretical work quantified the effect of waves from various sources on the amount of precipitation. *Inan et al.* [1978, 1982] used a test-particle simulation to quantitatively determine electron fluxes expected to be precipitated by waves of different amplitudes, including both linear and nonlinear gyroresonant scattering. Theoretical predictions were successfully used for direct comparison with experimental observations in the low-Earth orbit of precipitating electrons directly driven by VLF transmitter signals [*Inan et al.*, 1985] and by lightning generated whistlers [*Inan et al.*, 1989]. *Bell and Inan* [1981] considered the overall electron scattering result as dependent on resonant trapped and untrapped particles and found that even if the different populations had different pitch angle changes, the overall pitch angle change can be significant. *Chang et al.*

[1983] used a test particle simulation of particle precipitation flux and found that when wave growth increases, the precipitated energy of rising frequency signals is significantly higher than that for falling frequency signals. *Harid et al.* [2014b] considered large-amplitude coherent waves and used a Vlasov-Liouville model to demonstrate the importance of phase trapping in precipitation. These authors also showed the utility and validity of linear scattering theory for small wave amplitudes and that the frequency-time format of waves can be selected to maximize precipitation.

Propagation in Ducts

Although the dispersion of waves propagating through the plasma medium is well understood, the ducting mechanism that forms the waveguide for the whistler-mode waves is not entirely understood and has been difficult to directly observe. Generally, ducts are guiding structures formed from enhancements or depletions in the plasma density [*Haque et al.*, 2011]. *Inan and Bell* [1977] used ray tracing to demonstrate that the plasmapause can also act as a one-sided VLF wave guide.

Interactions of Multiple Waves

Interactions of multiple waves have been of significant interest, in approaching both theoretical wave-wave interactions as well as observed results such as the suppression effect [*Helliwell et al.*, 1986; *Raghuram et al.*, 1977; *Gail and Carpenter*, 1984]. *Serra* [1984] analyzed a subset of multiple wave interactions with theoretical analysis and simulations, focusing on two-wave interactions mediated through the same population of energetic electrons. The main criterion for this type of two-wave interaction to occur depends on the overlap of the trap in phase space or on the separation in frequency with some limits on wave amplitudes. Close frequency separation, <10 's of Hz, can reduce the coherence of phase-bunched electrons to result in suppression or in entrainment, where an emission couples into some external signal. Based on comparison with Siple injection experiments, *Serra* [1984] also determined that low amplitude waves and untrapped electrons can also contribute to a two-wave interaction. *Sa* [1990] further explored the theory of wave-wave interactions by proposing

that weak wave-particle-wave interactions may in fact be responsible for many triggered emissions. In particular, the magnetosphere may always be subject to weak waves radiated from power lines that can result in the proposed wave-particle-wave interactions. The consideration of multiple waves can also be used to extend the analysis of nonlinear wave-particle interactions by redefining large amplitude waves with amplitude modulation as two waves. *Tao et al.* [2013] provided a criterion for evaluating the required frequency separation for a resonance overlap to occur between waves and conducted a parametric sweep in simulation of a separation of 1 Hz to 3 kHz to show how multiple waves can approximate amplitude modulation in data and result in different scattering behaviors of the energetic electrons. *Brinca* [1972] also considers the effect of large-amplitude whistlers on the electron distribution, noting the resulting formation of large whistler side-bands. These side bands then may lend insight into the onset of triggered emissions.

Conditions for Wave-Particle Interactions (WPI)

Theoretical work has also explored other possible parameters that govern the result of wave-particle interactions. *Newman* [1977] touched on this and noted that the pulse length relative to the size of the interaction region can contribute to amplitude pulsations observed on long Siple keydown signals. *Kato and Omura* [2011] used an electron hybrid code to simulate chorus emissions and found that the amplitude corresponds with the frequency sweep rate in the simulated emissions. *Li et al.* [2015a] compared a Vlasov-Maxwell model [*Harid et al.*, 2014a] with observations in the data to show that the frequency sweep rate contributes to overall amplification of injected whistler-mode waves.

Application to Chorus Emissions

As an example of the general applicability of this work, *Cully et al.* [2011] and *Tao et al.* [2012] demonstrate the use of the wave-particle interaction theories of *Omura et al.* [2008] and *Helliwell* [1967] in predicting the frequency sweep rate behavior of chorus emissions in comparison with observations of chorus from the THEMIS

and CLUSTER satellites. It is likely the case that the understanding of the wave-particle interactions that govern amplification of injected waves and the generation of triggered emissions may also be used to describe the behavior of natural coherent waves occurring in planetary magnetospheres, in particular chorus emissions.

2.3 Experimental Archival Challenges

Due to the historical nature of the Siple data, some understanding of the recording process is required to understand the data format and the experimental limitations. We briefly discuss the original experimental setup and then discuss the challenges in reading and digitizing the historic data set, including the need for correcting errors introduced at recording and in the course of digitization. Finally, we discuss the importance of the transmission logs to illustrate the difficulty in analyzing data literally from a different era.

2.3.1 Original Experimental Setup

The overall setup and history of Siple Station and the receiving site at the conjugate location in Quebec, with a receiver first at Roberval and then at Mistissini, have been covered briefly in Chapter 1, Section 1.2.2. Here we focus more specifically on the transmitter and receiver equipment, as illustrated in Figure 1(b-c) of *Helliwell and Katsufakis* [1974], which is reproduced here as Figure 2.1. This diagram of the original experimental setup shows the overall experimental setup with the transmitter and receiver locations, as well as system components of the transmitter and receiver. The receivers, a magnetic loop antenna with a preamplifier, are similar in principle to the current generation of magnetic field sensors as described in *Harriman et al.* [2010] and *Cohen et al.* [2010b]. Due to the technological constraints of the time, WWV time markers were used for timing synchronization, and data was recorded via a magnetic tape recorder. The original configuration of the Siple transmitter is shown here with its elevated horizontal dipole antenna driven by a 100 kW amplifier modulated by a controller. By 1986, further improvements upgraded the transmitter to a pair of

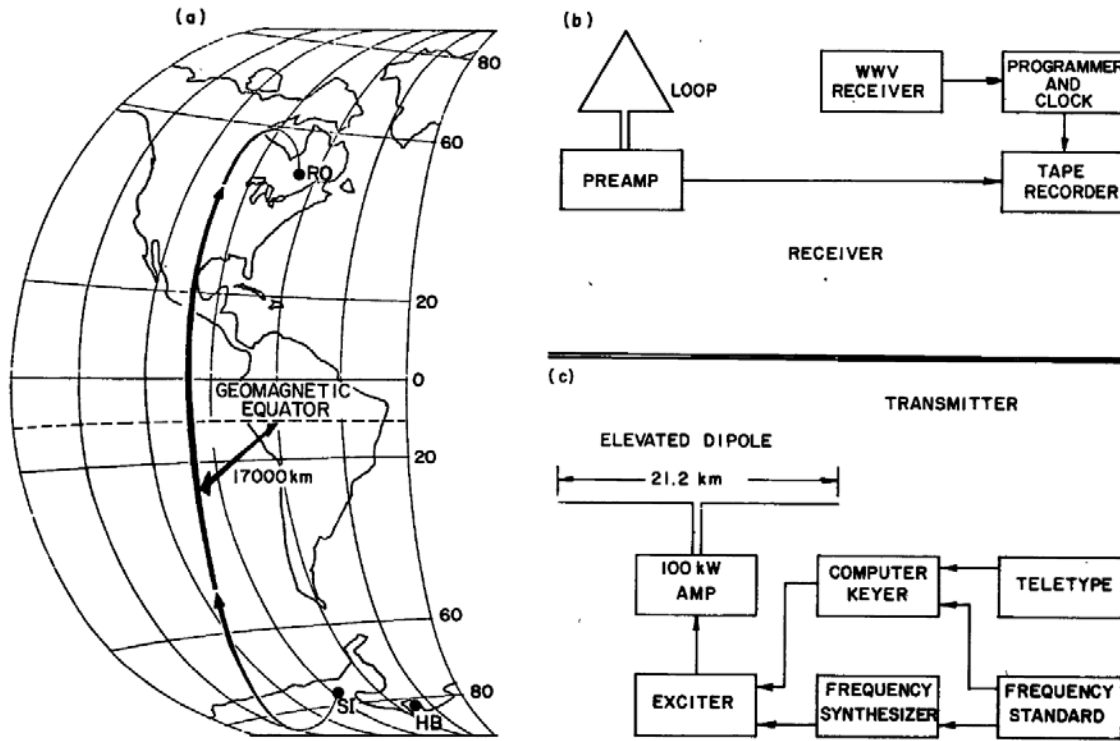


Figure 2.1: A reproduction of Figure 1 from [Helliwell and Katsufrakis \[1974\]](#) showing a sketch of the locations and magnetospheric path between the transmitter at Siple and the receiver in Quebec, Canada, originally at Roberval, and two block diagrams of the VLF receiver and transmitter.

crossed 42 km dipole antennas driven by a more flexible 150 kW transmitter.

Of particular concern for current efforts to analyze data from this era is the data storage medium and the data recording process. The data was recorded on quarter inch magnetic tape using an Ampex recorder, the use of which now is a challenge for direct analysis.

2.3.2 Archival Challenges and Digitization

After the experiment, the data tapes from Siple and the conjugate stations were shipped back to Stanford and stored in a warehouse building near the so-called Dish located on the Stanford foothills. At some point in time, with moves between different lab spaces and storage areas, the tapes were shelved and stored without any known

filling system. In addition, the physical size of the magnetic tape medium and the number of tapes, as shown in shelves of data tapes in Figure 2.2, made it quite difficult to locating specific tapes corresponding to given dates. These two factors meant that further analysis of Siple data required first digitizing large sections of the data so that relevant times and dates could be digitally and unambiguously located.



Figure 2.2: Two pictures illustrating the physical size and amount of data generated by the Siple transmitter experiment. The picture on the left is of a shelf of data in the Stanford VLF Group Data Analysis Laboratory, where the data was digitized. The picture on the right is of one row of data in storage in the VLF Data Library.

For a number of years, the VLF Data Manager would bring data tapes from the warehouse back to the Data Analysis Laboratory, where he would digitize them by reading the data using an Ampex-440C Recorder/Reproducer and passing the data through an anti-aliasing Rockland Systems Corporation Model 452 Hi/Lo Pass Filter to a National Instruments 6013 data acquisition card on a computer. The overall system digitized data with a 25 kHz sample frequency and a dynamic range

(essentially signal-to-noise ratio) of ~ 50 dB. As there was only limited storage space in the laboratory, the digitized tapes were returned to storage in the warehouse and the process of transferring the data tapes for digitization was then repeated. Through the diligent and persistent efforts of the VLF Data Manager, the data was steadily digitized, culminating in an extent of digitization as shown in Figure 2.3.

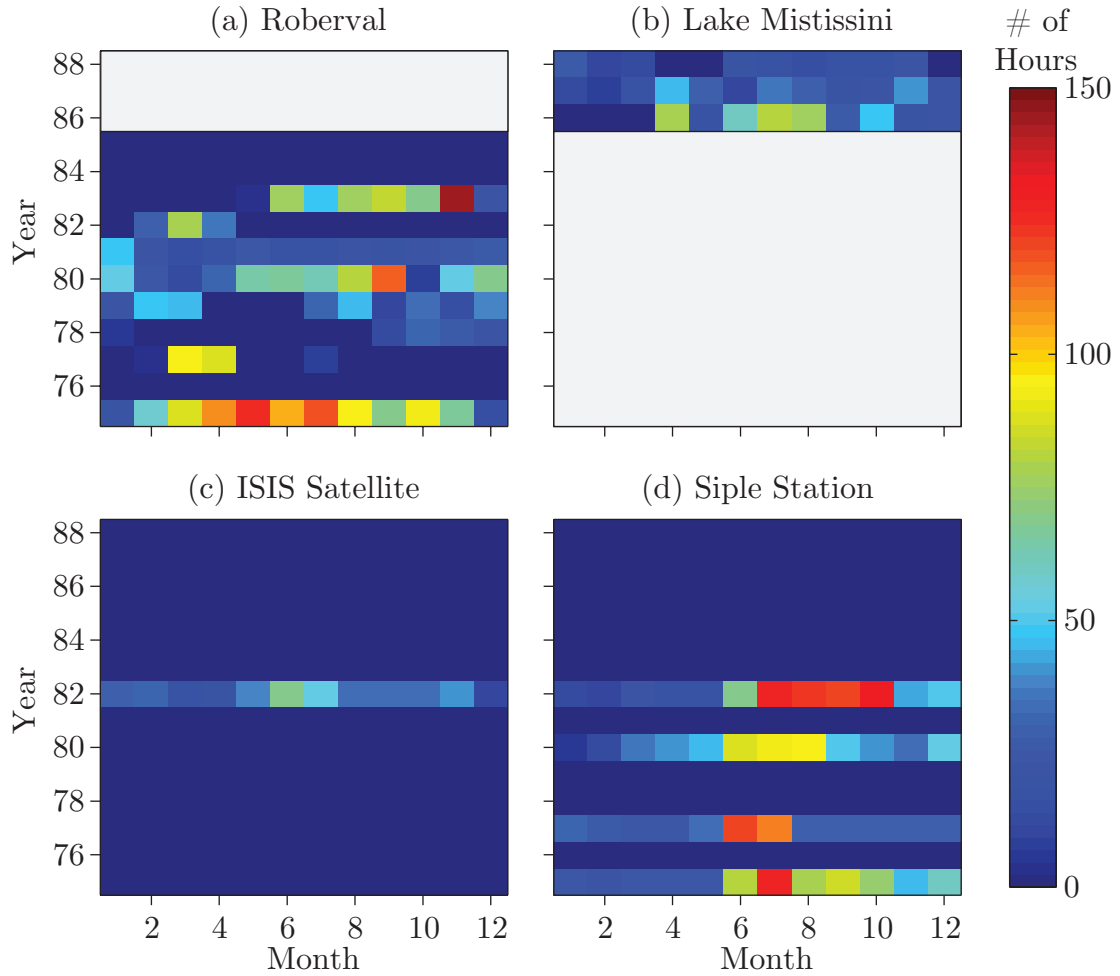


Figure 2.3: Number of hours of digitized data as a function of month and year during the Siple Station experiment. Each panel corresponds to one of four receivers, located at (a) Roberval, Quebec, (b) Lake Mistissini, Quebec, (c) ISIS satellite, (d) Siple Station, Antarctica. The Lake Mistissini receiver replaced the Roberval receiver in 1986. The white portion of the plots indicate the years when the receiver was not in operation.

The digitization efforts focused primarily on the ELF/VLF recordings made locally at Siple and in the conjugate region at Roberval and Lake Mistissini, with some selected intervals of data recorded from the International Satellites for Ionospheric Studies (ISIS), which provided low altitude in situ observations of Siple transmissions. Altogether, 6972 hours of data have been digitized, comprising 2.51 TB of data. While it is difficult to estimate with certainty the total amount of data, so far only an estimated 20% of the data has been digitized based on the amount of data still in storage.

2.3.3 Timing Correction and Alignment

The digitized data requires further preprocessing before analysis can begin. The magnetic tape recording and reading processes introduce artifacts into the data that must first be corrected. These artifacts arise as the outer layers of the tape travel faster than the inner layers of the tape, and the difference in rotational velocity results in frequency drifts in the data and offsets in time. Furthermore, tape flutter or movement during recording can introduce other time and frequency artifacts into the data. Efforts to correct these artifacts are complicated by the different timing reference methods employed during the years of the Siple experiment. For simplicity, we focus only on data from 1986, when the station had completed all improvements and upgrades. The Siple transmitter was in its most flexible and powerful configuration during this time, and a significant amount of data, relative to later years, was successfully digitized.

The timing errors can be largely corrected by examining the deviations in the phase of a reference 10 kHz pilot tone as first proposed by *Paschal and Helliwell* [1984]. As the tape speed fluctuates, at either recording or playback, the observed pilot tone frequency drifts from 10 kHz, resulting in a measurable advance or delay in the phase of the signal. To correct the frequency drift, we first apply a 175 Hz narrowband filter around the pilot tone frequency to obtain a set of sampled points from the pilot tone, y_f . The samples are complex, allowing for the use of phasor notation to represent the points by a magnitude and phase.

As the tape speed fluctuates, the phase of the pilot tone also changes. By taking a cumulative sum over a given time step consisting of n samples, we obtain the cumulative phase drift and magnitude, y_{total} as:

$$y_{\text{total}} = \sum_{k=1}^n y_f[k] \quad (2.6)$$

Here, n is set to 14 samples, or 0.56 ms of data, to handle any rapid frequency changes.

In phasor notation, we can represent y_{total} as an arc of some circle in the complex plane that geometrically describes the cumulative phase drift and magnitude of the signal. We can find the length of the chord, l , that subtends the arc and estimate the radius of the implicit circle, r_c . Then, the total change in phase, θ_c , the difference in phase over one time step, can be found from the geometry of the circle as:

$$\theta_c = 2 \sin^{-1} \left(\frac{l}{2r_c} \right) \quad (2.7)$$

The frequency correction, f_{corr} , is by definition the change in phase, θ_c , over the change in time and can be calculated as:

$$f_{\text{corr}} = \frac{\theta_c}{2\pi n} \quad (2.8)$$

By taking the cumulative sum of f_{corr} and dividing by the sampling frequency, f_s , we can interpolate and find the change in timing from the original signal, t_{interp} , as:

$$t_{\text{interp}} = \frac{1}{f_s} \sum_{k=1}^n f_{\text{corr}} \quad (2.9)$$

By scaling the timing drift, t_{interp} , with the ideal pilot tone frequency of 10 kHz, we obtain the timing difference that would result in the observed signal frequency offset. Then, we simply add this difference back to the measured signal time, t_{signal} in order to recover the timing that would correspond with a 10 kHz tone and thus

recover the original timing as:

$$t_{\text{corr}} = t_{\text{signal}} + \frac{t_{\text{interp}}}{f_{\text{pilot}}} \quad (2.10)$$

Although the timing correction is calculated only for the pilot tone, the drift in frequency and timing is assumed to be constant across frequencies, and so the correction applies to the entire signal. An example of this applied correction is illustrated in Figure 2.4, which shows the pilot tone before and after correction. In Figure 2.4(a), noticeable fluctuations in the pilot tone can be seen, with spikes that deviate up to 200 Hz, and similar errors in the Omega transmitter tone at 10.2 kHz. In Figure 2.4(b), the data has been corrected, with a majority of the pilot tone present in its 10 kHz band and similarly for the Omega tone. We also see a correction in the timing with a shift of some five seconds in this example that occurred as a result of correcting sixty minutes of the data file. While this example exhibits more serious timing errors, with some of the fluctuations in the 10 kHz pilot tone completely outside of the 175 Hz narrowband filter remaining uncorrected, a majority of the data analyzed here contains less serious frequency and timing fluctuations. This timing correction procedure effectively corrects the majority of the data but may require some adaptation for data from years other than 1986.

2.3.4 Transmission Log Transcription

In addition to the challenges posed by the need for the digitization and timing correction processes, this work with historical data faces the difficulty of obtaining the relevant experimental metadata. In particular, the recorded data alone does not provide sufficient information concerning the precise time of transmission, the tuning frequency of the transmitter, or the type of experimental transmission format. Another reason we selected data from 1986 for further analysis is the availability of a more complete set of transmission logs from 1986 detailing the mentioned experimental metadata, as well as observations of local conditions and notes detailing unexpected changes that altered the actual transmission.

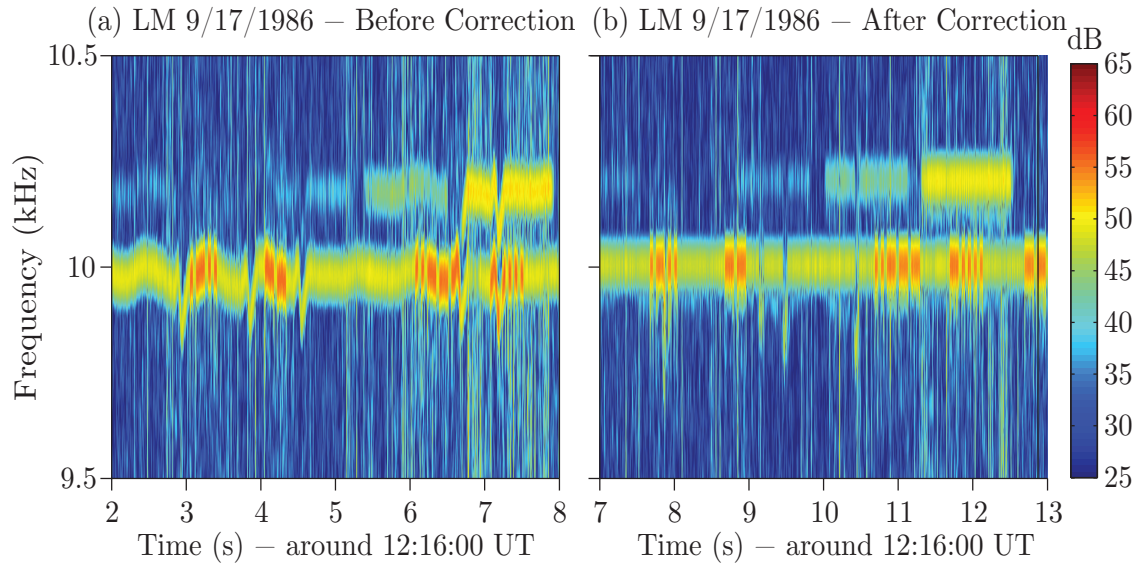


Figure 2.4: Timing Correction Example. A section of data from the Lake Mistissini receiver from 17 September 1986 illustrating the results of the timing correction algorithm. The data, prior to timing correction, is shown in (a), while the data after timing correction is shown in (b).

However, the transmission logs also require some preprocessing as they were handwritten in earlier years or typewritten as in 1986 as shown in Figure 2.5. Over two summers, two undergraduate students participating in the Stanford Research Experience for Undergraduates (REU) program worked on projects to transcribe these logs into a digital format. One student successfully utilized a commercial optical character recognition program to digitally transcribe the typewritten logs from 1986 into a searchable comma-separated values (CSV) formatted document. However, as this approach yielded poor results for handwritten logs, a later student manually transcribed the handwritten transmission logs from 1980 and 1983 into searchable Excel documents.

TRANSMISSION

LOG

SIMPLE 1979-1980

PAGE 81

SIMPLE
TRANSMITTER
PROGRAMS

1979-1980

-----START OF LOG ENTRY-----									
ENTRY: 77		ANTENNA: Cross		OUTPUT TRANSFORMER TAP: 50 ohm					

1986		POWER		TUNING		ECHO		COMMENTS	
DATE	PROG	ZULU TIME	-240	FSET	+240	FIDLE	FSET	FIDLE	POTS

Both operators at 58 HZ									

Shifted to E-W antenna only.									

23 June	TUNEF	0625-0626	90			4980			X X
	TUNEF	0627-0628	90			4020			X X
	TUNEF	0629-0630	90			3480			X X
	TUNEF	0631-0632	90			3000			X X
	TUNEF	0633-0634	90			2700			X X

Not much triggering.									

Cross antenna									
EM:LILA NS:LIL3									

EKA = 9									
Phase Shifter Pots:									
10.00 for EM									
10.00 for NS									
23 June	MDIAG	0700-0750	32/25	62/58	38/40	3.0/2.8	3480		

MDIAG is run every 30 seconds for fifty minutes.									
Not run during minutes 10 and 11.									

ground wave experiment.									
Transformer output tap is 150 ohm									
single antennas and 50 ohm									
both antennas are used.									

Tuning: EM--- NS:L4									

For Halley Bay. (East)									
Record 90 key ups.									
East. Started 10 seconds late.									
East twice.									
East north east. Keyed 10 seconds									
North east. Keyed 5 seconds late.									

North instead of north north east									
major screwup. Power is									
to incorrect xfrmr imped									
Started 5 seconds late.									

North.									

North east instead North north ve									
antennas driven from one									
Second major screwup.									

North west. Keyed 5 seconds late									

MDIAG	081845	75	4980
CMT	0820-082330	130	4980
MDIAG	082345	130	4980
CMT	0825-082830	35/30	4980

MDIAG	082845	35/30	4980
CMT	0830-083330	62/60	4980

Figure 2.5: Two pictures showing the collections of transmission logs in binders and one sample page of a typewritten transmission log from June 23, 1986. These are likely facsimiles of the original transmission logs produced for ease of reference.

Chapter 3

Characteristics of ELF/VLF Wave Amplification

One result of wave-particle interactions is the amplification of the waves. Here, we present work, of which a substantial portion has already been published as [Li et al. \[2014\]](#) in the *Journal of Geophysical Research Space Physics*. This work addresses the rather limited quantitative statistical justification that has been given for many observations and conclusions concerning wave amplification that have appeared in the literature. Statistical analysis of signal characteristics over longer time periods was not previously possible due to physical limitations on examining the data, which required processing information stored on magnetic tapes to make 35 mm spectrogram records [[Gibby, 2008](#)], and the computational requirements for analyzing the data, with at best real-time processing speed towards the last few years of operation at Siple [[Paschal, 1988](#)]. Most of the known quantitative numbers reported have been compiled from observations of single occurrences. For example, [Paschal \[1988\]](#) provides a survey of observed phenomena, including many unique individual cases. Concentration on well-defined cases may have also contributed to some bias in reception statistics in that only strong and exceptional cases were selected for detailed case study.

The lack of rigorous long-term statistics resulted in many key parameters being

coarsely estimated from early case studies and may not have been fully representative of the larger data set. For example, total temporal growth estimates of 30 dB and growth rates of 30–200 dB/s are repeatedly reported in the literature [*Helliwell et al.*, 1980; *Helliwell*, 1988a,b]. Today, it is difficult to track down which specific observations yielded these early estimates. Precise estimation of these parameters can be a powerful tool in guiding current computer simulation efforts.

While most prior studies of data from Siple Station transmissions have largely been concerned with examining individual cases with exceptional signal strength or triggered emissions, we present a more focused study of a single transmission format over the course of nine months from April to December of 1986, as the station did not operate during the austral winter. The statistics on transmission reception provide some insight into the conditions governing successful conjugate wave transmissions, and an examination of signal amplitudes and growth rates provides quantification of key parameters resulting from magnetospheric wave-particle interactions. These amplitude statistics update sparser numbers from earlier work and further constrain theoretical and modeling efforts to explain wave-particle interactions.

3.1 The Mini-Diagnostic (MDIAG) Format

Although many different formats were transmitted from Siple Station during its years of operation, we focus on the mini-diagnostic or MDIAG format from 1986. It is illustrated in Figure 3.1(a) and begins with a two-second tone at the central tuning frequency, or f_{set} , with an amplitude ramp starting at -10 dB that rises at 10 dB/s for the first second until reaching and holding constant at 0 dB for the remaining second. The two-second tone is followed by a descending staircase of five 200 ms long tones spaced 250 Hz apart from $f_{\text{set}}+500$ to $f_{\text{set}}-500$, two descending frequency ramps (the first at 0 dB and the second at -6 dB) over the same frequency range for one second each, and a seven second long pair of constant frequency tones (called a doublet) at $f_{\text{set}}+480$ and at $f_{\text{set}}+510$ at 0 dB. The central tuning frequency was selected for each transmission by the operator based on his evaluation of natural conditions. In this study, we focus on the two-second tone at the start of the format. At reception, the

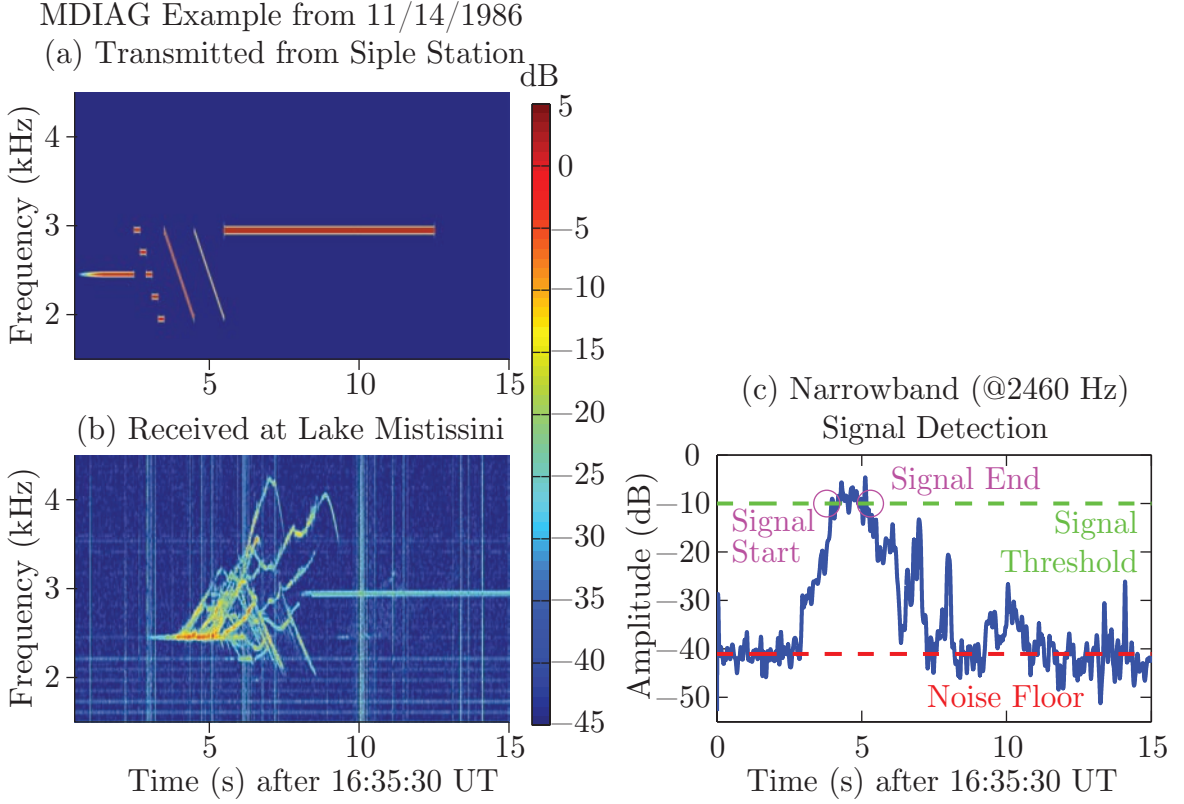


Figure 3.1: MDIAG Example. (a) the transmission format from Siple Station, (b) a received signal with triggered emissions as recorded at Lake Mistissini, (c) the main tone amplitude at the f_{set} frequency of 2460 Hz illustrating the detection of the signal using a signal threshold technique.

linear growth phase where the signal retains its built-in 10 dB/s amplitude ramp at the beginning of the tone can be differentiated from the nonlinear growth phase where the signal amplitude increases at a significantly higher rate, allowing for some insight into the behavior of transmitted signals undergoing magnetospheric amplification. The built-in amplitude ramp allows for calculation of the threshold level, which marks the transition to the phase of nonlinear signal growth. At saturation, the signal is commonly accompanied by the presence of triggered emissions, which are narrowband emissions that begin near the original signal and then sweep through a wide range of frequencies [Helliwell, 1979; Omura *et al.*, 1991].

Figure 3.1 shows an example of the MDIAG format at transmission and reception

using a spectrogram, which displays the time-frequency plot with amplitude strength marked by the colorbar, and a visual illustration of the automated detection process. Figure 3.1(a) is a spectrogram view of the signal format, as described, that would be transmitted from Siple Station. It is time aligned with Figure 3.1(b), which shows an actual received signal at the Lake Mistissini receiver, including the path delay. The signal was received cleanly and all components of the format were clearly preserved although some portions may be less distinct due to the reception of overlapping triggered emissions. A database of the transmissions was compiled by a visual inspection of processed high time and frequency resolution spectrograms of each MDIAG transmission where the reception of the MDIAG transmission was manually identified.

3.2 Reception Statistics

Table 3.1 gives reception statistics for the dataset. The reception statistics differ from previous work in that we only consider the MDIAG transmission format, as opposed to counting all signals that were observed in some duration [*Carpenter and Bao, 1983; Carpenter and Miller, 1976; Golkowski et al., 2008*]. As the data was not available for all four thousand MDIAG transmissions as only the available data tapes were digitized, our study consists of the 1074 MDIAG transmissions that were available, of which 407 cases, 38%, were received at Lake Mistissini, the conjugate point. In the case of daytime (sunlight at 100 km) operations at Siple Station, 131 of 381 (34%) transmissions were received; while in the nighttime (darkness at 100 km) at Siple Station, 276 of 693 (40%) transmissions were received. We consider the daytime and nighttime conditions only at Siple, as only 19 cases were transmitted with 9 receptions during the nighttime at Lake Mistissini and the other 1074 cases occurred during the daytime at Lake Mistissini. These reception statistics are lower than earlier results for reception of all 1-hop echoes [*Carpenter and Bao, 1983*] as the detection criteria here is specific to the MDIAG format and requires that the two-second tone at the beginning of the MDIAG be measurable rather than merely detectable.

Next, we examine the geomagnetic conditions surrounding the time of transmission, noting that 1986 was a year of overall low geomagnetic activity near the solar

	Day Time	Night Time	All Cases
Number Transmitted	381	693	1074
Number Received	131	276	407
Percentage Received	34	40	38

Table 3.1: Table of MDIAG Reception Statistics in 1986, broken down by day/night conditions at the Siple Station transmitter.

cycle minimum. We perform a superposed epoch analysis using the Kp index examining conditions from four days before to two days after the time of transmission. Figure 3.2 shows the average Kp in three hour increments in blue for all the cases when the MDIAG format was successfully received in the northern hemisphere and in red for times when the format was transmitted but not detected. To test the statistical significance of the differences in Kp values between received and not received cases, we apply a Kolmogorov-Smirnov test to evaluate if the sampled values are drawn from different underlying distributions, and note that the period of quieting leading up to the hour of transmission is statistically different for received cases, with $p < 0.01$. A similar analysis performed with magnetospherically injected signals from the HAARP facility showed a similar trend [Golkowski *et al.*, 2011].

3.3 Amplification Statistics

Next, we examine characteristics of the signal amplitudes and growth rates for the set of 407 MDIAG receptions. In order to meaningfully consider signal amplitude parameters between transmissions from different data files, we need to consider the signal-to-noise ratio at the receiver, which strongly depends on both the fixed electronic noise of the receiver and the highly variable natural noise from chorus, hiss, and lightning. The variable noise floor complicates our analysis as portions of the MDIAG reception may be below the noise floor and thus inaccessible. Lightning-generated impulses tend to dominate the injected noise characteristics [Chrissan and Fraser-Smith, 1996] but can be successfully removed with preprocessing. We can also eliminate the effects of variability in measurements from the different Ampex machines used to record data at each site by normalizing values to the constant

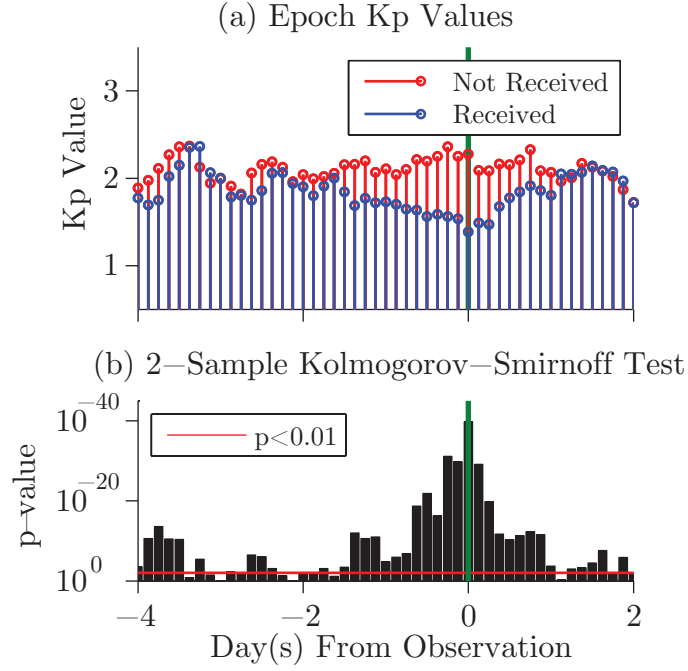


Figure 3.2: (a) Superposed epoch analysis of the average Kp-index over a six day period for MDIAG transmissions detected in the conjugate hemisphere in blue and those transmitted but not detected in red. (b) P-values for a two-sample Kolmogorov-Smirnoff statistical significance test are plotted for each 3-hour epoch interval. Note, the y-axis is inverted such that smaller p-values appear as taller bars to visually indicate significance.

calibration tone injected into the receiver.

We focus on the two-second tone at the beginning of the MDIAG format, as mentioned in Section 3.1, to obtain measurements in the following manner. First, we take four seconds of broadband data centered on the estimated time of arrival of the tone and apply a preprocessing technique to remove sferics developed within our research group. Here, we use a sparse separation technique [Strauss, 2013, Section 2] to detect and remove the sferics. Then, we multiply the broadband signal by a complex exponential in order to shift it down to baseband from the f_{set} carrier frequency specified in the transmission logs. Using a low pass filter with a 100 Hz bandwidth, we extract the narrowband signal. After smoothing with a ten point median filter to further reduce impulsive noise, we normalize the signal using the

closest preceding reference calibration tone. The narrowband signal amplitudes for all 407 cases provide measurements of the saturation power level and the nonlinear growth rate as illustrated in Figure 3.3(a). Here, the noise floor (dashed red line) dominates until the high nonlinear growth rate (dashed orange line), 159.5 dB/s in this case, causes the signal to rise out of the noise floor. Growth then stops at saturation (dashed green line). However, for a subset of fourteen cases, identified here as Subset 1, additional parameters of the signal can be quantified as shown in Figure 3.3(b). The distinguishing feature of Subset 1 is that the initial signal level (dashed black line) is distinct from the noise floor. Next, the built-in 10 dB/s amplitude ramp (dashed yellow line) can be seen. At some amplitude level, indicated as the nonlinear threshold (dashed cyan line), the growth rate drastically increases. The signal grows at this higher nonlinear growth rate until it reaches saturation as before.

For an MDIAG signal to be received at Lake Mistissini, the transmitted whistler-mode VLF wave typically experiences some type of cyclotron resonance growth as a result of interaction with energetic electrons in the near-equatorial magnetosphere. The growth resulting from this interaction can be divided into two phases: 1) linear or spatial growth wherein all portions of the signal are amplified to the same degree and 2) nonlinear or temporal growth wherein later portions of the signal are amplified more than earlier portions. The MDIAG format was designed in order to excite wave amplification and evaluate the power threshold needed to trigger nonlinear amplification [Helliwell *et al.*, 1980]. For this reason, the format includes a 10 dB/s amplitude ramp at the start of the transmission. For the Subset 1 cases, the signal growth from the initial level to the saturation level goes through two distinct phases. Figure 3.3(b) clearly shows that the first amplitude ramp is 10 dB/s (equivalent to the power increase at the transmitter). This observed 10 dB/s amplitude ramp is indicative of the phase of linear signal growth. The originally transmitted 10 dB/s amplitude ramp is preserved and all portions of the received signal are amplified by the same amount according to expectations from linear theory. The amount of linear growth itself is not measurable by a ground-based VLF receiver precisely because all portions of the signal are amplified identically. At the nonlinear threshold level, the

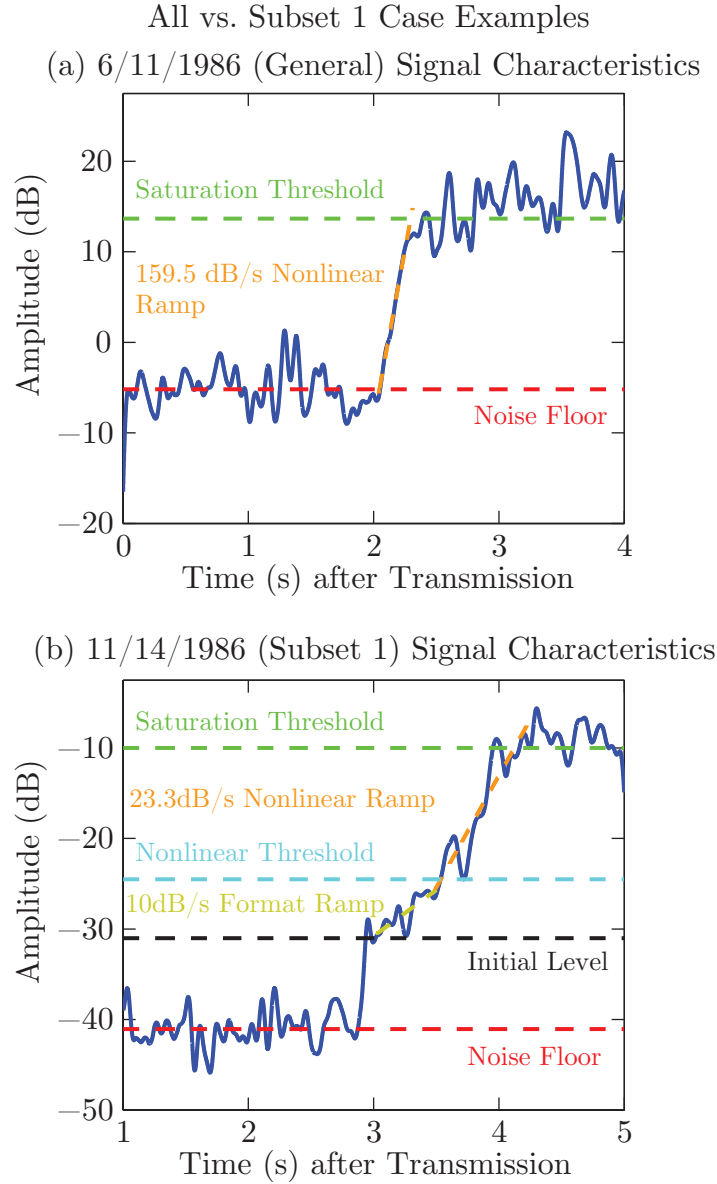


Figure 3.3: General (a) and Subset 1 (b) MDIAG cases. General cases describe the cases where the signal rises up from the noise floor (dashed red line), undergoes nonlinear amplification (dashed orange line), and then saturates (dashed green line). Subset 1 cases describe cases where the signal is received clearly distinct from the noise floor (dashed red line) at some initial power level (dashed black line), undergoes a phase of linear amplification that can be identified by the presence of the injected 10 dB/s amplitude ramp (dashed yellow line), reaches some growth threshold (dashed cyan line), experiences nonlinear amplification (dashed orange line), and then saturates (dashed green line).

amplitude slope suddenly switches to exceed the original 10 dB/s slope. This portion is indicative of temporal growth as later portions of the signal are amplified more than earlier portions. In the majority of received cases, only the later, temporal or nonlinear growth portion of the signal is detectable, and the nonlinear growth rate is determined by measuring the slope of the signal power as it rises from the noise floor to the saturation level.

Past observational studies [e.g. [Helliwell et al., 1980](#); [Helliwell, 1988a](#); [Sonwalkar et al., 1997](#)] refer to the two phases of observed signal growth as the spatial and temporal (or exponential) growth phases. However, more recent theoretical works [e.g. [Omura et al., 2008](#); [Gibby et al., 2008](#)] have shown that the two growth phases can be described by linear and nonlinear theory, respectively. In order to focus on physical processes rather than observed phenomena, we will henceforth refer to the growth phases as linear and nonlinear.

First, we consider the general set of cases, for which only the nonlinear growth portion is visible, and analyze the saturation level, the nonlinear growth rate, the noise floor, and the f_{set} tuning frequency. Figure 3.4(a) shows the lack of statistically significant correlation between the nonlinear growth rate and the saturation power level, that is a higher nonlinear growth rate does not necessarily result in higher signal amplitude (consistent with the results from [Sonwalkar et al. \[1997\]](#)). We do, however, find a significant ($\rho = 0.73, p < 0.01$) correlation between the noise floor and the saturation power level as shown in Figure 3.4(b). The noise floor in the band of Siple transmission is highly variable, covering a range of about 80 dB. Since preprocessing of the data includes sferic removal, the remaining variability in the noise floor is largely due to occurrence of magnetospheric emissions including bands of hiss or chorus. As further discussed in Section 4, this suggests that when conditions are favorable for the linear amplification of magnetospheric noise, Siple signals are also able to achieve higher total amplitude. However, the rate at which signals grow to saturation appears to be independent as the nonlinear growth rate is not correlated with either the saturation level (Figure 3.4(a)) or the noise level (not shown).

Figure 3.4(c) examines the nonlinear growth rate as a function of the f_{set} transmission frequency. There are relatively few columns as only a fixed number of discrete

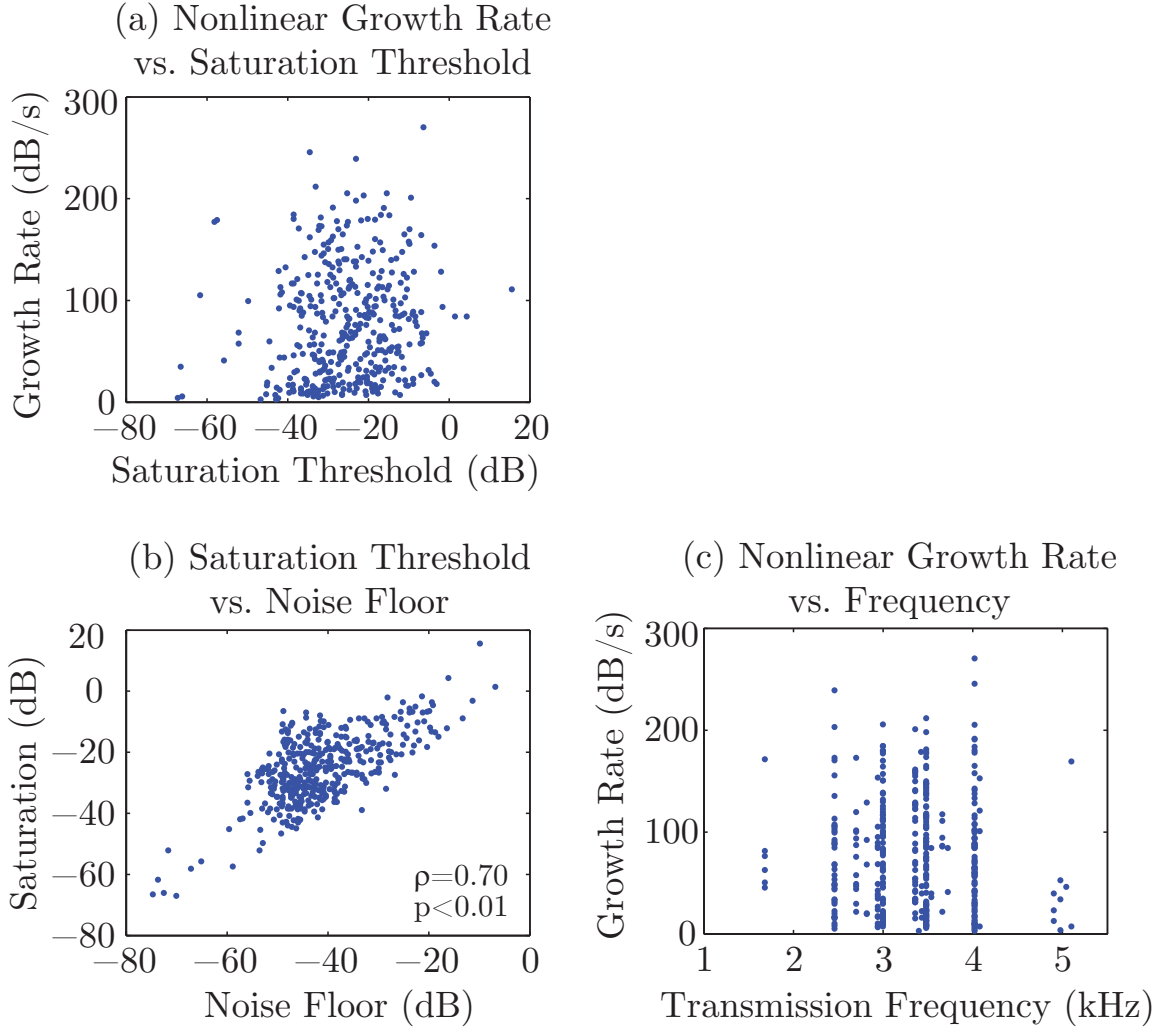


Figure 3.4: Comparison of (a) the nonlinear growth rate against the saturation power level, (b) the saturation power level versus the noise floor [$\rho = 0.73p < 0.01$], and (c) the nonlinear growth rate against the f_{set} tuning frequency.

f_{set} frequencies were used for transmissions. Overall there is no correlation between nonlinear growth rate and f_{set} , and furthermore, for a given f_{set} , the nonlinear growth rate is relatively uniformly spread over a wide range of values (consistent with the results from [Carpenter et al. \[1997\]](#)). We note that all transmissions were below 0.5 of the equatorial gyrofrequency, which for the location of Siple corresponds to about 6 kHz.

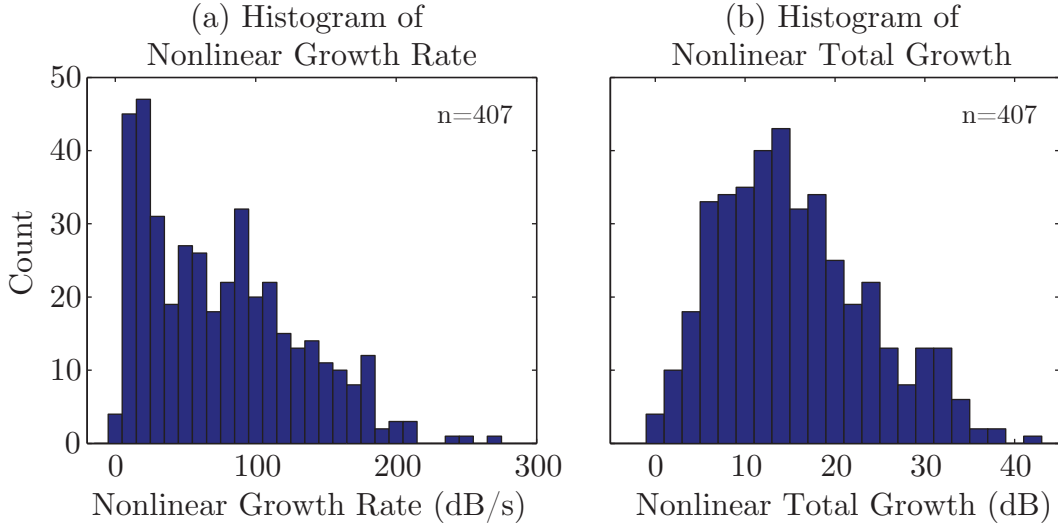


Figure 3.5: Histograms illustrating the range of (a) nonlinear growth rates and of (b) the nonlinear total growth.

Figure 3.5(b) is a histogram of the nonlinear growth rates, which range from 3–270 dB/s with a median growth rate of 68 dB/s, matching well with observations from previous work. The other comparison with earlier work [*Helliwell and Katsufakis, 1974*; *Helliwell et al., 1980*] is a comparison of the total amplification, or total growth. While there is reason to suggest redefining this observed growth as a pseudo-total growth due to the uncertainty of any amplification below the noise floor, we continue with the accepted definition in terming this to be the total nonlinear amplification. Figure 3.5(b) is a histogram of the total growth, calculated as saturation level minus noise floor, for all received cases, showing a spread of 3–41 dB and a median total growth value of 18 dB. While these values are still in the same range as the values from past work [*Helliwell and Katsufakis, 1974*; *Helliwell et al., 1980*], the often cited 30 dB value should likely be adjusted to ~ 20 dB. While this new value only definitively applies to data from 1986, this update has more statistical justification than the original value and there is no reason for this result not to represent the general case.

Next, we examine the 14 Subset 1 cases, which occurred on four separate days and include measurements of the nonlinear threshold level, that is the amplitude at which

the growth changes from linear to nonlinear. Figure 3.6(a) compares the saturation level with the threshold level. There is no statistically significant correlation, implying that the total nonlinear growth should decrease as the threshold level increases. This, in fact, can be seen in Figure 3.6(b), which plots the total nonlinear growth against the threshold level and shows strong negative correlation ($\rho = -0.86$, $p < 0.05$). The total nonlinear growth is in the range of 5–30 dB.

Further, the nonlinear growth rate is also uncorrelated with both the threshold level (Figure 3.6(c)) and the saturation level (not shown, but consistent with Figure 3.4(a)). Finally, in Figure 3.6(d) we see the strong negative correlation ($\rho = -0.74$, $p < 0.05$) between the nonlinear growth rate and the nonlinear growth duration. Signals with higher nonlinear growth rates grow for a shorter time period while signals with lower growth rates

3.4 Discussion

The statistical analysis of data from the Siple Station experiment enables observation-driven evaluation of physical models of resonant, nonlinear growth. The analysis presented here provides statistical verification of generalized observations from past work and provides insight to theoretical studies. Current prevailing theory holds that temporal growth and the generation of free running emissions is the result of nonlinear gyro-resonant interactions between whistler mode waves and resonant particles [Omura *et al.*, 1991; Hikishima and Omura, 2012; Nunn and Omura, 2012]. As shown in Figure 3.3(b), the injected signal grows first according to linear theory and then, after passing the power threshold, abruptly switches to a regime of nonlinear growth. This nonlinear growth is generally attributed to nonlinear phase trapping of resonant electrons. As particles move away from the equator, there is a finite wave amplitude required for trapping. Recent work on the theory using numerical simulations, previously limited due to insufficient computing capability, has also demonstrated that the trapping mechanism results in a depletion of electron density in phase space known as a “phase-space hole” which appears to be responsible for many of the nonlinear effects. The formation of this phase space structure, which takes a finite amount of

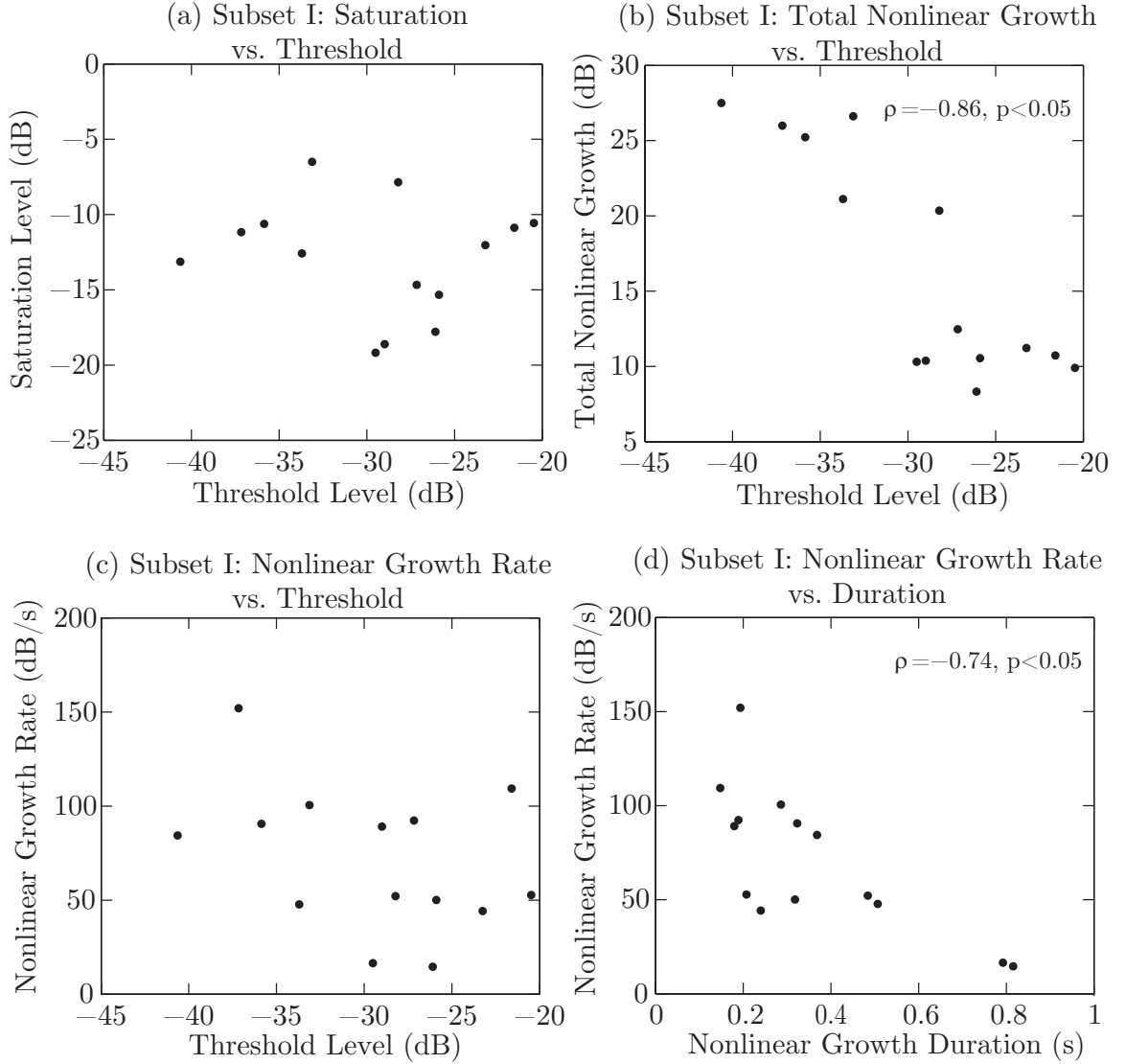


Figure 3.6: Comparison amongst threshold power level, saturation power level, total growth, and the nonlinear growth rate and duration using the set of cases where the initial and threshold power levels were clearly distinguishable from the noise floor. ρ values are given only for statistically significant, $p < 0.05$, correlations. We compare (a) the saturation power level, (b) the total growth, and (c) the nonlinear growth rate with the threshold power level, while (d) compares the nonlinear growth rate with the nonlinear growth duration.

time, along with the finite amplitude for trapping, may be responsible for the finite transition time between linear and nonlinear growth [Dowden *et al.*, 1978; Vomvoridis and Denavit, 1979; Omura *et al.*, 2008; Hikishima and Omura, 2012].

The analysis of two-second tones transmitted by Siple and received in the conjugate hemisphere allows us to statistically quantify the nonlinear growth rate, saturation level, and estimate the total signal growth. The transmission format includes a 10 dB/s amplitude ramp during the first second, which allows us, in a small subset of cases, to separate the linear growth phase from the nonlinear growth phase and determine the threshold amplitude at which that occurs. We find that the nonlinear growth rate varies between $\sim 5\text{--}270$ dB/s, but the nonlinear growth rate does not depend on 1) the transmission frequency (within a narrow range below 0.5 of the equatorial gyrofrequency), 2) the noise floor, 3) the threshold amplitude or 4) the saturation level. The lack of correlation between these quantities suggests that once a signal reaches the threshold amplitude, it proceeds to undergo nonlinear growth, but our observations do not provide insight on what controls the value of the nonlinear growth rate. Further, we find that as the nonlinear growth rate increases, the nonlinear growth time decreases. Also, as the threshold level increases, the total nonlinear growth decreases. These last two observations suggest that the saturation level, though not constant, is bounded.

We also find that the saturation level is linearly correlated with the measured noise floor. Lightning generated sferics contribute significantly to the noise floor in this frequency range, and two data processing techniques were used to minimize the effects on sferics on the data (autoregressive sferic removal on the broadband data and median filtering of the extracted narrowband signal). Even after sferic removal, the noise floor during the observations varies over a range of ~ 80 dB, as seen in Figure 3.4(b). In examining the individual case records, we find that events with significantly higher noise (above -15 dB) often occur in the presence of a band of magnetospheric emissions such as hiss and chorus. Figure 3.7 shows two example records with and without the presence of a band of hiss. The hiss band contributes to a 35 dB higher noise floor (red dashed line), and the saturation amplitude in the hiss case is 11 dB higher. The nonlinear growth rate for the two cases is similar (black

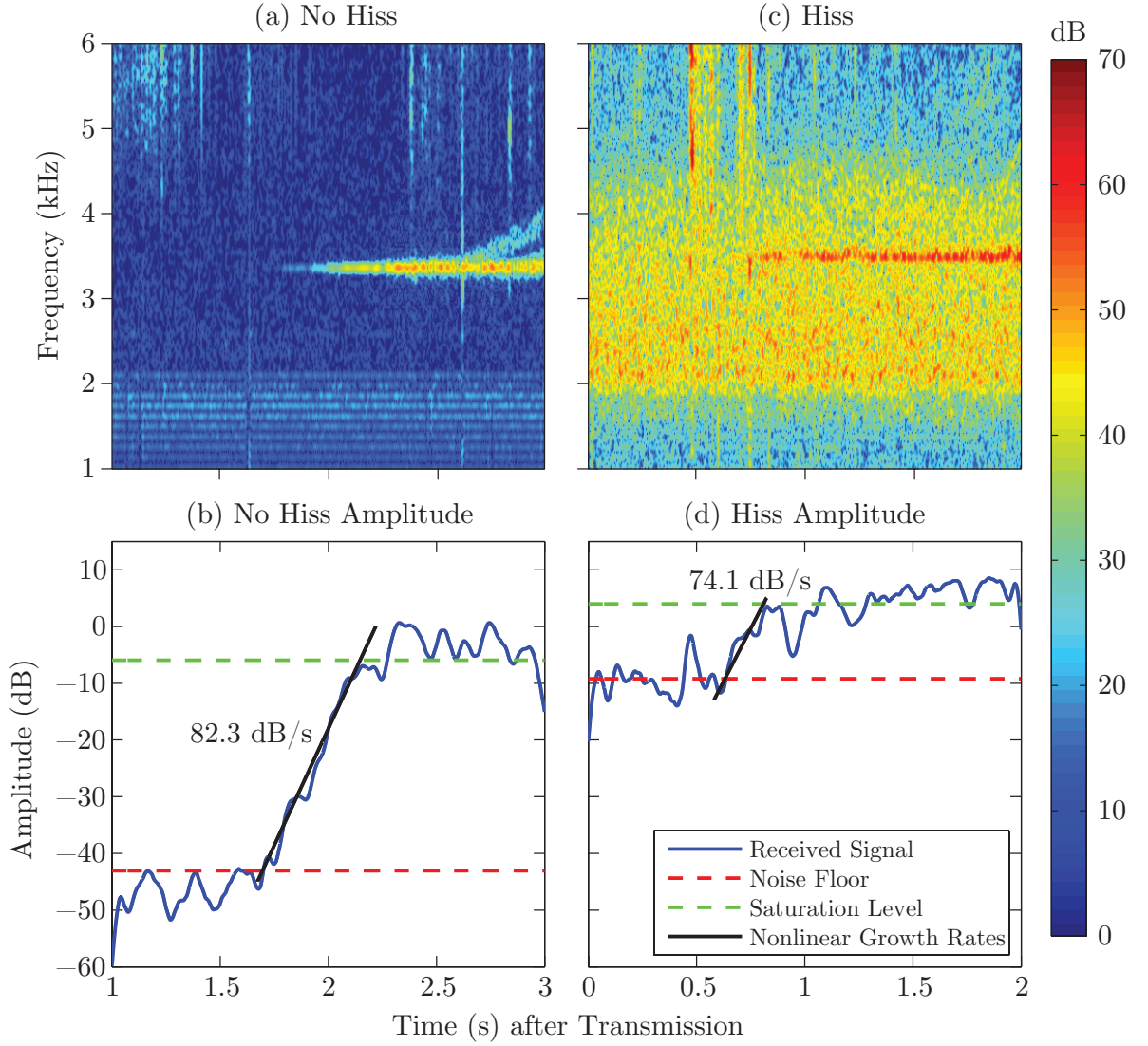


Figure 3.7: Comparison of two received transmissions with and without hiss. The spectrograms show (a) the lack of and (b) the presence of a hiss band. The corresponding narrowband analysis at the f_{set} transmitter frequency shows (a) lower noise and saturation levels for the no hiss transmission and (b) higher noise and saturation levels for the transmission with hiss, even though the nonlinear growth rates are similar.

line), but the duration of observed nonlinear growth is nearly twice as long for the transmission without a hiss band. These observations indicate the possibility that stronger magnetospheric activity correlates with higher saturation and noise levels,

and this suggests that the saturation level is influenced by the linear growth rate. In contrast the lack of correlation between the nonlinear growth rate and saturation, threshold and noise level suggests that the nonlinear growth rate is somewhat independent of the linear growth rate.

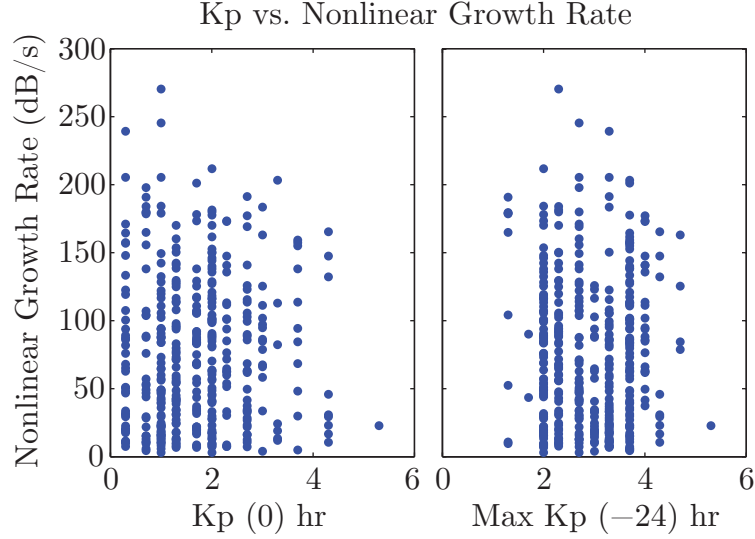


Figure 3.8: Two panel figure correlating nonlinear growth rate in dB/s with the Kp index for all cases. The left panel compares the nonlinear growth rate with the Kp value at the time of transmission and reception, while the right panel makes the same comparison with the maximum Kp value in the last 24 hours.

To further investigate these ideas, we correlate the nonlinear growth rate and the saturation level with measures of the geomagnetic activity. Figure 3.8 plots the maximum value of the Kp index in the 24 hours preceding the Siple transmission with a) the saturation level and b) the nonlinear growth rate but shows no correlation in either quantity. Comparisons with the AE and SYM-H index produce a similar lack of correlation. It is likely that the global nature of geomagnetic indices does not well represent the conditions in an isolated magnetospheric duct, and that the presence of natural emissions remains as the best indicator of local conditions for wave growth.

3.5 Conclusions

A major effort has been undertaken to restore and preserve data collected during the Siple Transmitter Experiment. Nearly 7000 hours of data have been digitized from magnetic tapes, and algorithms have been developed to eliminate frequency drifts and timing errors inherent in the data. The analysis presented here focuses on a frequently transmitted diagnostic format (MDIAG) that included a two-second tone and allows for determination of the nonlinear growth rate, saturation level and an estimate of the total growth, which is dubbed the pseudo-total growth as it cannot take into account growth from below the highly variable noise floor. In a subset of cases the two regimes of linear and nonlinear growth can be separated.

For the 1986 interval examined here, the reception rate of the MDIAG format is consistent with past observations with 38% of MDIAG transmissions from Siple received at the conjugate hemisphere. Nighttime ionospheric conditions at the transmitter led to slightly higher (40%) reception rates, likely due to decreased trans-ionospheric absorption [e.g. [Graf et al., 2013](#)]. We find that the average geomagnetic conditions, as described by the Kp-index, for successful transmissions is characterized by a highly statistically significant period of quieting compared with the undetected transmissions. At the time of transmission, the Kp-index is 0.84 units lower when the signal is received than when it is not. This result matches with similar observations made by [Golkowski et al. \[2011\]](#) for the successful reception of two-hop signals using HAARP. [Golkowski et al. \[2011\]](#) interpreted the correlation of conjugate reception to geomagnetic quieting as stemming from the conditions for optimum stability of ducted propagation paths. The results reported here are consistent with that interpretation.

The total nonlinear growth for the events examined here is in the range of 3–41 dB with a median growth of 18 dB, and the nonlinear growth rates are in the range of 3–270 dB/s with a median growth rate of 68 dB/s. The observations show that as the nonlinear growth rate increases the duration of nonlinear growth decreases, and also that as the threshold amplitude (the amplitude at which growth changes from linear to nonlinear) increases the total nonlinear growth decreases. Both of these observations

suggest that the saturation level is bounded. Further, the correlation between saturation level and increases in the noise floor due to natural magnetospheric emissions suggests that the absolute saturation level is controlled by the linear growth rate. The lack of correlation between the nonlinear growth rate and the noise, threshold and saturation levels suggest that the nonlinear growth rate is independently controlled and may be independent from the linear growth rate.

Chapter 4

The Preferential Amplification Phenomenon

In this chapter, we use statistical bounds on wave amplification derived from observations to constrain theoretical interpretation and numerical simulations of wave-particle interactions. We present work, a substantial portion of which has been published as [Li et al. \[2015a\]](#) in the *Geophysical Research Letters*, in considering one particular amplification phenomenon called preferential magnetospheric amplification. Using observations of ground-based ELF/VLF observations of injected whistler-mode waves from the 1986 Siple Station experiment, we quantify the preferential amplification of rising over descending frequency-time ramps. From examining conjugate region receptions of ± 1 kHz/sec frequency-time ramps, we find that rising ramps generate an average total power 1.9 times higher than that of falling frequency ramps when both are observed during a transmission. Further, in 17% of receptions, only rising ramps are observed above the noise floor. We also find that the amplification ratio inversely correlates with the noise and total signal power. Using a narrow-band Vlasov-Maxwell numerical simulation, we explore the preferential amplification of rising ramps resulting from differences in the linear growth rate as a function of frequency and nonlinear phase trapping. These results contribute to the understanding of magnetospheric wave amplification and the preference for structured rising elements in magnetospheric chorus emissions.

4.1 Statistical Observations of Preferential Amplification

The staircase coherence format, abbreviated STACO, transmitted by Siple Station from July to December of 1986 is illustrated in Figure 4.1(a) and is composed of two identical sets of rising, 1 kHz/s ramp elements (Riser 1 and Riser 2), followed by two identical sets of falling, -1 kHz/s ramp elements (Faller 1 and Faller 2). Each ramp set is composed of five elements that are approximations to an ideal frequency ramp using 1 ms, 10 ms, 25 ms, 50 ms, and 100 ms long tones with each ramp being 1 second in total duration. The entire transmission is centered on an operator selected tuning frequency, f_{set} , which ranged from 1680 Hz to 4020 Hz. Data from the conjugate receiving station is available for 170 transmissions of the STACO format, and 63 receptions were detected for a 37% reception rate. Of those detected, 60 were received with sufficient signal to noise ratio for further analysis. The format was originally intended for studying the required time-frequency spacing to approximate a continuous frequency ramp [Mielke and Helliwell, 1993].

The goal of the current study is to compare the total magnetospheric amplification, which includes both the amplification of the transmission and the generation of triggered free running emissions, resulting from the injection of rising versus falling frequency ramps. We develop a metric to calculate the total signal power generated from each set of ramp elements, and we make comparisons between rising and falling sets only within a given transmission in order to eliminate variations due to changes in background conditions. To calculate this metric, we manually identify a set of rising or falling ramps, preprocess to reduce interference from lightning generated sferics using a sparse separation technique [Strauss, 2013, Section II]. Then, we apply a 75,000-point fast Fourier transform with proper scaling for the signal duration and filter the result using a 1000-point median filter to further remove impulsive noise in the frequency domain, such as power line harmonics and single frequency fluctuations in the background noise. We integrate over a 3 kHz window centered on f_{set} and identify this number as the uncalibrated power metric for the signal using Parseval's theorem. We also apply this same methodology to a manually selected segment of

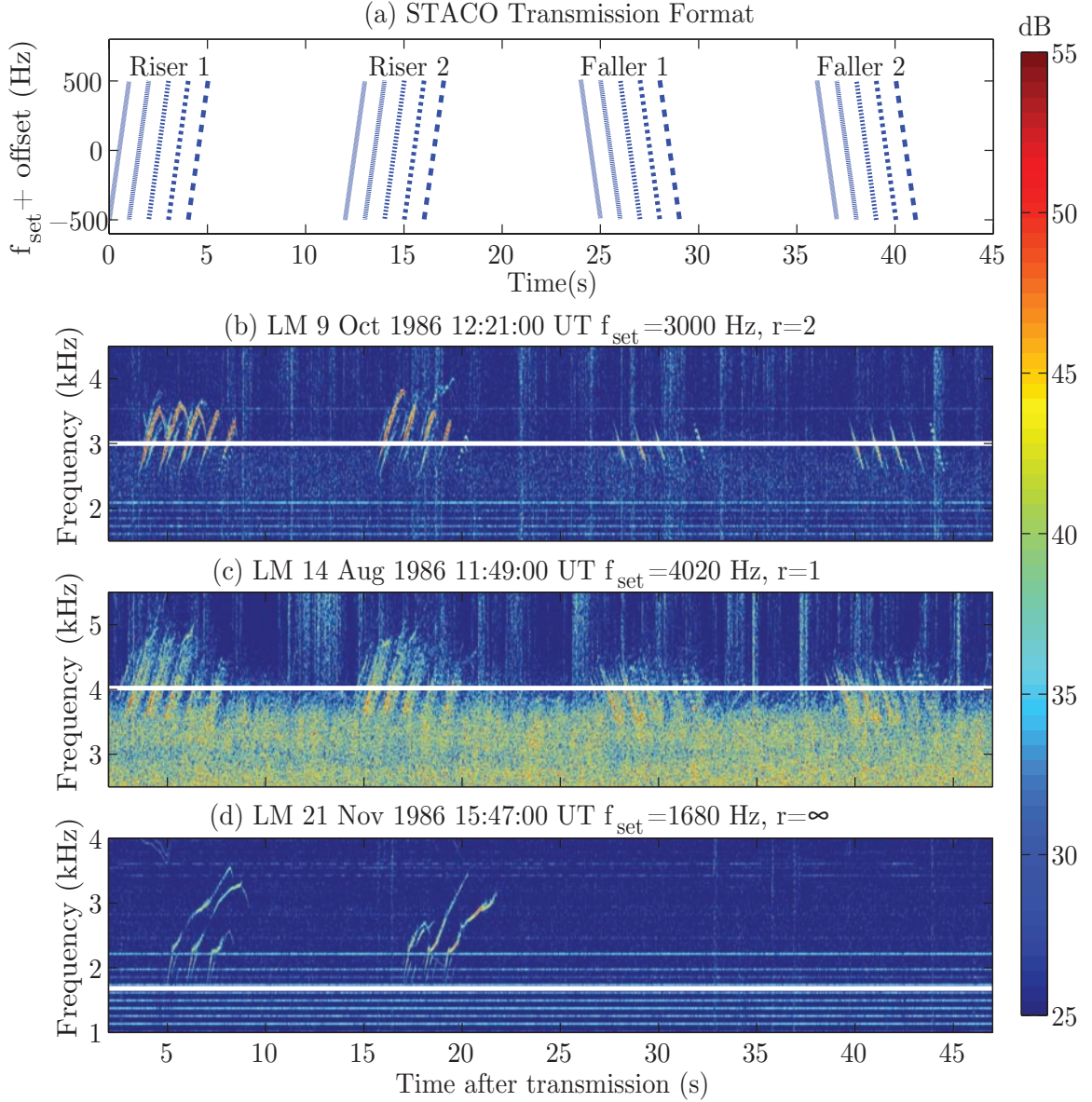


Figure 4.1: (a) Illustration of the STACO format transmitted by Siple and conjugate receptions with riser to faller amplification ratios of (b) $r = 2$, (c) $r = 1$, and (d) $r = \infty$.

data from several seconds prior to or following the ramp set to characterize the local background noise around the time of the ramp reception. This noise power is then

subtracted from the signal power metric to obtain a single number for the amplification metric. The amplification ratio (r) is then the ratio of the amplification metric for different sets of ramps within a transmission, such as Rising to Falling or Rising 1 to Rising 2.

Figure 4.1(b-d) shows examples of receptions of the STACO format for three different amplification ratios. Figures 4.1(b-d) are aligned in time and are shifted 3 seconds from Figure 4.1(a) to account for propagation delay. The first example, (b), shows a case where the Rising to Falling amplification ratio is about 2 and exhibits stronger amplification of the transmitted rising signals, triggered emissions (downward hooks at the top of the rising ramps), and visible multipath effects. The Siple transmissions are believed to reach the conjugate hemisphere primarily in a ducted propagation mode [*Carpenter and Sulic, 1988*], and multipath refers to the phenomenon where the transmission propagates in multiple magnetospheric ducts simultaneously. Multipath effects can be seen on the spectrograms in Figures 4.1(b-d) as additional receptions within a 0.5 s window. In Figure 4.1(c), the Rising to Falling amplification ratio is near unity, with both risers and fallers appearing similar in intensity and embedded in a band of hiss. Finally, Figure 4.1(d) is an example where the fallers are not detected (deemed $r = \infty$) while some significant portion of the risers are detected and generate rising tone triggered emissions that extend > 1 kHz above the transmitted ramp.

The distribution of amplification ratios for all received transmissions of the STACO format is shown in Figure 4.2. The histogram in Figure 4.2(a) presents the amplification ratio for Riser 1 to Riser 2 sets, in order to evaluate any possible difference in amplification due to temporal effects. The median value of r is 1.06 and 61% of cases have values of r between 0.75 and 1.25. The histogram in Figure 4.2(b) shows the distribution of the amplification ratio for Rising to Falling ramps. We note that the bin with highest occurrence ($n=10$) is the infinite ratio bin, that is, the falling ramps are not received at all. The median value of the ratio, not including the infinite cases, is 1.93, and 12 cases (20%) have a r value less than 1, that is fallers are amplified more than risers. Of those 12 cases, 5 cases have $r > 0.8$, 4 cases have $0.8 > r > 0.5$, and 3 cases have a $0.5 > r > 0.3$. The results from Figure 4.2(a), that

subsequent ramps have an amplification ratio near 1, suggest that the differences in the rising to falling amplification are unlikely to be due to temporal effects within a given transmission. Figure 4.2(c) shows a scatterplot of the noise power versus the rising to falling amplification ratio, where the dividing $r = 1$ line separates the two regions of differing behavior. As we have an insufficient number of cases where $r < 1$, we examine cases only where the risers are amplified more than fallers and the fallers are received (that is $1 < r < \infty$), and find that as the noise power increases, the amplification ratio decreases. The correlation coefficient between noise power and amplification ratio in that range of r is -0.46 ($p < 0.01$). *Li et al.* [2014] reported that the primary contribution to the increase in noise power for Siple receptions is the occurrence of natural emissions such as hiss, as seen in Figure 4.1(c), and as such, intervals of higher noise power likely indicate when the conditions for linear growth are enhanced. As applied to Figure 4.2(c), lower noise power suggests lower linear growth rates which are then associated with higher amplification ratios. Figure 4.2(d) shows a scatterplot of the total power of the rising ramps versus the rising to falling amplification ratio with a similar trend of the rising power metric increasing as the amplification ratio decreases. We also examined the relationship between the amplification ratio and the f_{set} frequency, the Kp index at the time of transmission, and the local time of transmission, and found no correlation.

4.2 Theory and Modeling of Preferential Amplification

Modeling the propagation and growth of whistler-mode waves interacting with energetic radiation belt electrons requires solving the Vlasov-Maxwell system of equations. The evolution of the electron distribution function is governed by the Vlasov equation while the wave fields are generated according to Maxwell's equations. Under the assumption of parallel propagating signals, which ducted Siple signals are considered to be, the interaction between waves and particles is dominated by cyclotron resonance.

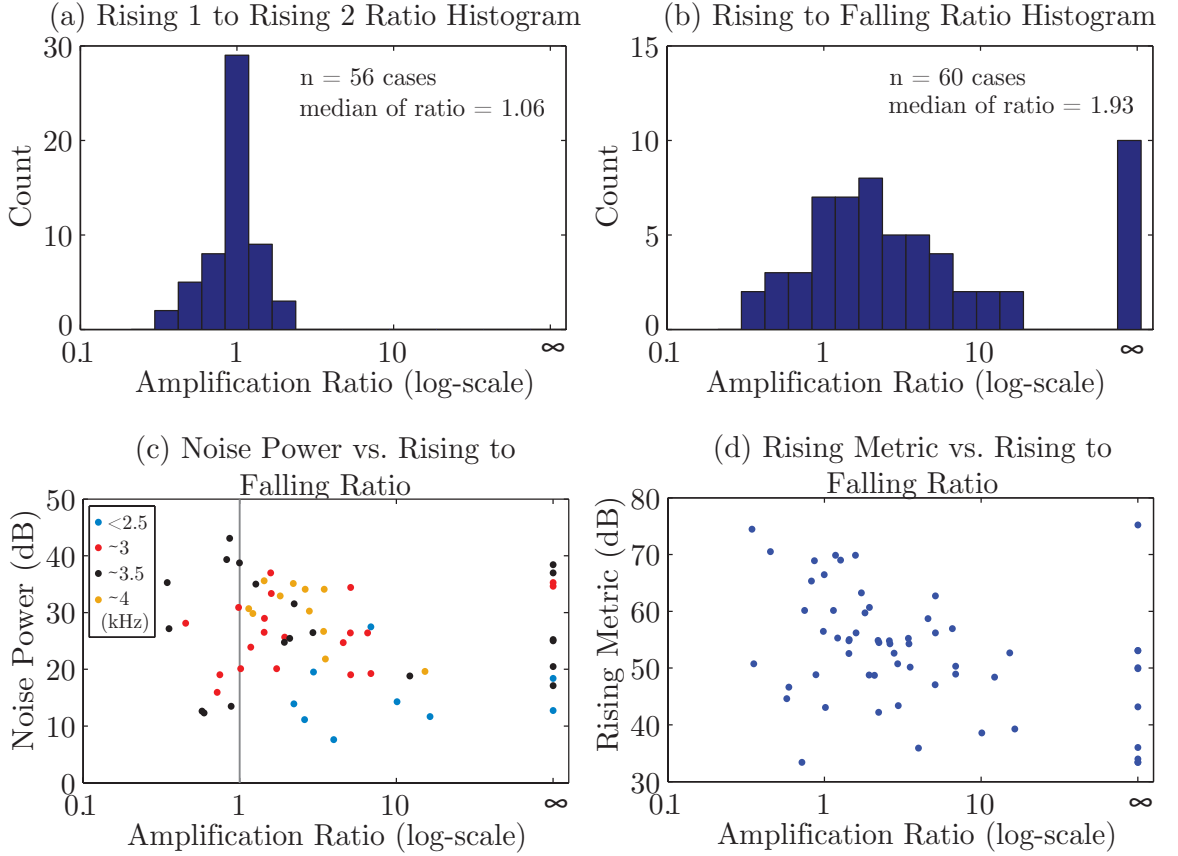


Figure 4.2: Results from the statistical analysis of the STACO format. The histograms show (a) the amplification ratio between the sequential rising sets, Riser 1 and Riser 2, and (b) the amplification ratio between rising and falling sets with the amplification ratios on a log scale. The scatterplots show the log scale riser to faller amplification ratio as functions of (c) the noise power metric (color-coded by the value of f_{set}) and (d) the riser amplification metric.

For small amplitude injected waves, the solution to the Vlasov-Maxwell system according to linear theory predicts exponential wave growth if the electron distribution is sufficiently anisotropic [Kennel and Petschek, 1966]. Although the linear growth rate is a function of frequency, linear growth of rising and falling frequency ramps sweeping over the same frequency range will result in the same net integrated amplification, and thus variations in the linear growth rate with frequency cannot explain the preferential amplification of rising ramps observed in the data. However, after

undergoing linear growth, the wave amplitudes can become large enough to trap resonant electrons in the wave potential well, and the formation of this trap is believed to play a crucial role in nonlinear wave growth [Nunn, 1974; Dowden *et al.*, 1978; Vomvoridis and Denavit, 1979; Bell and Inan, 1981; Omura *et al.*, 1991]. The conditions for particle trapping can be summarized by a single collective inhomogeneity parameter, S , [Omura *et al.*, 1991] defined as:

$$S = \frac{1}{2\omega_t^2} \left[\left(3V_R - \frac{kv_\perp^2}{\omega_c} \right) \frac{\partial \omega_c}{\partial z} - \frac{2\omega + \omega_c}{\omega} \frac{d\omega}{dt} \right], \quad (4.1)$$

with the quantities ω_c , ω , and k representing the electron gyrofrequency, wave frequency and wavenumber, respectively. V_R is the resonance velocity and v_\perp is the component of the particle velocity perpendicular to the geomagnetic field, which is oriented in the z direction. The quantity ω_t is the trapping frequency, defined as:

$$\omega_t = \left(\frac{qv_\perp k B_w}{m_e} \right)^{\frac{1}{2}}, \quad (4.2)$$

where B_w is the wave magnetic field, q is the magnitude of the electron charge and m_e is the electron mass.

When S has a magnitude less than 1, particle trapping and consequently nonlinear wave growth can occur. As shown in Equation 4.1, S depends on the inhomogeneity of the geomagnetic field ($\frac{\partial \omega_c}{\partial z}$) as well as on the frequency sweep rate of the wave ($\frac{d\omega}{dt}$). For simplicity, we first consider the hypothetical case of a constant amplitude wave. The center of the interaction region is defined at $S = 0$, and the extent of the interaction region is defined where $|S| < 1$. For a monochromatic wave, $\|S(z)\|$ is symmetric around the equator, and thus the nonlinear interaction region is also symmetric around the equator. For a rising frequency ramp, $\frac{\partial \omega}{\partial t}$ is a positive constant, and $S(z)$ thus resembles the monochromatic profile except that it is shifted upstream, to latitudes toward the transmitter. Likewise, the reverse scenario holds true for a falling frequency ramp, and the nonlinear interaction region shifts downstream, towards the receiver. For the case of a constant amplitude wave, the spatial shift in the interaction region is approximately symmetric around the equator for rising

and falling tones. The inclusion of wave amplification adds to the complexity as ω_t depends on the wave amplitude and the wave amplitude will be growing as a function of position along the magnetic field line, which then changes the value of S ; this is an important aspect that contributes to the difference in amplification of rising compared to falling ramps.

4.2.1 Numerical Model

Modeling nonlinear amplification of coherent waves is analytically intractable and must be approached using numerical techniques. The Vlasov equation in canonical coordinates is shown in Equation 4.3, where the terms $\frac{dx_i}{dt}$ are governed by the single particle equations of motion, the Lorentz force.

$$\frac{\partial f}{\partial t} + \sum_{i=1}^n \frac{dx_i}{dt} \frac{\partial f}{\partial x_i} = 0 \quad (4.3)$$

In this study, we simulate the amplification of rising and falling frequency ramps using a recently developed narrowband Vlasov solver [Harid *et al.*, 2014a]. The solver discretizes the Vlasov equation on a uniform phase-space grid and then integrates in time using a first order finite difference linear upwind scheme. The model is well suited for simulating the growth of coherent waves in the large amplitude regime where particle phase trapping dominates.

Since the waves in this simulation are coherent, the Vlasov equation can be coupled to the narrowband wave equations, shown in Equations 4.4 and 4.5, which also account for the background cold plasma [Nunn, 1974].

$$\frac{\partial B_w}{\partial t} - v_g \frac{\partial B_w}{\partial z} = -\frac{\mu_0 v_g}{2} J_E \quad (4.4)$$

$$\frac{\partial \phi_w}{\partial t} - v_g \frac{\partial \phi_w}{\partial z} = -\frac{\mu_0 v_g}{2} \frac{J_B}{B_w} \quad (4.5)$$

The quantities B_w and ϕ_w are the wave amplitude and phase of the modulating wave packet propagating in the $-z$ direction at the group velocity, v_g . J_E and J_B are components of the resonant current in the direction of the wave electric and magnetic

fields respectively. The narrowband wave equations are integrated in time with the same finite difference scheme used for the Vlasov equation.

To simulate the Siple transmissions, we use a centered dipole geomagnetic field model at $L = 4$ and a cold plasma density of 250 cm^{-3} . The hot plasma distribution function is a bi-Maxwellian with a temperature anisotropy ($A = (\frac{T_{\perp}}{T_{\parallel}}) - 1$) of 1.16 and a hot electron density (n_h) of 0.25 cm^{-3} . The simulation domain extends out $\pm 5000 \text{ km}$ around the equator, chosen based on the minimum trapping amplitude threshold parameterized by S and for consistency with past work [Nunn, 1974; Gibby *et al.*, 2008]. Pulses that rise or fall in frequency are injected into the simulation space by enforcing a chirped phase at the input with an initial amplitude of 0.1 pT. The input pulses are 0.5 seconds in duration, and the rising and falling ramps have equal though opposite sweep rates, cover the same 500 Hz range of frequencies, and have the same center frequency. The instantaneous frequency profile for the rising ramps is given by $f_{rise}(t) = (f_{set} - 250) + 1000t$ and for the falling ramps by $f_{fall}(t) = (f_{set} + 250) - 1000t$, where f_{set} is the center frequency of the ramp. The linear growth spectrum for the simulation parameters is shown in Figure 4.3(a), and a family of linear growth rate curves for varying anisotropies is shown in Figure 4.3(b). In Figure 4.3(a), the frequency at which the linear growth rate is maximized (f_m) is 2450 Hz, and the center frequencies for the simulation are chosen such that two frequencies are below f_m (1000 Hz, 1500 Hz), and the other two are above f_m (3480 Hz, and 4500 Hz). Linear growth alone cannot explain the difference between rising and falling ramps; however, all signals first undergo linear growth before crossing the nonlinear threshold. Therefore, rising ramps with a center frequency above the maximum linear growth rate frequency will at first grow faster than falling ramps as the starting frequency is closer to f_m and subsequently reach the nonlinear threshold sooner. We thus expect rising ramps to amplify more in these cases and falling ramps to amplify more in the cases where the center frequency is below the maximum linear growth rate frequency.

The received wave amplitudes for the fully nonlinear simulations are shown in Figures 4.3(c-f), plotted as a function of time at the output of the simulation space

($z = 5000km$). For the two cases where the center frequency is below f_m , Figures 4.3(c,d), the falling ramps grow more than the rising ramps. The corresponding amplification ratios (riser to faller) are 0.554 and 0.556 for the 1000 Hz and 1500 Hz cases respectively. Figures 4.3(e,f), with center frequencies of 3480 Hz and 4500 Hz, correspond to the cases where the rising ramp grows faster at first due to the higher initial linear growth rate and thus reaches the trapping threshold sooner. The corresponding amplification ratios are 2.27 for $f_{\text{set}} = 3480$ Hz and 4181 for $f_{\text{set}} = 4500$ Hz. In fact, for the 4500 Hz case, Figure 4.3(f), the falling ramp does not reach the trapping threshold and does not undergo any nonlinear growth and subsequently gives a far lower output amplitude than the rising ramp and thus a very large amplification ratio, matching well with the infinity ratio cases.

The fact that Siple observations generally show a higher degree of growth for rising ramps suggests that the transmitted signals are more likely to be above f_m . Further, as seen in Figure 4.3(b), when the electron temperature anisotropy decreases, the value of f_m decreases. Thus, lower anisotropies will favor the growth of risers, as more of the spectrum is above f_m . This is consistent with the observational finding in Figure 4.2(c) showing that lower noise power (which is associated with less natural emissions and presumably a lower linear growth rate) favors higher amplification ratios (better amplification of risers). As A decreases, risers are favored, but the total growth of signals is expected to be lower, and this trend is seen in Figure 4.2(d) where higher amplification of risers over fallers is associated with lower total power in the risers.

Spatial amplitude profiles from the simulation shown in Figure 4.3(e) with $f_{\text{set}} = 3480$ Hz are shown at two different time steps in the simulation in Figure 4.3(g) and (h), with an animation of all of the full simulations in the supplementary materials. The dashed curve represents the minimum amplitude for particle trapping for a monochromatic tone at f_{set} . At $t = 0.44s$ in Figure 4.3(g), in the region upstream of the equator ($z < 0$), the waves are below the minimum trapping amplitude and grow according to linear theory. The linear growth rate, which is a function of the wave frequency, is initially higher for the rising tone as it starts at a lower frequency. This

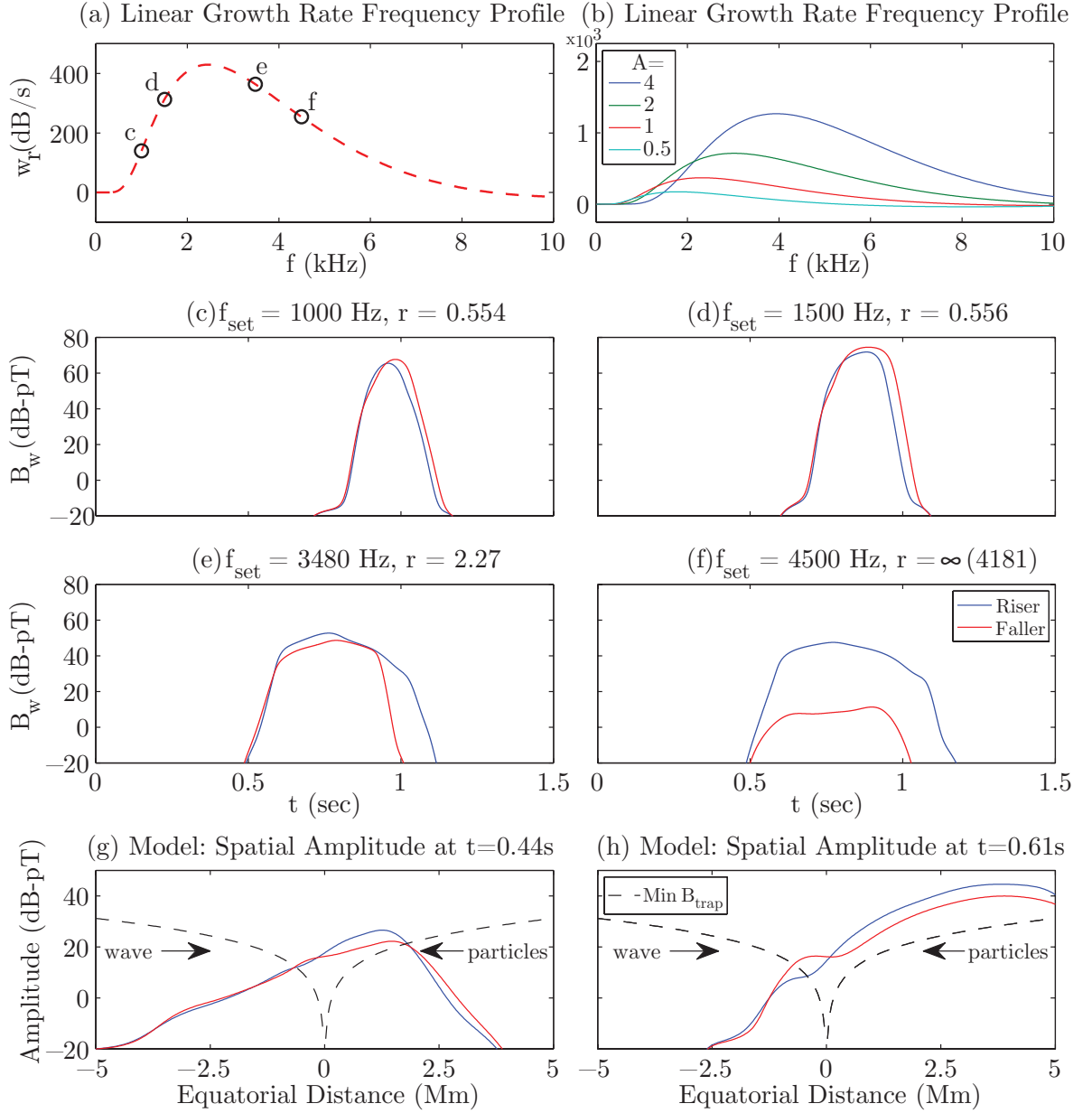


Figure 4.3: (a) The linear growth rate curve as a function of wave frequency for $A = 1.16$ and $n_h = 0.25\text{cm}^{-3}$ with four points indicating the center frequency for the simulation in the corresponding panel, and (b) as a family of such curves for a range of anisotropies. The time series plots show the simulated amplitude at the end of the interaction region ($z=5000$ km) for (c) $f_{\text{set}} = 1000$ Hz, (d) $f_{\text{set}} = 1500$ Hz, (e) $f_{\text{set}} = 3480$ Hz, (f) $f_{\text{set}} = 4500$ Hz for risers (blue) and fallers (red). Additionally, the spatial amplitude profile over the interaction region is shown at (g) $t = 0.44s$ and at (h) $t = 0.61s$ for risers (blue) and fallers (red, with the minimum trapping amplitude for a monochromatic wave with 70 deg pitch angle (black)).

difference in initial linear growth rates ensures that the rising tone crosses the minimum trapping amplitude sooner than the falling tone and consequently undergoes nonlinear growth sooner as well.

At a later time ($t = 0.61s$), shown in Figure 4.3(h), the waves have propagated further through the simulation space. The wave amplitude of the falling ramp is still lower than the rising ramp; however, the falling ramp has grown in time such that the wave crosses the minimum trapping amplitude. This occurs due to the increase in linear growth rate resulting from the decrease in the falling ramp frequency and partially from the accompanying shift of the nonlinear interaction region downstream. Conversely, the rising ramp begins to damp slightly near ($z = 0$) because the linear growth rate has decreased due to the increased frequency; however, since the riser crossed the trapping threshold earlier in time, the change in the linear growth rate does not play as much of a role. The net effect is that the rising ramp undergoes more amplification than the falling frequency ramp.

4.3 Conclusions

Historical observations of Siple Station transmissions [*Mielke and Helliwell, 1993; Carlson et al., 1985a*], along with more recent cases from HAARP wave injection experiments [*Golkowski et al., 2008, 2011*] and satellite recordings of discrete chorus elements [*Burtis and Helliwell, 1976; Li et al., 2011*], indicate a natural preference for the amplification of rising frequency signals over falling frequency signals. Furthermore, the importance of the time and location of the transition from linear to nonlinear growth was postulated from wave injection observations made by *Golkowski et al. [2010]*.

Here, for the first time, we quantify the amplification of rising and falling frequency ramps injected into the magnetosphere from Siple Station, and use a narrowband Vlasov-Maxwell simulation to interpret the results. Simulations show that the net amplification of frequency ramps depends on both the linear growth rate and the duration of nonlinear growth. When the center frequency of the ramp is above f_m , the frequency at which the linear growth rate is maximized, rising frequency

ramps will undergo more initial linear growth. Conversely, falling frequency ramps will undergo more initial growth when the center frequency is below f_m . Further, for rising frequency ramps the nonlinear interaction region is shifted upstream (to latitudes below the equator for a southern hemisphere transmitter), and thus the rising ramps can undergo nonlinear growth earlier and for a longer duration owing to the feedback effect of wave amplitude on the conditions for nonlinear growth (such as expressed in the S -parameter). These effects combine to result in a net preferential amplification of rising frequency ramps. In the Siple receptions, we find that rising frequency ramps generate a total power that is on average 1.9 times higher than that of falling frequency ramps when both are received within a given transmission. Also, in 17% of receptions, only the rising frequency ramps are observed, and the falling ramps are below the detectable signal level. This behavior may occur when the falling ramps do not reach the threshold for nonlinear growth such as when the ramp center frequency is well above f_m as in Figure 4.3(f). A lower value of hot electron temperature anisotropy will move f_m to lower frequency, further favoring the growth of rising ramps. This is supported experimentally by the inverse correlation between the amplification ratio and both the observed noise power and the total signal power metric. Finally, in 20% of the receptions, falling ramps are amplified more than rising ramps, and simulations show that this may occur when the ramp center frequency is below f_m . Our results contribute to the understanding of magnetospheric wave amplification and the described mechanism likely also plays a role in chorus emissions, which likewise exhibit a preference for structured rising as opposed to falling emissions.

Chapter 5

Observational Behavior of Triggered Emissions

Nonlinear wave-particle interactions result in the exponential temporal amplification of coherent signals injected into the magnetosphere, as discussed in Chapter 3 and Chapter 4. A second result of these interactions is the generation of new frequency components called triggered emissions. Triggered emissions are important for understanding naturally occurring waves in the magnetosphere such as chorus emissions, which show similar frequency time structure but have thus far been difficult to interpret or model. The present work aims to provide a better understanding of the observed structure of triggered emissions to inform further work and is in review as *Li et al.* [2015b].

In this work, we analyze a database of receptions of a mini-diagnostic (MDIAG) format transmitted by Siple in 1986, which included long and short fixed frequency tones, falling frequency ramps, and a pair of tones closely spaced in frequency, under a variety of times and conditions in order to build a statistical understanding of the time-frequency behavior of triggered emissions (TEs). We also apply the same analysis process to study triggering from the staircase coherence (STACO) format, which includes rising and falling frequency ramps, to further extend our analysis of the effect of the triggering signal on triggered emissions. Past experimental work solely focused on triggering from fixed frequency tones, but here, by considering observations

of triggered emissions based on the different triggering elements, we show that the triggering element has a significant effect on the resulting triggered emission. By quantifying the overall frequency change, we then show that the physical process governing the free-running behavior of triggered emissions is effectively independent of the triggering signal once the triggered emission begins. These statistical bounds on the properties of the behavior of triggered emissions are important for evaluating our theoretical understanding of the triggered emission generation mechanism and the validity of numerical simulations.

5.1 Past Observations and Modeling Efforts

To frame this statistical understanding of triggered emission behavior and to provide some background to understanding triggered emissions, we include a brief review of related past research. Similarly, in order to interpret the experimental results, we have also included a short review of the three common numerical models used to simulate triggered emissions and provide theoretical interpretation.

The generation of free running emissions is a key feature of the coherent wave instability. Triggered emissions typically occur after the transmitted signal undergoes a period of exponential temporal growth and generally take the form of narrowband rising, falling or various hook-like elements. These basic forms are commonly referred to as risers, fallers, and hooks [[Helliwell and Carpenter, 1962](#); [Helliwell, 1965](#)]. The earliest work observed the generation of these triggered emissions from Morse code VLF Navy transmissions [[Helliwell et al., 1964](#); [Helliwell, 1965](#); [Kimura, 1968](#); [Lasch, 1969](#)] or from natural signals such as whistlers [[Carpenter et al., 1969](#)], while later work focused on observations of triggered emissions from Siple transmissions [[Helliwell and Katsufakis, 1974](#); [Stiles and Helliwell, 1977](#); [Helliwell, 1988b,a](#); [Sa, 1990](#)]. Repeated observations of triggered emission behavior provided phenomenological descriptions of conditions for triggering. [Stiles and Helliwell \[1975\]](#) found that triggering occurs only after the transmitted pulses undergoes its exponential growth and saturates, and [Helliwell \[1988b\]](#) observed that triggering usually generates risers and can occur repeatedly until the transmitted pulse ends. The falling triggered emissions, so-called

fallers, were observed to occur when the signal terminates near the saturation level and when the transmitted pulses were short in duration, <200 ms [Lasch, 1969; Helliwell and Katsufrakis, 1974]. The saturation level is the amplitude at which the nonlinear amplification of the injected frequency signal terminates and after which other nonlinear effects, such as triggered emissions, may occur [Gibby *et al.*, 2008]. Rising and falling triggered emissions, and the times at which the triggering begins, were also found to relate to phase advances in the transmitted pulse [Paschal, 1988, Chapter 4].

Numerical modeling of triggered emissions has proven to be an incredibly challenging task, in spite of work by several research groups over many decades. While various numerical approaches have provided insight into the triggering process and behavior, modeling attempts have not successfully reproduced the entire range of triggered emission behavior. Both hybrid- [Katoh and Omura, 2006] and full- [Hikishima *et al.*, 2010] particle-in-cell (PIC) codes successfully simulated rising tone triggered emissions, and the results suggest that triggering occurs at the back end of the input signal near the magnetic equator and that the resonant current formation by untrapped electrons plays an important role in the triggering process. Using the Vlasov Hybrid Simulation (VHS) code, Nunn *et al.* [2005] performed a parametric study and found that low input amplitudes generate fallers, intermediate input amplitudes generate risers, and large input amplitudes generate fallers or hooks. The frequency sweep rate of the resulting triggered emission was shown to be most dependent on the cold plasma density, where lower densities resulted in higher sweep rates. Phenomenological approaches [Helliwell, 1967; Trakhtengerts *et al.*, 2003] have proven to be very general in generating any desired form of triggered emission, with the spectral form of the triggered emission primarily dependent on the position and motion of the location (i.e., the locus) of the interaction region. However, it is otherwise difficult to ascertain the validity of these approaches due to the large number of free parameters.

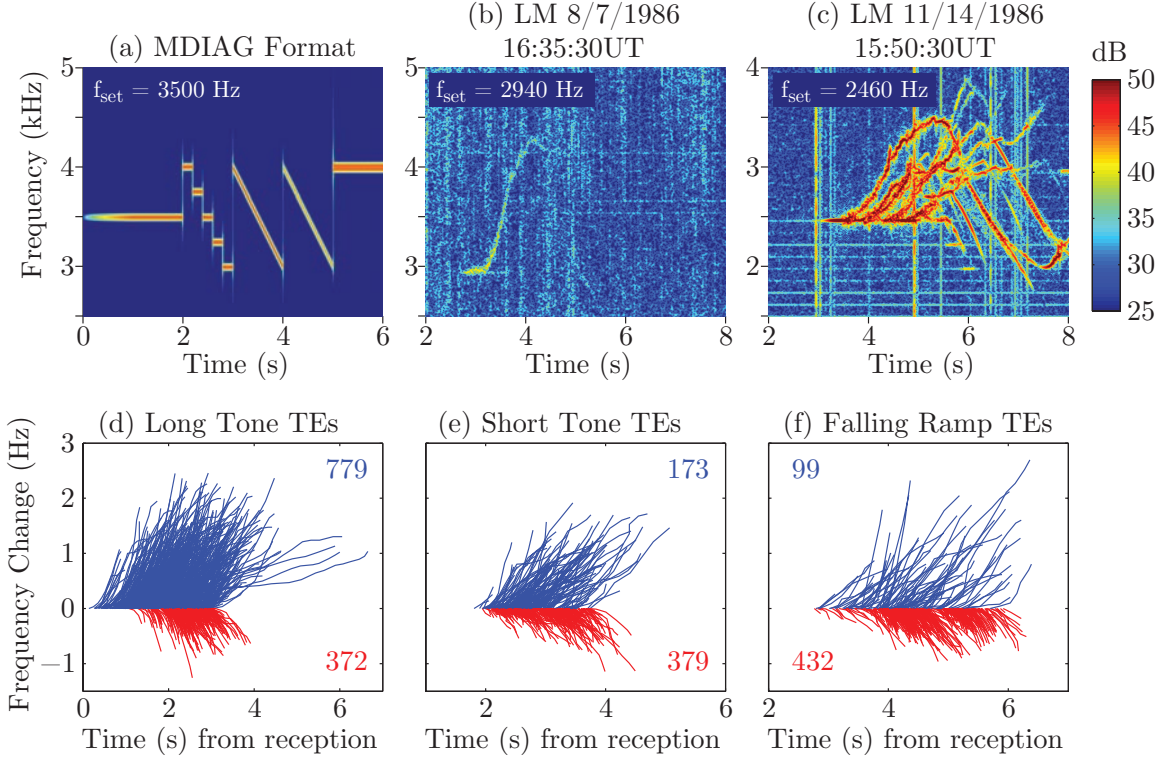


Figure 5.1: Spectrograms of (a) the transmitted MDIAG format and two conjugate hemisphere receptions with (b) a canonical simple riser and (c) a wide variety of triggered emissions. All collected triggered emissions are overlaid on the same plot to show the frequency and time profiles of risers (blue) and fallers (red) triggered from the transmitted (d) long tone, (e) short tones and (f) falling ramps. The vertical axis describes the triggered emission’s frequency change relative to its initial triggering frequency, and the horizontal axis describes the triggered emission’s initiation time relative to the time at which the transmitted signal was received. The triggered emissions from the doublets are not included in the spectrogram or as an overlay plot due to an insufficient number of observations. For clarity in displaying the overlay plots, the triggered hook emissions are not included as they would overlap with and obscure the risers and fallers, and the color-coded numbers in (d-f) describe the number of plotted risers (blue) and fallers (red) for each triggering element.

5.2 The 1986 MDIAG and STACO Data Set

We characterize triggered emission behavior by examining two transmission formats and their associated triggered emissions that were received at the Lake Mistissini

receiver during 1986. The first format is the mini-diagnostic format, abbreviated MDIAG, which was first discussed in Section 3.1 and described here again for reference. The MDIAG format was commonly transmitted by Siple Station in 1986 and is shown in spectrogram format in Figure 5.1(a). The entire transmission is centered on an operator-selected tuning frequency, f_{set} , which ranged from 1680 Hz to 5100 Hz. The format is composed of a 2-s “long” tone at f_{set} , five 200-ms “short” tones, two 1-s -1 kHz/s “falling ramps” centered at f_{set} , and a 7-s dual frequency tone, “doublet”, spaced 30 Hz apart and centered on $f_{\text{set}} + 495$ Hz. The long tone begins with a power ramp, where the transmitted power is increased from -10 dB to 0 dB over the first second. The short tones descend in a staircase from $+500$ Hz to -500 Hz from f_{set} in 250 Hz steps. The second of the two frequency ramps is transmitted at -6 dB below the power of the first ramp. Data from the conjugate receiving station in Lake Mistissini, Canada, is available for 1143 transmissions of the MDIAG format, and 444 receptions were detected for a 39% reception rate. The format was originally used for assessing reception conditions to determine if other studies could be conducted, and similar diagnostic transmission formats were used throughout the years of operation of Siple Station.

Two case examples of MDIAG receptions are shown in Figures 5.1(b-c), and highlight the wide range of triggered emission behavior. Figure 5.1(b) illustrates a canonical riser, which initiates from the long tone and then rises in frequency at a relatively constant frequency sweep rate. In contrast, Figure 5.1(c) demonstrates the more common behavior, where a number of triggered emissions are triggered by the injected signal. Here, we see that not only are risers excited, but fallers and hooks (triggered emissions that change from a riser to a faller or vice versa) are also generated. To develop our data set of 3469 triggered emissions excited from our 444 MDIAG transmissions, we first processed each transmission to generate a high time and frequency resolution spectrogram. Using the spectrogram, we considered narrower time and frequency windows around each type of triggering element (long tone, short tones, ramps, and doublet) and manually identified and selected time and frequency points corresponding to each triggered emission. Each triggered emission was then labeled

based on its frequency behavior, where signals that only increased or decreased in frequency were labeled as risers or fallers and signals that both increased and decreased in frequency were labeled as hooks. The results are compiled in Table 5.1. Hooks are also further subdivided into positive hooks, hooks that initially rise in frequency, and negative hooks, hooks that initially fall in frequency. The upper half of Table 5.1 categorizes the number and percentage of triggered emissions triggered by each transmission element (long tone, short tones, falling ramps, and doublet) of the MDIAG format.

To characterize an aggregate profile of all 3469 triggered emissions, overlay plots in Figures 5.1(d-f) plot the aggregate time-frequency profile of risers (blue) and fallers (red) differentiated by the triggering element. For clarity, the triggered hook emissions are not shown on these plot due to their overlap with other triggered emissions. The vertical axis describes the frequency change of the triggered emissions relative to their initial initiation frequency, while the horizontal axis describes when the triggered emissions began relative to when the triggering MDIAG transmission was received. The triggering transmission element plays a significant role in the determining the resulting type of triggered emission, but in general, risers initiate earlier than fallers and extend to higher frequencies and endure for longer durations. The doublet transmission element exhibits a suppression effect [Helliwell *et al.*, 1986] that suppresses the amplification of the doublet signals and disturbs the conditions conducive for generating triggered emissions. As such, the triggered emissions triggered from doublets, numbering 109 triggered emissions, are not shown or further considered here due to the statistically insufficient number of cases.

As the MDIAG format only includes falling frequency ramps, we also examine the behavior of triggered emissions from a second transmission format called the staircase coherence format, abbreviated STACO, which includes both rising and falling frequency ramps. The STACO format, first discussed in Section 4.1 and described again here for reference, was transmitted by Siple from July to December of 1986 and is illustrated in Figure 5.2(a). This format is composed of two identical sets of rising, 1 kHz/s ramp elements (Riser 1 and Riser 2), followed by two identical sets of falling, -1 kHz/s ramp elements (Faller 1 and Faller 2). Each ramp set contains

five 1-s elements approximating an ideal frequency ramp composed of 1 ms, 10 ms, 25 ms, 50 ms, and 100 ms long tones. The entire transmission is centered on an operator selected tuning frequency, f_{set} , which ranged from 1680 Hz to 4020 Hz. Data from the conjugate receiving station is available for 170 transmissions of the STACO format, and 63 receptions were detected for a 37% reception rate, although one case is excluded from further analysis due an operator transmission error. The format was originally intended for studying the required time-frequency spacing to approximate a continuous frequency ramp [Mielke and Helliwell, 1993], and has also been recently used to quantify the observed preferential nonlinear amplification of rising ramps over falling ramps [Li et al., 2015a].

An example of a STACO reception is shown in Figure 5.2(b), with the white lines at 3980 Hz and 2980 Hz marking the frequency extent of the transmitted signals in order to highlight the triggered emissions rising and falling at the end of the ramp elements. To characterize an aggregate profile of the 1183 triggered emissions excited from our set of 62 complete STACO transmissions, overlay plots in Figures 5.2(c-d) plot the aggregate time-frequency profile of all risers (blue) and fallers (red) separated by the triggering element. For clarity, the hooks are not shown due to their overlap with other triggered emissions. The vertical axis describes the frequency change of the triggered emissions relative to their initial initiation frequency, while the horizontal axis describes when the triggered emissions began relative to the reception of a frequency ramp in the STACO transmission. These overlay plots once again highlight the significant role of the triggering transmission element in determining the resulting type of triggered emission, where rising ramps tend to generate rising triggered emissions and falling ramps generate falling triggered emissions. It can also be seen that risers extend to higher frequencies and endure for longer durations than fallers. As before, the triggered emissions are again labeled as risers, fallers, or hooks and are categorized in the STACO half of Table 5.1 by the number and percentage of triggered emissions triggered by each transmission element (rising ramps and falling ramps).

		Risers	Fallers	Hooks	Positive	Negative
MDIAG	All	1111	1220	1138	759	379
	Long Tone	779	372	585	505	80
	Short Tones	173	379	227	124	103
	Falling Ramps	99	432	246	65	181
	Doublet	43	15	51	44	7
STACO	All	474	225	484	409	75
	Rising Ramps	458	27	405	404	1
	Falling Ramps	14	198	79	5	74

		Risers	Fallers	Hooks	Positive	Negative
MDIAG	All	32%	35%	33%	22%	11%
	Long Tone	45%	21%	34%	29%	4.6%
	Short Tones	22%	49%	29%	16%	13%
	Falling Ramps	13%	56%	32%	8.4%	23%
	Doublet	39%	14%	47%	40%	6.4%
STACO	All	40%	19%	41%	35%	6.3%
	Rising Ramps	51%	3.0%	46%	45%	0.1%
	Falling Ramps	4.8%	68%	27%	1.7%	25%

Table 5.1: Table of MDIAG and STACO Triggered Emission Statistics in 1986, illustrating the overall number of triggered emissions, divided into risers, fallers, and hooks, with hooks further subdivided into positive (initially rising) and negative (initially falling) hooks. The two versions provide the counts and percentages of each type of triggered emission excited by a given transmission element. The percentages for risers, fallers, and hooks sum to 100%, while the positive and negative hook percentages sum to the percentage of hooks. The top half of each table describes the results for the MDIAG format with further subdivisions by the long tone, short tones, falling ramps, and doublet elements, while the lower half of each table describes the results for the STACO format with subdivisions for the rising and falling ramps.

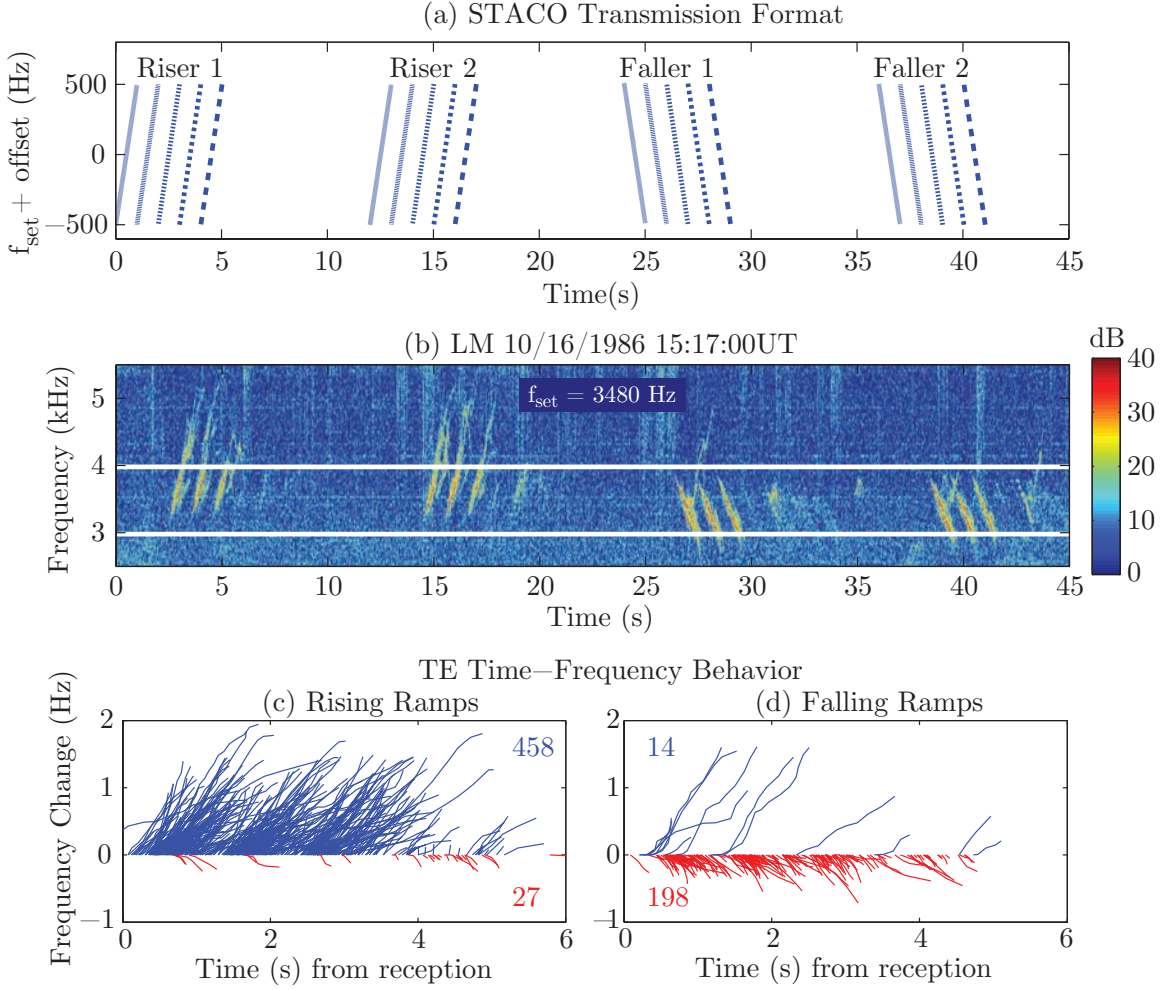


Figure 5.2: Spectrograms of (a) the transmitted STACO format, and (b) an example of the received signal including triggered emissions on various elements. All collected STACO triggered emissions are overlaid on the same plot to show the frequency and time profile of risers (blue) and fallers (red) triggered by (c) rising ramps and (d) falling ramps. The vertical axis describes the triggered emission's frequency change relative to its initial triggering frequency, and the horizontal axis describes the triggered emission's initiation time relative to the time at which the transmitted signal was received. For clarity in displaying the overlay plots, the triggered hook emissions are not included as they would overlap with and obscure the risers and fallers, and the color-coded numbers in (d-f) describe the number of plotted risers (blue) and fallers (red) for each triggering element.

5.3 Statistical Characterization of Triggered Emissions

As triggered emissions can take on complex forms and can overlap significantly in time and frequency with one another, we were unable to use an automated approach to detect triggered emissions. Instead, we visually inspected a high-resolution spectrogram of each transmission and manually identified the triggered emissions. The initiation time of each triggered emission and the specified transmission element times in the transmission format were used to identify which transmission element was the triggering element. We selected a number of features to quantify triggered emission behavior and primarily analyzed the net frequency change (frequency change) and the initial frequency sweep rate (sweep rate). The frequency change is computed as the ending frequency minus the starting frequency. The initial sweep rate is calculated as the slope between the first two manually selected time-frequency points of the triggered emission and characterizes the instantaneous frequency sweep rate of the triggered emission at the moment of initiation. This is based on the assumption that the initial sweep rate most closely describes the initiation process and that the later behavior is driven by its own, independent interactions with the energetic electrons. Other parameters that we consider include the initial frequency at which the triggered emission began, the operator selected f_{set} transmission frequency, the frequency at which the triggered emission ended, and the maximum frequency that the triggered emission reached.

An overview of aggregate triggered emission behavior is shown in Figure 5.3. Here, we divide the plots of triggered emissions from the MDIAG format into the standard classes of risers, fallers, and hooks. Each 2D histogram shows the occurrence of triggered emissions and their evolution in time and frequency relative to their triggering initiation time and frequency. The stacked histogram of risers and fallers in Figure 5.3(a) illustrates their differing extent of frequency change and time duration, and a comparison with the hooks in Figure 5.3(b) on their right demonstrate how hooks could be considered as combinations of risers and fallers. The color reflects the density in occurrence of triggered emissions in a given time and frequency bin

and the high density regions indicate a narrow cone of behavior for risers and fallers that can be used to define the prototypical riser and faller. This high-density cone also indicates that many triggered emissions last only a short duration, <0.5 s, and undergo only small amounts of frequency change, ~ 200 Hz, and that the fallers fall at a slightly higher sweep rate than risers rise. Overall, the risers last for a longer duration and extend to significantly higher frequencies than fallers, about twice as much in both respects. The hooks fill in the empty region between risers and fallers, and also exhibit behavior similar to combinations of the risers and fallers.

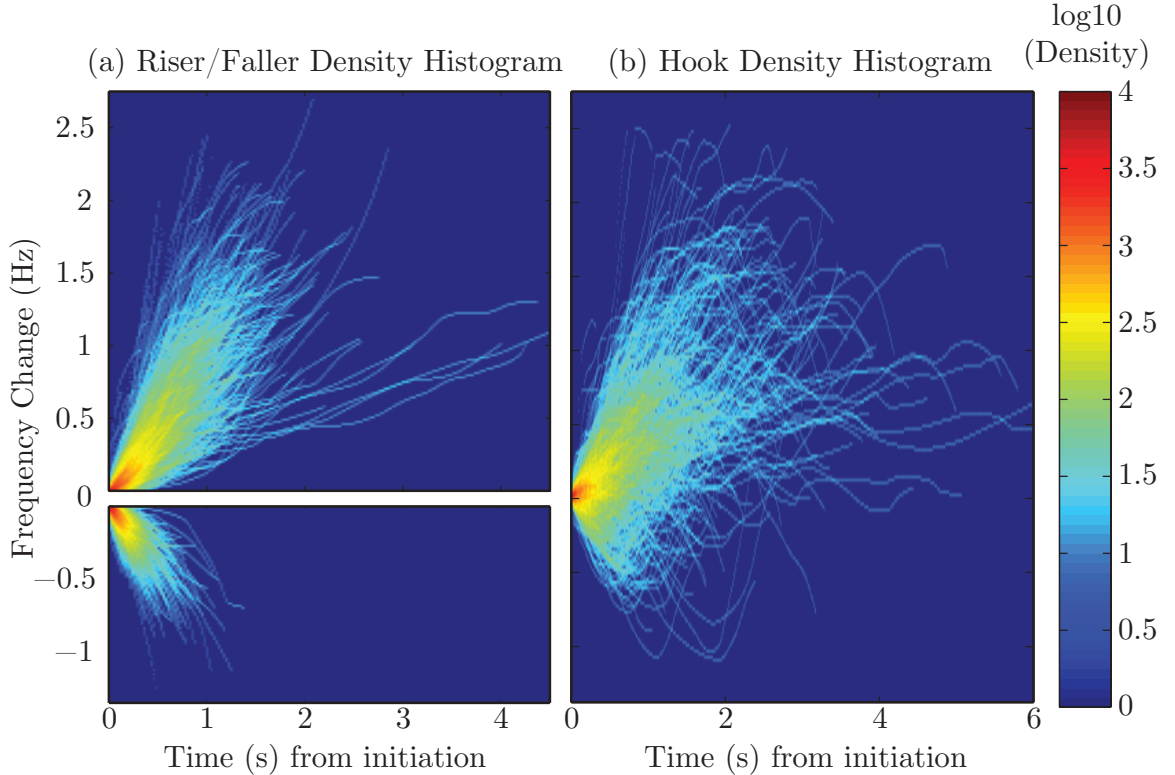


Figure 5.3: A two dimensional histogram showing the density in occurrence of triggered emissions from the MDIAG format with a given time and frequency change from the triggering initiation time and frequency for (a) risers (top) and fallers (bottom), and (c) hooks. The color axis describes the number of triggered emissions in log scale.

We now consider the statistical characteristics of triggered emission behavior, as shown in Figure 5.4 and Figure 5.5. Figures 5.4(a-c) (top row) show histograms of the

net frequency change for triggered emissions triggered by the (a) long tone, (b) short tones, and (c) falling ramps. Figures 5.4(d-f) (bottom row) show histograms of the initial sweep rate for triggered emissions from the (d) long tone, (e) short tones, and (f) falling ramps. Figures 5.5(a-c) (top row) show scatterplots showing sweep rate versus frequency change for triggered emissions from the (a) long tone, (b) short tones, and (c) falling ramps. And Figures 5.5(d-f) (bottom row) show scatterplots of frequency change versus initial frequency for triggered emissions from the (d) long tone, (e) short tones, and (f) falling ramps. All blue plot elements represent risers, while red elements represent fallers. In Figures 5.5(a-c), the green elements in quadrants II and IV represent hooks, where the initial sweep rate may not reflect the overall net frequency change. Each row is divided into the three main MDIAG format elements, long tone, short tones, and falling ramps, as the overlay plots in Figure 5.1 indicate a significant dependence on the triggering element. The text in the Figures 5.4(a-f) details the number of net risers (blue) and net fallers (red) observed; these numbers cover all triggered emissions with a net positive or negative frequency change.

In general, from Figures 5.4(a-c), the net frequency extent ranges from -1 kHz to 2.5 kHz, with risers undergoing a larger change in frequency than fallers, a median change of 558 Hz compared with -198 Hz for fallers. More specifically, the long tone exhibits significantly more triggered emissions and a preference for exciting more risers than fallers. The set of five short tones and the falling ramps preferentially excite fallers, and the short tone triggered emissions tend to undergo smaller changes in frequency. From Figures 5.4(d-f), we see the preference at initiation for the long tone to excite more risers and for the short tone and the falling ramps to excite more fallers and that for all triggered emissions the initial frequency sweep rate ranges from -5 kHz/s to 5 kHz/s, although 97.8% of the cases are between -2.5 kHz/s and 2.5 kHz/s. We can also compare the sweep rate versus the net frequency change as shown in Figures 5.5(a-c). As before, the long tone appears to trigger more risers and the short tones and falling ramps trigger more fallers. Furthermore, this presentation of a scatterplot allows the examination of hooks as well, in green. The long tone generates more rising hooks, while the short tones and falling ramps produce more negative hooks. Another interesting result is that risers and fallers appear to exhibit

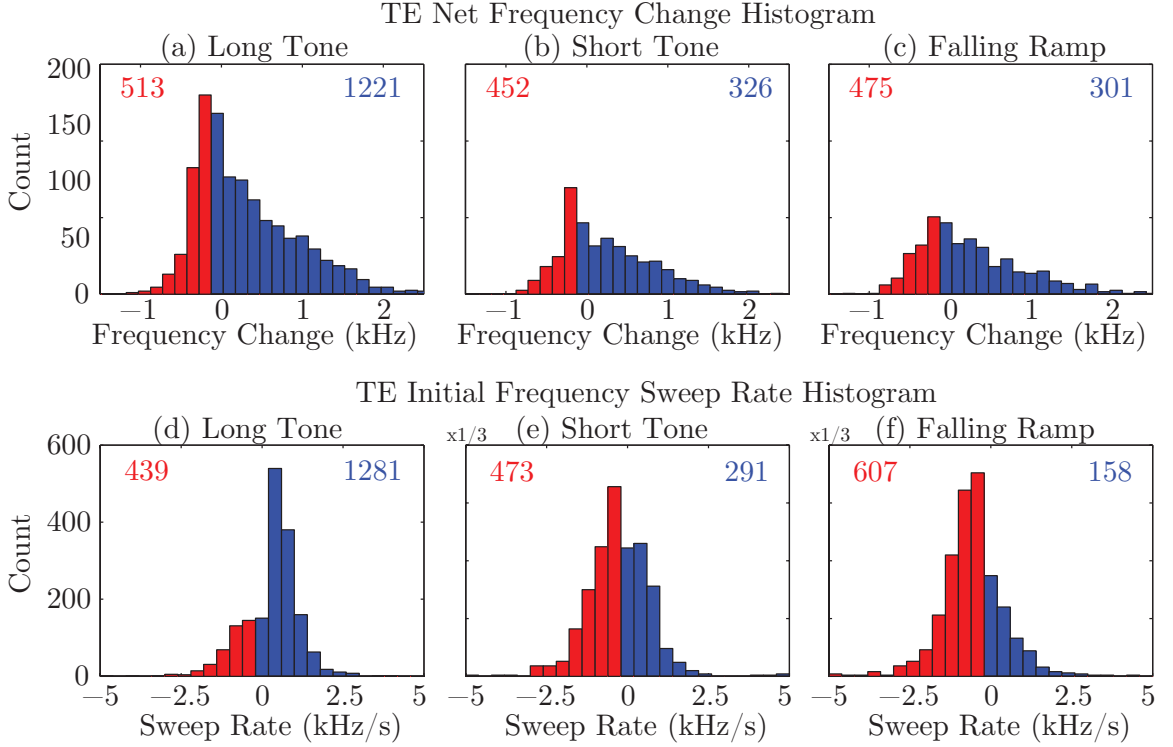


Figure 5.4: Analysis plots summarizing statistical observations and correlations of the time-frequency behavior of triggered emissions (TEs) excited from MDIAG transmissions. Histograms of net frequency change and initial frequency sweep rates of the triggered emissions are broken down by the triggering element type of (a,d) long tone, (b,e) short tones, and (c,f) falling ramps in the left, middle, and right columns respectively. Blue bars illustrate net risers, while red bars illustrate net fallers. (Net frequency change includes all triggering emission types that end with positive or negative frequency change, and net sweep rate includes all triggering types that begin with positive or negative sweep rates.) The numbers in each subplot describe the number of net risers (blue) and net fallers (red) observed.

different distributions, with fallers (red) in the lower left quadrant demonstrating a much smaller range in frequency change and sweep rate than the risers (blue) in the upper right quadrant.

While we compared a number of frequency parameters, between the initial frequency, the ending frequency, the maximum frequency, the transmission frequency, the frequency change, and the frequency sweep rate, we show just one comparison in Figures 5.5(d-f) between the frequency change and the initial frequency of triggered

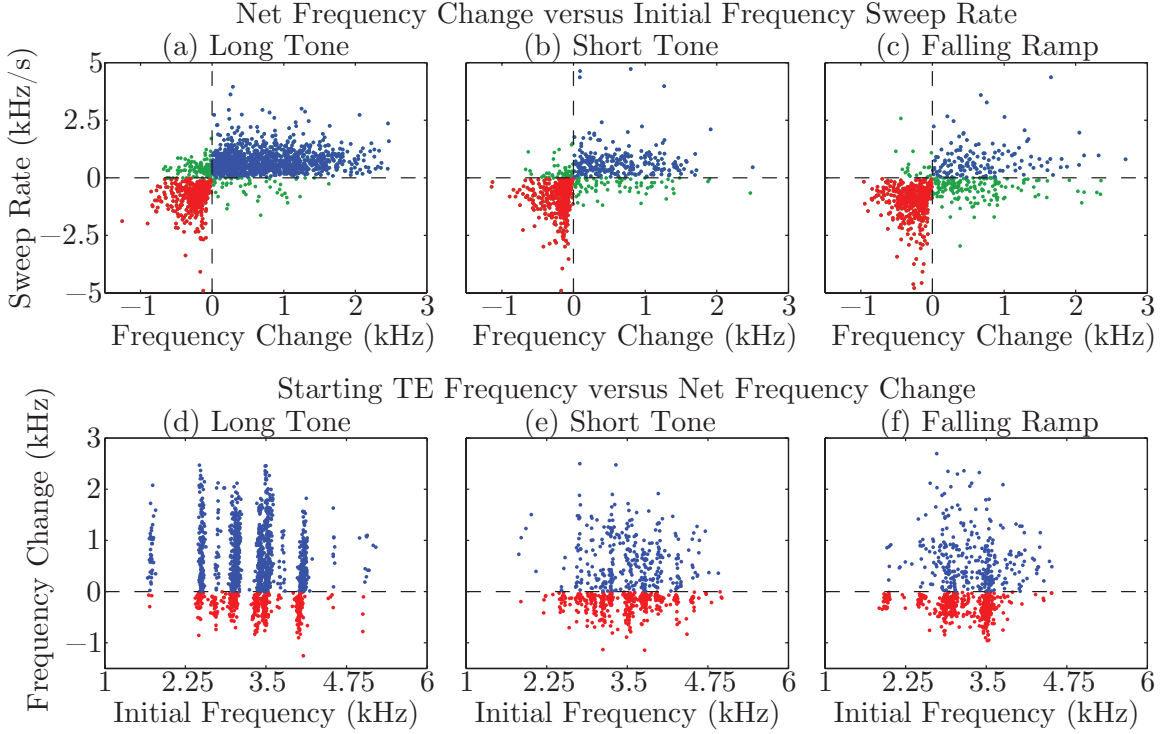


Figure 5.5: Additional summary plots of triggered emissions (TEs) excited from MDIAG transmissions. The scatterplots show the frequency sweep rate as a function of the net frequency change for the (g) long tone, (h) short tones, and (i) falling ramps. The dashed black lines show the zero sweep rate and zero frequency change boundaries with risers in blue, fallers in red, and hooks in green. Similarly, the scatterplots show the net frequency change as a function of the initial triggered emission frequency for triggered emissions from the (g) long tone, (h) short tones, and (i) falling ramps. And the dashed black line shows the zero frequency change boundary.

emissions. There appears to be a weak trend in Figure 5.5(d) where the extent in frequency change decreases as the initial frequency increases, but there is no definitive correlation due to fewer cases at the high and low initial frequencies. And to avoid any confusion, the apparent structure of the scatterplot in Figure 5.5(d) is due to the limited discrete transmission frequencies used, while the lack of such structure in (k) and (l) is due to the multiple offsets in frequency from f_{set} with the short tones and falling ramps in a transmission. Comparison of the frequency change with the f_{set} transmission frequency, the ending triggered emission frequency, and the triggered

emission maximum frequency also reveals no correlation. Similarly, the frequency change does not depend on the value of the Kp index.

In addition to considering the time-frequency behavior of individual triggered emissions, we are also interested in understanding the parameters that determine the total number of triggered emissions excited by a given transmission. We checked for a dependence of the total number of triggered emissions for an MDIAG transmission on the Kp at transmission in Figure 5.6(b), and also include a plot of the general Kp conditions under which detection occurs in Figure 5.6(a). Figure 5.6(a) illustrates the breakdown of the Kp index at transmission into five quantiles and the percent of transmissions received for each quantile. We note here that transmissions are usually detected more often when Kp is low, which is in good agreement with the quieting conditions of Kp for reception of Siple signals noted in *Li et al. [2014]*. The conditions of lower Kp are likely required in order for the formation of ducts for the propagation of ELF/VLF waves. Taking the received transmissions, we can then consider the number of triggered emissions based on the Kp conditions. Figure 5.6(b) breaks down transmissions by low (0-2), middle (3-12), and high (13+) number of triggered emissions and the Kp at transmission is again divided into five quantiles. The number separations were selected by examining at a histogram of the occurrence of given counts of triggered emissions. While there does not appear to be any strong correlation between the low and mid cases of triggered emissions with Kp, the high number cases have a weak trend suggesting that more disturbed geomagnetic conditions, as reflected by higher Kp, may result in a higher number of triggered emissions for a transmission.

Another parameter which may be important in determining the number of triggered emissions is the total amplification of the injected signal. The total growth can be measured by finding the narrowband signal amplitude of an injected transmission as in Figure 5.6(c) and subtracting the noise floor from the saturation threshold [*Li et al., 2014*]. We measure the total growth of the long tone element from our 444 MDIAG transmissions and compare the total growth with the number of triggered emissions excited by the long tone as shown in Figure 5.6(d). We observe that there is a weak linear correlation between the number of triggered emissions and the total

growth with $\rho = 0.56$ with a p-value < 0.01 . The correlation is less pronounced when only considering the total number of risers or fallers, and the total number of triggered emissions is taken to be more representative of the overall triggering activity for a given transmission.

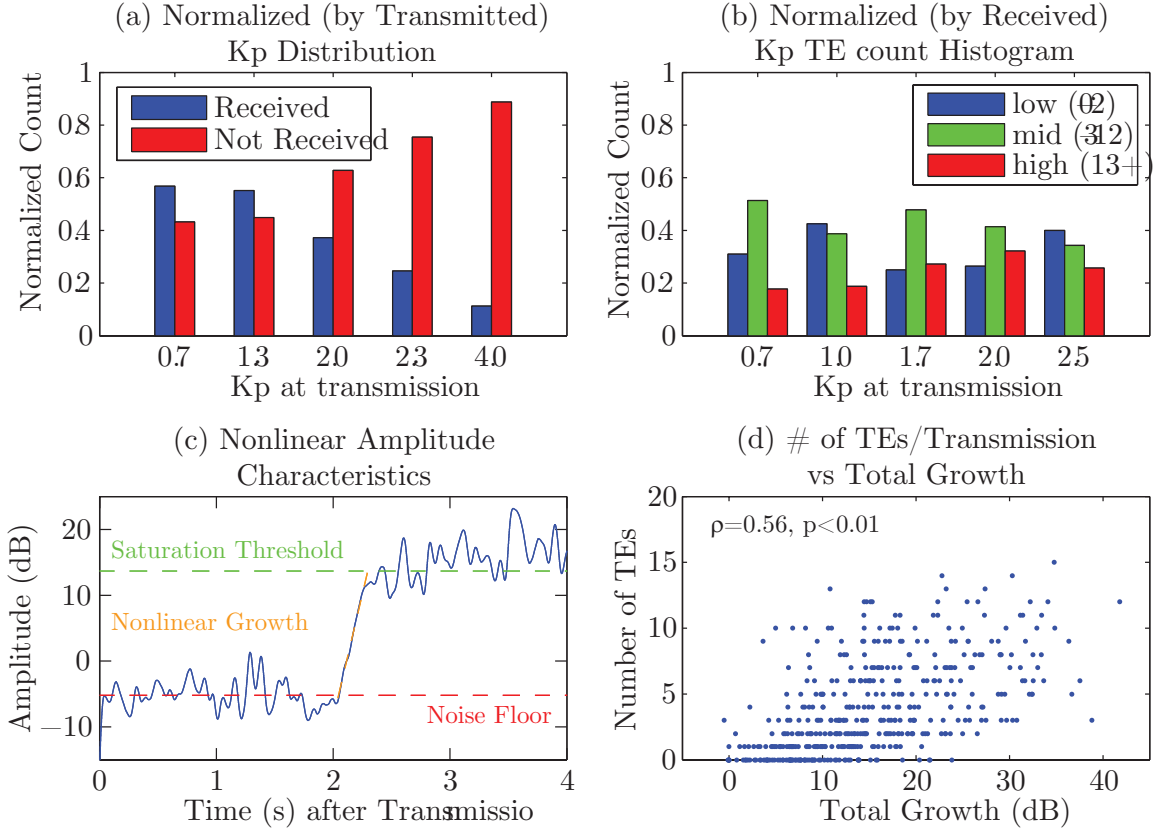


Figure 5.6: Five quantile Kp binned histograms of (a) receptions normalized by total transmissions with receptions in blue and non-detections in red, and (b) of cases with low (0-2) in blue, middle (3-12) in green, and high (13+) in red number of triggered emissions. (c) An explanation plot of the amplitude characteristics of the nonlinear growth phase of the injected signal provides context for the plot of (d) the number of triggered emissions excited by the long tone in a MDIAG transmission as a function of the total growth (saturation – noise) of the transmission. The total growth and the number of triggered emissions are linearly correlated with $\rho = 0.56$ with a p-value < 0.01 .

Furthermore, the observed frequency-time dispersion of the falling frequency ramps in the MDIAG format can be utilized to estimate the L -shell and the cold electron

density at the equator, N_{eq} , of the path of propagation [Golkowski, 2009, Section 3.2]. For the observations where the ramp element was present, we calculate the cold plasma parameters associated with the transmission. The L -shell ranges from ~ 3.5 to ~ 6.5 , and the N_{eq} values range from $\sim 1e - cm^{-3}$ to $\sim 600e - cm^{-3}$. No correlation is observed between the number of triggered emissions or the initial triggered emission frequency sweep rate and the L -shell of N_{eq} . This differs from the work by Nunn *et al.* [2005], which found a strong dependence of the emission sweep rate on the cold electron density at the equator. Hot plasma parameters from in-situ satellite measurements are not available for this intervals.

By applying a similar analysis method to triggered emissions from STACO transmissions of ± 1 kHz/s ramps, we extend our analysis to also compare the effects of an injected rising versus falling frequency ramp (although the amplitude analysis and the L -shell and N_{eq} comparisons are only applied to the MDIAG data). As the staircase tones approximate ramps quite closely, we can consider the vast majority of triggered emissions as having been triggered from the ramps, with the 100 ms tone approximation as the only exception. The results in Figure 5.7 show two histograms quantifying the net frequency change (a-b) and initial frequency sweep rate behavior (c-d) of triggered emissions excited from rising (left column) and falling ramps (right column), as well as two scatterplots (e-f) showing sweep rate versus frequency change. Again, all blue plot elements represent risers, while red elements represent fallers, and as before, the green elements in Figures 5.5(a-c) represent hooks. The plots in the left column correspond with triggered emissions from rising ramps, while the plots in the right column correspond with triggered emissions from falling ramps. The inset text in the top four subfigures describes the total number of risers (blue) and fallers (red) observed.

While the results from analyzing STACO transmissions, as shown in Figures 5.7(a-d), demonstrate similar ranges in net frequency change and initial frequency sweep rates as the MDIAG triggered emissions, the triggering effect of different transmission elements is significantly more pronounced. Rising ramps, (a) and (c), show a clear and strong preference for risers, with a median frequency increase of 391 Hz and a median initial sweep rate of 1.03 kHz/s, while the falling ramps, (b) and (d), show

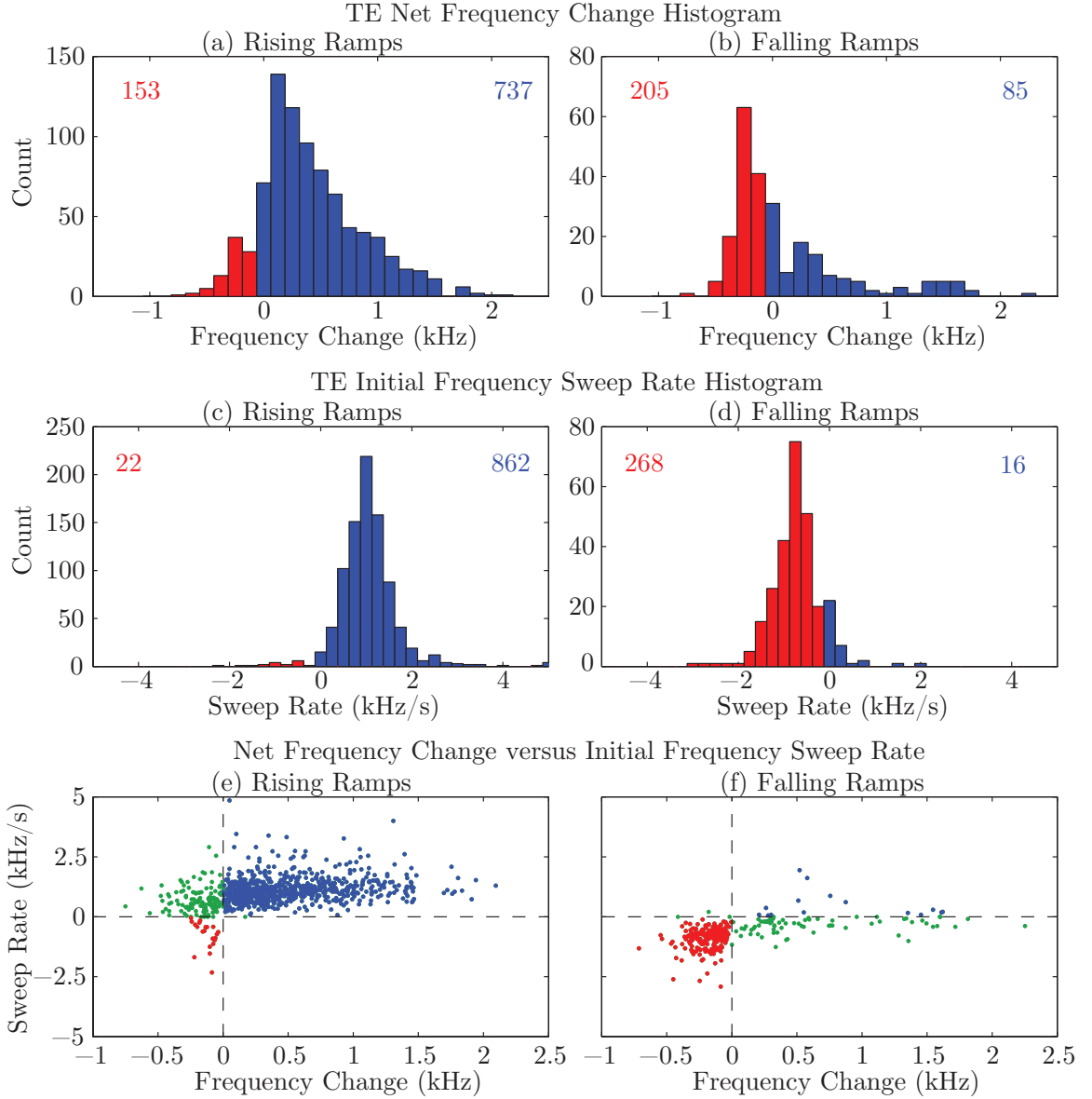


Figure 5.7: Analysis plots summarizing statistical observations and correlations of the time-frequency behavior of triggered emissions (TEs) excited from STACO transmissions. Histograms of net frequency change and initial frequency sweep rates of the triggered emissions are broken down by (a,c) rising and (b,d) falling ramps. Blue bars illustrate net risers, while red bars illustrate net fallers. (Net frequency change includes all triggering emission types that end with positive or negative frequency change, and net sweep rate includes all triggering types that begin with positive or negative sweep rates.) The numbers in each subplot describe the number of net risers (blue) and net fallers (red) observed. The scatterplots show the frequency sweep rate as a function of the net frequency change for (e) rising and (f) falling ramps. The dashed black lines show the zero sweep rate and zero frequency change boundaries with fallers in red, risers in blue, and hooks in green.

the opposite preference for fallers, with a median frequency change of -166 Hz and a median sweep rate of -0.73 kHz/s. This preferential triggering extends to the hooks generated, as shown in Figures 5.7(e) and (f), where rising ramps generate almost exclusively positive hooks (i.e., hooks that initially increase in frequency) and falling ramps negative hooks (i.e., hooks that initially decrease in frequency). Although the STACO and MDIAG falling ramps are both -1 kHz/s ramps, any difference in behavior may be attributed to the larger number of ramps in the STACO format and to human error in labeling the triggering element for the MDIAG format.

For reference, we have included tabulated results describing the median net frequency change and initial frequency sweep rate behavior of triggered emissions from MDIAG and STACO transmissions in 1986. Table 5.2 describes both the median frequency change for net risers and fallers and the median frequency sweep rate for initial risers and fallers, as triggered by long tones, short tones, falling ramps, and rising ramps. The breakdown further supports the result that characterizes risers as undergoing more frequency change than fallers as well as the observation that the transmission type or element plays a significant role in determining the initial triggering response such as in the initial frequency sweep rate. Several cells are left blank, due to an insufficient number of triggered emissions for analysis.

5.4 Discussion and Model Validation

These statistical characterizations of triggered emission behavior can be used to direct theoretical exploration and to constrain numerical simulations of triggered emissions. From Figures 5.4(a-f) and Figures 5.7(a-d), we find that overall, triggered emissions have a net frequency change between -1 kHz and 2.5 kHz and initiate with an initial sweep rate ranging between -2.5 kHz/s and 2.5 kHz/s. We also observe that risers appear to undergo a wider range in net frequency change than fallers, as noted by the spread in Figures 5.5(a-c) and to a lesser extent in Figures 5.7(e-f) and as summarized by the median frequency change values of 397 Hz to 601 Hz for the risers and of -145 Hz to -252 Hz for the fallers in Table 5.2. This typical triggered emission behavior is also illustrated in an alternate form by Figure 5.3(a), where the cone

		Net Riser Δ Frequency	Net Faller Δ Frequency	Initial Riser Sweep Rate	Initial Faller Sweep Rate
MDIAG	All	558 Hz	-198 Hz	581 Hz/s	-735 Hz/s
	Long Tone	601 Hz	-214 Hz	602 Hz/s	-726 Hz/s
	Short Tones	536 Hz	-155 Hz	520 Hz/s	-681 Hz/s
	Falling Ramps	536 Hz	-252 Hz	571 Hz/s	-817 Hz/s
	Doublet	—	—	—	—
STACO	All	397 Hz	-155 Hz	1017 Hz/s	-726 Hz/s
	Rising Ramps	391 Hz	-145 Hz	1025 Hz/s	—
	Falling Ramps	477 Hz	-166 Hz	—	-726 Hz/s

Table 5.2: Table of MDIAG and STACO Triggered Emission Statistics in 1986, illustrating the median frequency change for net risers and fallers and the median frequency sweep rate for initial risers and fallers triggered by each element of the MDIAG and STACO transmission formats. Net riser or faller indicates a triggered emission with overall positive or negative frequency change, and initial riser or faller includes a triggered emission with initial positive or negative sweep rate.

of higher occurrence illustrates the difference in frequency and time extent between the risers and fallers. This difference in behavior between risers and fallers hints at potential differences in conditions suitable for generation and sustained evolution of triggered emissions based on their initial type and may relate to the observed preferential amplification of rising frequency ramps in *Li et al. [2015a]*. While the precise physical mechanism is not yet known, one possible explanation is suggested by *Li et al. [2015a]*, which found that injected rising ramps are preferentially amplified due to favorable linear growth rate conditions that allow for an earlier initiation of nonlinear amplification. Similarly, risers may be preferentially amplified over fallers as the experimental conditions may allow for a larger range of frequencies to support continued amplification of risers. The linear growth rate curve as a function of frequency also decreases more rapidly as the frequency decreases but more gradually as the frequency increases. Nonlinear effects are also likely important, but some basic differences in behavior are already evident from the linear growth rate profile. There are some suggestions that the range of frequency change depends slightly on the initial frequency of the triggered emission as observed by the range of frequency changes

observed in Figure 5.5(d), but there are an insufficient number of receptions at higher f_{set} frequencies. Figure 5.3(b) also suggests that the overall frequency-time behavior of hooks can be considered as a combination of risers and fallers.

Another important result is that the format of the original triggering element directly impacts the resulting triggered emissions. Here, we clearly show that long tones [Figure 5.4(a,d)], short tones [Figure 5.4(b,e)], falling ramps [Figure 5.4(c,f) and Figure 5.7(a,c)], and rising ramps [Figure 5.7(b,d)] each exhibit a particular preference in the initial behavior of the triggered emission. Specifically, the differences in triggering behavior can be attributed to the two primary factors of duration and sweep rate of the triggering signal. We note that the difference in duration between the long tone and the short tones, and the difference in the rising versus falling ramps, result in the generation of quite different triggered emissions, where the long tone and rising ramps favor risers (45% and 51%) and positive hooks (29% and 45%) while the short tones and falling ramps favor fallers (49%, 56%, and 68%) and negative hooks (13%, 23%, and 25%). These differences in triggered emission types are illustrated by the traces of the different triggered emissions in Figures 5.1(d-f) and Figures 5.2(c-d) and broken down by percentage in Table 5.1. Consequently, any complete theory of triggered emissions should address the dependence on the form of the triggering signal, and numerical simulations of triggered emissions should be expected to reproduce a range of triggered emissions just by varying the signal duration and sweep rate. Despite this dependence on the form of the triggering signal, the triggered emissions can also become quite free-running at a later timepoint. This can be noted by the large number of hooks that are triggered which undergo varied frequency sweep rate changes over time, as shown in the aggregate by the hooks in Figure 5.3(b).

Theoretical treatment or numerical simulations of the triggered emission process should also reproduce wave amplification, as triggered emissions typically occur after the transmitted signal reaches saturation and ceases amplification, or when the signal terminates [Stiles and Helliwell, 1977]. However, the dependence of triggering behavior on signal amplitude leads to some difficulty in determining the exact theoretical contribution of the duration and sweep rate of the triggering signal on the triggered emission behavior, as the same two features also play a role in determining

the amplification of the triggering signal [*Helliwell and Katsufakis, 1974; Li et al., 2015a*]. Future examination of the two ramps of differing power in the MDIAG format may provide some insight into the effect of amplitude versus sweep rate on the resulting triggered emissions. We also note that the doublets produce very few triggered emissions, supporting the observed suppression effect due to wave-wave interactions [*Helliwell, 1983*]. The weak trend of more triggered emissions occurring when Kp at transmission is higher, from Figure 5.6(b), implies that more disturbed conditions reflect energetic particle distributions with higher free energy (or anisotropy), allowing for more triggering. Similarly, the moderate correlation between the number of generated triggered emissions and the total growth of the injected signals in Figure 5.6(d) implies that the energy available for nonlinear amplification relates to the energy available for the generation and amplification of triggered emissions.

The STACO triggered emission behavior, in Figure 5.7(a-d), also revisits the question regarding the time of termination of the triggering signal and the initiation of the triggered emission. *Stiles and Helliwell [1975]* first raised this question in observing that triggered emissions begin at the same frequency as the triggering signal and that the two signals could not be separated. At that time, *Stiles and Helliwell [1975]*, somewhat arbitrarily, defined only the unamplified signal as the injected or triggering signal. We revisit this question as the triggered emissions from the STACO ramps not only begin at the same frequency as the triggering signal, but also initiate at the same frequency sweep rate. For the rising ramps at 1 kHz/s, the triggered risers begin with a median initial frequency sweep rate of 1.03 kHz/s. And for the falling ramps at -1 kHz/s, the sweep rates of the triggered fallers are still quite close at -0.73 kHz/s. Tones may exhibit similar behavior with triggered emissions initiating with a 0 kHz/s sweep rate, but are difficult to detect as such behavior would simply appear to lengthen the tone. This behavior of the triggered emission as an extension or re-radiation of the injected signal may have implications in understanding the triggering process and may also tie in with the wave amplification process. As we note in simulations of wave amplification [*Harid et al., 2014a*], the amplification process can result in a lengthening of the injected pulse, which may actually correspond with the generation of a triggered emission.

We now briefly consider how our statistical observations might update the observations and features described by *Stiles and Helliwell* [1975]. *Stiles and Helliwell* [1975] provided a first statistical description of triggered emission behavior by analyzing the time evolution of spectral profiles of triggered emissions. In this study, the authors examined triggered emissions observed from several days in 1963 of constant frequency tones transmitted by the NAA and the Forestport, New York Omega transmitters and received at Eights Station, Antarctica, as well as constant frequency tones transmitted from Siple Station, Antarctica and received at Roberval, Quebec, Canada. Of the conclusions presented by *Stiles and Helliwell* [1975], we address the points regarding the time-frequency behavior (1-5,7). We agree (1) that triggered emissions "begin at the frequency of the transmitted signal" and for the most part (3-4) that the "initial low-amplitude portions of the [triggered emissions] stimulated by Siple ... are also fairly repeatable" and are generally well-behaved. In part, we also agree (2) that some triggered emissions, "regardless of their final slope, initially rise upon leaving the triggering frequency", but have noted several cases which do not conform to this behavior, such as falling frequency ramps that often trigger pure fallers. This conclusion may also depend on the power of the transmitted signal and be more accurate for the transmitted lower-powered tones in the original study of *Stiles and Helliwell* [1975]. We cannot comment for certain on (7) that "the generation process [of triggered emissions] is relatively independent of transmitter frequency and power", as we only examine data from Siple Station, which was also significantly more powerful in 1986 than in 1963. However, we believe that our observations of triggered emissions appear more varied than those reported in *Stiles and Helliwell* [1975]. Finally, we disagree strongly with (5) that the triggered emissions initiated by Siple transmissions "rarely drift more than 100 Hz above the triggering frequency before the triggering signal has terminated". In fact, we find that triggered emissions initiated by Siple signals can drift far more than 100 Hz from the triggering frequency before the injected signal terminates and can undergo very significant overall changes in frequency.

Similarly, we consider how our observations may update the features of triggered emissions covered in the review papers presented by *Matsumoto* [1979] and *Omura*

et al. [1991]. Of the features concerning the time-frequency behavior in *Omura et al.* [1991] (1-2,4), we agree that (1) triggered "emissions have a narrow bandwidth" and that (4) triggered emissions undergo considerable "total frequency change" and can exhibit "complex emission forms". However, we disagree with (2) that triggered emissions are "long enduring" with a duration "many times that of the triggering pulse." Instead, we find that although there are emissions of long duration, many triggered emissions endure for only a short time, commonly lasting less than 0.5 s and for a shorter duration than the triggering pulse. Overall, our observations illustrate that triggered emissions are even more complex and varied in behavior than earlier observations indicated, with greater observed ranges in the extent of frequency change and of triggered emission duration.

These statistical bounds and features can be used to validate numerical simulations of triggered emissions. Next, we compare our statistical observations with three types of models used to simulate triggered emissions. Of the many approaches, for instance described in Table 1 of *Omura et al.* [1991], we consider simulation results from two Vlasov type codes by *Nunn et al.* [2003] and *Harid et al.* [2014a], a PIC approach by *Hikishima and Omura* [2012], and a phenomenological theory by *Helliwell* [1967]. These approaches are fairly successful in reproducing aspects of triggered emissions. *Nunn et al.* [2003] produces a canonical riser and faller and a reasonable hook. *Harid et al.* [2014a] models wave amplification but shows how triggering can occur at the termination of an injected signal. *Hikishima and Omura* [2012] also generates risers, and *Helliwell* [1967] demonstrates how to reproduce the spectral form of a given triggered emission. The primary limitation is that each approach only reproduces limited features or a limited type of triggered emissions. The VHS code by *Nunn et al.* [2003] reproduces all three types of triggered emissions, but the bandwidth constraints of the code do not accurately reproduce the observed triggered emissions bandwidths and require additional and somewhat artificial constraints in order to reproduce saturation effects which may play a role in determining triggered emission occurrence. *Harid et al.* [2014a] does not require bandwidth filtering constraints but only generates triggered emissions with quite limited frequency change. The PIC approach of *Hikishima and Omura* [2012] requires few assumptions and addresses a

number of other physical characteristics but is limited to producing risers with sweep rates on the order of 1 kHz/s. These results of the numerical simulations contrast directly with our statistics, which show triggered emissions of all types being generated by the same injected signal in the same duration and with frequency changes on the order of several kHz. Even when the sweep rates are reasonable, such as a riser sweep rate of 2 kHz/s and a faller sweep rate of -2 kHz/s, the frequency change extent may push the limits of our observations, where the riser undergoes a frequency change of 1.5 kHz and a faller -2 kHz [Nunn *et al.*, 2003]. In addition, the spectral forms of the modeled triggered emissions [Nunn *et al.*, 2003; Hikishima and Omura, 2012] are often also of a very simple time-frequency form unlike the complexities observed in the data. On the other hand, the phenomenological theory presented by Helliwell [1967] can reproduce a wide range of observed triggered emissions but requires a large number of free parameters, making parametric simulation rather complicated. To aid in the development of reasonable models, we suggest a number of features that should be reproduced. Most importantly, the model should be able to generate a wide range of frequency sweep rates and reach a wide range of frequency changes, in accordance with observations of triggered emissions. Furthermore, different types of injected elements should trigger proportionally different types of triggered emissions.

5.5 Conclusions

The understanding and modeling of the generation of ELF/VLF triggered emissions continue to pose a challenge for further scientific work, and advances in theoretical explanations and in numerical simulations can aid in the understanding of broader aspects of wave-particle interactions in the magnetosphere. While different models can successfully model aspects of triggered emissions, no single simulation approach captures the full range of triggered emission behavior as observed in the data. To aid in theoretical and modeling efforts to reproduce the full behavior of triggered emissions, we present an improved data set of 4650 triggered emissions generated from two different formats transmitted by the Siple Experiment over nine months in 1986. Using our database of triggered emissions, we find a number of results that are

summarized below:

1. Triggered emissions can exhibit a wide range of frequency sweep rates, between -2.5 kHz/s and $+2.5$ kHz/s, and undergo significant frequency change between -1 kHz and 2.5 kHz. The emissions can last up to several seconds, usually no more than 4 s but can also be quite short, <0.5 s.
2. Triggering behavior at the initiation of triggering appears to depend on the transmitted element but can become quite free-running at a later time point.
3. The orientation of transmitted frequency ramps is very important to determining the initial triggered emission profile. Rising ramps generate initial risers 97.5% of the time, while falling ramps trigger initial fallers 94.4% of the time. And the resulting triggered emission sweep rates, 1.03 kHz/s for risers and -0.73 kHz/s for fallers, are close to the transmitted ramp's sweep rate of ± 1 kHz/s.
4. The duration of constant frequency tones plays a role in determining the initial triggered emission profile. Long tones (2-s) generate initial risers 74.5% of the time, while short tones (200-ms) trigger initial fallers 61.9% of the time.
5. Risers tend to undergo larger frequency change (median changes from all triggering elements between 397 Hz and 601 Hz) than fallers (median changes of -145 Hz to -252 Hz), regardless of the triggering element. And risers can endure for longer duration (<5 -s) than fallers (<2 -s).
6. The number of triggered emissions is linearly dependent on the total growth of the transmitted signal and may correlate with more disturbed geomagnetic conditions, as describe by the Kp index.

These results substantially improve the statistical understanding of triggered emission behavior. We expect that these statistical bounds would be useful in directing theoretical examination of the triggering process and in validating numerical simulations to better understand wave-particle interactions in the magnetosphere. Further work in analyzing the amplitude behavior of triggered emissions may also be useful for comparing observations and theory.

Chapter 6

Predicting Conditions for Siple Receptions

Wave injection experiments provide an opportunity to explore and quantify aspects of nonlinear wave-particle phenomena in a controlled manner. Waves are injected into space from ground-based ELF/VLF transmitters, and the modified waves are measured by radio receivers on the ground in the conjugate hemisphere. These experiments are expensive and challenging projects to build and to operate, and the transmitted waves are not always detected in the conjugate region. We consider the application of more modern machine learning techniques in order to predict conditions for the reception of one-hop signals from the Siple Transmitter Experiment. The present work is in review as [Li et al. \[2015c\]](#).

The Siple Transmitter Experiment generated a substantial volume of data, but early work typically focused on individual examples and case studies, making generalizations of behavior relying on anecdote rather than statistics. In the years since the Siple Experiment, significant advances in computational resources allow us to digitize, store, and process large volumes of data in order to rigorously quantify the range of observed nonlinear effects. One particular limitation of working with data from the Siple Experiment has been the relatively low rate of reception in the conjugate hemisphere, with only $\sim 40\%$ of Siple transmissions being detected [[Gibby, 2008](#); [Li et al., 2015a](#)]. In order for Siple signals to be observed in the conjugate hemisphere,

they must propagate in the magnetosphere within field-aligned density irregularities known as ducts [Angerami, 1970]. The reception of signals transmitted from Siple is more likely when geomagnetic conditions are less disturbed [Carpenter and Bao, 1983; Li et al., 2014]. This requirement for quieting in Kp was also observed in wave injection experiments using the HAARP ionospheric heater [Golkowski et al., 2011] and was attributed to the formation of stable ducts. Figure 6.1(a) shows a superposed epoch analysis of the Kp index from 4 days before to 2 days after the time of transmission for Siple transmissions received and not received in the conjugate hemisphere. There is a significant difference, as described by a Kolmogorov-Smirnov significance test as shown in Figure 6.1(b), in the geomagnetic conditions characterized by the Kp index with a period of quieting beginning several days prior to intervals with successful receptions of transmissions, indicating the potential utility of using the Kp index to evaluate in advance conditions suitable for the reception of magnetospherically propagating signals.

The key information that allows for detecting a Siple transmission at the receiver comes from transmission logs which detail the transmission format (the frequency-time elements transmitted in a set sequence), the transmission time, and the f_{set} transmission frequency (the central tuning frequency to which transmitted elements were referenced). While the most thorough detection method would be a visual inspection of spectrograms of data from the conjugate region and manual detection of receptions, this manual identification process does not scale with the amount of data and becomes too time consuming as the amount of data increases. Another method attempts to automatically detect signals using a signal amplitude threshold that determines if a sufficiently strong signal is above the noise floor [Li et al., 2014], but this approach suffers from inherent limitations in only detecting strongly amplified signals in the presence of low background noise conditions and is not sufficiently robust. Here, we demonstrate the application of machine learning classification techniques as a preprocessing step for selecting intervals when receptions may be significantly more likely. There has thus far been limited work in the space physics community taking advantage of more recent machine learning techniques, and most such results, using for instance support vector machines, tend to be for regression models [Gavrishchaka

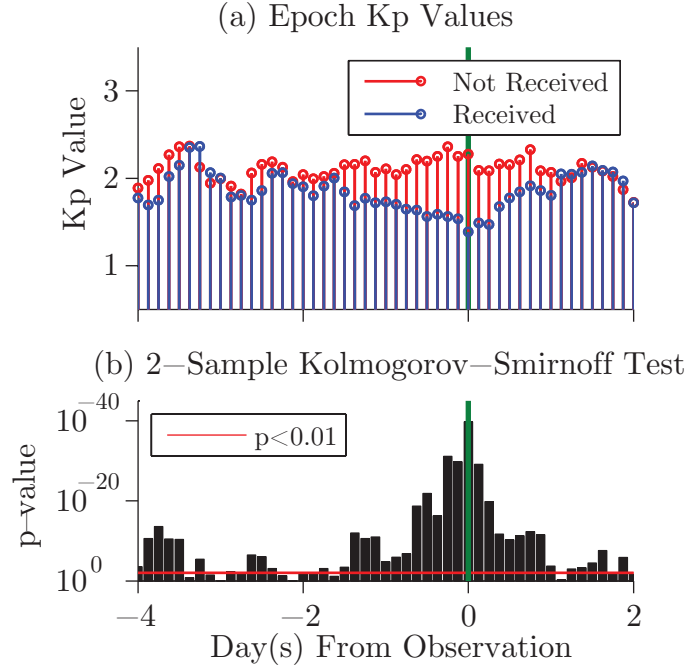


Figure 6.1: (a) Superposed epoch analysis of the mean Kp index over a 6 day period of MDIAG transmissions detected (blue) and of transmissions not detected (red) at the receiver in the conjugate hemisphere. (b) The p values for a two-sample Kolmogorov-Smirnoff statistical significance test are plotted for each 3 hour interval, and the y-axis is inverted so that the more significant p values are better highlighted. This figure is an updated version considering a larger number of transmissions from Figure 4 in [Li et al. \[2014\]](#) and is also shown in Chapter 3.

[and Ganguli, 2001](#); [Ji et al., 2013](#); [Yue et al., 2015](#)].

Given the significant difference in the Kp index between received and not received Siple transmissions, we apply two methods for classifying transmissions to develop a model for predicting intervals of receptions of Siple transmissions at Lake Mistissini based on the geomagnetic Kp index from the 6 days preceding the time of transmission. Both methods, a naive Bayes classifier with Laplace smoothing and a support vector machine classifier, have prediction accuracies of 80%-90%. We also demonstrate the statistical advantages of these classification approaches by using the detected cases to update the statistics on nonlinear growth rate and total growth of injected signals first presented in [Li et al. \[2014\]](#). Applying these classifier approaches

using the Kp index to experimental studies may allow for more efficient experiments by selecting transmission times and conditions that are significantly more likely to result in reception, and these techniques may provide insight into understanding the conditions that lead to wave amplification from wave-particle interactions. Applying these classifiers to our Siple data set, we detect the improved set of 406 receptions of Siple transmissions analyzed in Chapter 3.

6.1 Machine Learning Techniques for Prediction of Receptions

Considering the amount of data generated by Siple Station, most of the earlier work chose to focus on key case studies or on interesting observed phenomena, with fewer studies leveraging the entire data set. With transmissions being detected only $\sim 40\%$ of the time, additional preprocessing and examination of the data would be needed in order to select cases with received transmissions for study. Traditionally, this preprocessing would involve a manual selection of detected receptions, but we demonstrate here the application of machine learning techniques for automatically detecting receptions.

We use two methods for classifying transmissions to develop a model for predicting Siple transmission receptions at Lake Mistissini based on the geomagnetic Kp index from the 6 days preceding the time of transmission. Both methods, a Naive Bayes classifier with Laplace smoothing and a support vector machine classifier, have prediction accuracies of 80%-90%. We also demonstrate the statistical advantages of these classification approaches by using the detected cases to update the amplification statistics from [Li et al. \[2014\]](#). Applying these classifier analyses using the Kp index to experimental studies may allow for more efficient experiments by selecting transmission times and conditions that are significantly more likely to result in reception, and these techniques may provide insight into understanding the conditions that lead to wave amplification from wave-particle interactions.

6.2 Classification Methodologies

Although there are many different classification techniques, we consider two simple supervised learning methods for classification, naive Bayes with Laplace smoothing and support vector machines. We first describe the common data set used for both classification approaches, including the generation of the ground truth labels describing signal reception and the Kp geomagnetic indices used as the input feature set, and then provide some intuition regarding the two classification techniques. While a naive Bayes classifier is a commonly first implemented classifier to determine the effectiveness of applying machine learning techniques, a SVM classifier is a more sophisticated and computationally intensive method that often yields more accurate predictions although its internal parameters are more opaque.

6.2.1 The MDIAG Data Set

The data set is comprised of observations of transmissions of a mini-diagnostic (MDIAG) format during 1986. This data set builds on the data set first developed by [Li et al. \[2014\]](#), in focusing on this single transmission format transmitted by Siple from April to December of 1986 and observed at the conjugate receiver at Lake Mistissini (LM). The MDIAG format, first discussed in Section 3.1 and described again here for reference, was a frequently transmitted format with a variety of elements used to evaluate the conditions for transmitting different subsequent formats and is illustrated in Figure 6.2(a). The format begins with a 2-s tone at the central tuning frequency, f_{set} (with an amplitude ramp from 10 dB to 0 dB over the first second), followed by a descending staircase of five 200 ms tones spaced 250 Hz apart from $f_{\text{set}} + 500$ to $f_{\text{set}} - 500$, two descending frequency ramps (the first at 0 dB and the second at 6 dB) over the same frequency range for 1 s each, and a 7 s long pair of constant frequency tones (called a doublet) at $f_{\text{set}} + 480$ and at $f_{\text{set}} + 510$ at 0 dB. These elements can be visually identified on spectrograms in order to determine if the transmission was received in the conjugate hemisphere.

In 1986, we have data for 1093 transmissions of the MDIAG format, and as shown in Figure 6.2(b), not all transmissions were received and detected at Lake Mistissini.

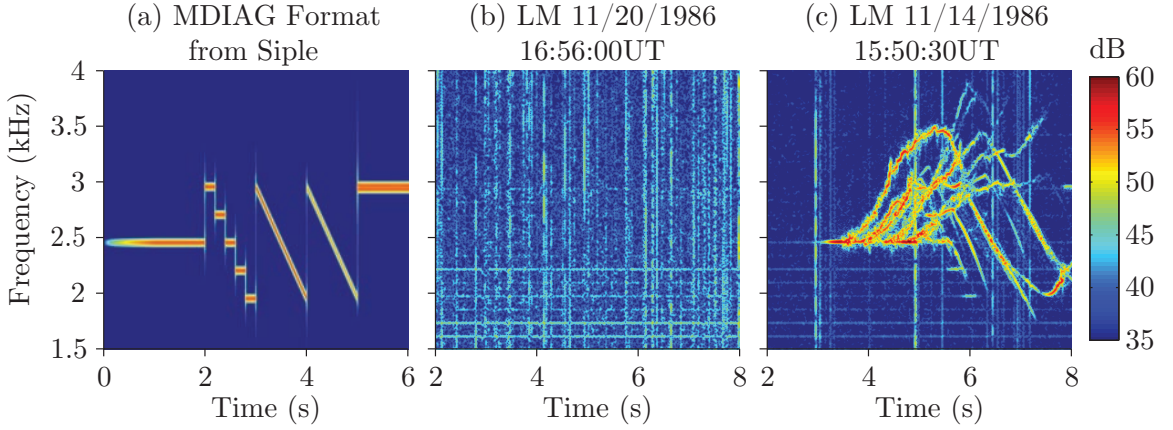


Figure 6.2: (a) Illustration of the MDIAG transmission format transmitted from Siple Station, and conjugate observations at Lake Mistissini (LM) showing examples of a case where (b) the transmission was not received and (c) the transmission was received.

To develop ground truth labels describing the detection of receptions of MDIAG transmissions, we process each MDIAG case into high frequency and time resolution spectrograms and manually determine if the MDIAG transmission is observed through a visual inspection of the spectrogram, as in Figure 6.2(c). Of the 1093 transmissions, 423 receptions were detected and 670 were not detected, giving a 39% reception rate. This matches well with general statistics compiled by [Gibby \[2008\]](#) and with the smaller number of transmissions of a different format studied in [Li et al. \[2015a\]](#). We label the received transmissions as Class 1 and the not received transmissions as Class 0.

We select the Kp index as the input feature for the classification methods, in particular the Kp index from the 6 days preceding the time of transmission and including the Kp index at transmission. The Kp index was chosen by noting that receptions generally occur when the geomagnetic condition as described by Kp is less disturbed [[Carpenter and Bao, 1983](#)] and that geomagnetic conditions described by the Kp index differ between cases of reception and non-reception [[Li et al., 2014](#)]. The 6 days preceding the time of transmission were selected to include the entire window of time originally chosen for conducting the epoch analysis of Kp behavior for received and not received cases shown in Figure 6.1(a). An analysis of the significant intervals

from Figure 6.1(b) may indicate that fewer days may suffice as well.

6.2.2 Naive Bayes with Laplace Smoothing

The naive Bayes classifier belongs to the class of generative learning algorithms that model the distributions of the input features for each class the algorithm is trying to learn. Generative learning algorithms are a supervised learning approach, which requires the training data to first be manually labeled. By assuming that the features are conditionally independent given the class, the resulting algorithm is the well-understood naive Bayes classifier [Rish, 2001]. In practice, the naive Bayes classifier works by first training the conditional probability of each feature given each class. This corresponds with maximizing the likelihood of a given class occurring given a set of features. Then, using the conditional probabilities trained for each feature, new cases can be evaluated by calculating the conditional probability for each class and assigning a label for the class that is more likely. Laplace smoothing adds a small, but non-zero probability to the conditional probabilities for all of the features in order to prevent results with an indeterminate form, that is both the numerator and denominator are 0. This small added probability extends the functionality of the classifier to generate predictions for cases with new features that were not identified in training. In the work presented here, the class labels are “1” for received transmissions and “0” for not received transmissions. As the Kp index can vary substantially and the quieting may be the important characteristic indicating suitable ducting conditions for propagation, we instead used the change in Kp between 3-hr intervals as the input feature for the naive Bayes classifier. Furthermore, as the input features to these Bayes classifiers must be binary valued, we implement a simple binary representation by creating a large lookup table binary array.

6.2.3 Support Vector Machines

Support vector machines were developed by Cortes and Vapnik [1995] and have become a widely used algorithm in the machine learning community. SVMs can be conceptualized as a way of separating the data by its features into distinct classes

by projecting the data into a higher dimensional space where the classes can then be separated by a hyperplane. The projection depends on the chosen mathematical transformation, called a kernel, and the hyperplane maximizes the distance to the closest points. The set of the closest points to the hyperplane are then called support vectors. As the kernel transformation of the input features for the hyperplane separation is more opaque to understanding the specific workings of the classifier and as the input features do not need to be binary valued, here we use the Kp indices directly as the input data features. We implement this SVM classifier utilizing a standard, off-the-shelf implementation called LibSVM by [Chang and Lin \[2011\]](#).

6.3 Classification Results

We apply these two classification techniques to the MDIAG data set, using the Kp indices from the 6 days preceding the time of transmission to automatically predict whether or not the MDIAG transmission is detected. First, we train the naive Bayes classifier feature weights and the support vector machine classifier model on a training set composed of 810 transmissions, with 317 detections and 493 undetected cases so that the training set distribution of detected and undetected cases is reflective of the overall reception rates in the data. Then, we evaluate the accuracy of the models and verify their validity by analyzing their predictions given a new set of testing data, the remaining 283 cases, with 106 detections and 177 undetected cases, which were never used in the training of the models. For the amount of data considered here, both models take a negligible amount of time to train and to generate predictions.

The prediction results and how they compare with the ground truth labels are shown in a confusion matrix in Table 6.1. The upper half describes the results for the Bayes classifier, and the lower half for the SVM classifier. The left column describes results for the training data, and the right column the results for the test data. The numbers indicate the predicted or observed number of transmissions. Overall, the accuracy for the Bayes classifier is 90% (732/810) for the training data and 88% (250/283) for the test data. The accuracy is representative of the predictive capability of the classifier, with a high precision (correctly predicted detections divided

		Observations of MDIAG Training Transmissions		
		Total	Received	Not Received
		810	317	493
Bayesian Predictions	Received	301	270	31
	Not Received	509	47	462
SVM Predictions	Received	300	278	22
	Not Received	510	39	471

		Observations of MDIAG Test Transmissions		
		Total	Received	Not Received
		283	106	177
Bayesian Predictions	Received	111	92	19
	Not Received	172	14	158
SVM Predictions	Received	115	97	18
	Not Received	168	9	159

Table 6.1: Confusion matrix showing the prediction results of MDIAG reception and non-reception for the Bayesian and SVM classifiers. The confusion matrix describes the true and false positives and negatives for each classifier, with the top table describing the classifier results from the training data and the lower table describing the results from the test data.

by all predicted detections) of 90% and of 83% and a high recall (correctly predicted detections divided by all detections) of 85% and 87% for the training and test data respectively. The results for the SVM are similar, if not slightly better. The accuracy is 92% and 90%, the precision is 93% and 84%, and the recall is 88% and 92% for the training and test data respectively. Incorrectly classified cases reveal transmissions where the Kp behavior of received cases more closely resembles the Kp behavior of non-reception transmissions, and a visual examination of the transmissions shows that these receptions are also usually weaker and less active.

Both classifiers perform well, with 80% to 90% accuracies in predicting the reception and non-receptions of transmitted Siple MDIAG signals. This compares favorably with the actual reception statistics, where the transmissions were detected only 40% of the time, and may prove useful for guiding the operations of future wave injection experiments or further analysis of the historic Siple dataset. As Kp is a global geomagnetic index with a 3-hour resolution, efforts were made to consider the potential improvement in prediction by using local magnetometer stations and by using a geomagnetic index with higher time resolution. However, using data from three Canadian K indices stations, at Meanook, Ottawa, and Victoria, as the input features for both the Bayes and SVM classifiers did not improve the prediction accuracies. Similarly, using the 1-minute AE index as the input feature to improve the time resolution was not successful as the higher time resolution resulted in too large of an input feature set, leading to overfitting and to ill-suited classifiers.

While the SVM classifier is opaque to understanding the structure of the hyperplane and how the data is classified, we can consider the structure of the Bayes classifier. The Bayes classifier generates probabilities for each element in the feature set, and an examination of these probabilities may indicate additional details. Some precision in interpreting these results are required though, as each element in the feature set describes a given change in Kp index between intervals for a given day preceding transmission. We find that the most predictive element, indicating that reception is 42 times more likely, is the token describing an increase in Kp index of 2 units during the interval 3 days before the time of transmission. This result is interesting in pointing out that not only is the overall quieting needed for the formation of a stable duct for wave propagation, but also a prior interval of higher geomagnetic activity, presumably associated with the injection of energetic electrons into the inner magnetosphere, is also key to driving the wave amplification such that reception of signals in the conjugate region is possible.

6.4 Conclusions

As the scale of data increases and the scope of experiments include many more cases, more sophisticated techniques for detection or classification may become more useful. Looking at a set of experiments from the Siple transmitter experiment in 1986, we demonstrate the application of a naive Bayes with Laplace smoothing classifier and a support vector machine classifier for the automatic detection of transmitted MDIAG transmissions received at the conjugate receiver at Lake Mistissini. The presented problem is non-trivial with 1093 transmissions that are received at a 39% reception rate for a total of 423 receptions. The classifiers take as input features the Kp indices from the preceding 6 days to predict the reception of transmissions with 80%-90% accuracy. This work suggests further utilization of machine learning techniques for active experiments in maximizing the number of detectable receptions for scientific analysis, especially with the higher accuracies afforded by more sophisticated techniques such as the SVM classifier. By analyzing the Bayes classifier probabilities, we find that the most predictive token is a period of increasing activity 3 days prior to transmission. Thus, we conclude that reception of Siple signals requires a period of higher geomagnetic activity, which results in higher fluxes of energetic electrons for wave amplification, followed by a period of quieting, which results in the formation of stable ducted paths for wave propagation.

Chapter 7

Conclusions and Suggestions for Future Work

7.1 Summary of Contributions

The wave-particle interactions between energetic electrons in the Earth's radiation belts and electromagnetic whistler-mode waves are an important driver of space weather dynamics and provide insight into understanding the interactions as a fundamental concept in plasma physics. However, the interactions have been and remain difficult to study given the size scales involved. As a result, a quantitative understanding of the results of the wave-particle interactions, in particular the modification of the waves, has been lacking. In this dissertation, a comprehensive examination of controlled wave injection experiments from the Siple transmitter experiment in 1986 has been conducted in order to develop a statistical description of wave amplification and of triggered emission behavior.

Much effort has been undertaken to restore and preserve data collected during the Siple Transmitter Experiment, producing nearly 7000 hours of data digitized from magnetic tapes and post-processed to eliminate frequency drifts and timing errors inherent in the data. An analysis of the diagnostic format (MDIAG) used to study wave amplification established statistical bounds on the nonlinear growth rate, saturation threshold, and an estimate of the total growth using some 406 receptions, with

an additional subset of 14 cases highlighting the separation of phases of linear and nonlinear growth. These statistical bounds on the total growth, 3–41 dB with a median growth of 18 dB, and on the nonlinear growth rates, 3–270 dB/s with a median growth rate of 68 dB/s, can be used to constrain theoretical and modeling efforts to understand and numerically simulate wave amplification. A particular example is provided in this work where the preferential amplification of injected rising and falling frequency ramps using a ramp approximation (STACO) format is quantified and then modeled and interpreted using a narrowband Vlasov-Maxwell simulation. Measurements of the total excitation by each ramp element from the observations find that the rising ramps amplify on average 1.9 times more than falling ramps, and the modeling efforts using the *Harid et al.* [2014a] Stanford Finite Difference Vlasov Solver reveal that the preferential amplification effect is driven by the conditions setup by the initial linear amplification of the waves.

In addition to studying the nonlinear amplification of injected whistler-mode waves, this work also addresses a long-standing question concerning the nonlinear generation of new waves in examining triggered emissions. A significant amount of theoretical and numerical work concerning triggered emissions has been conducted over the last 50 years and ties in with better understanding of the wave-particle interactions that drive natural processes such as chorus in the magnetosphere. While some previous work, notably *Stiles and Helliwell* [1975] and *Stiles and Helliwell* [1977], has explored the range of triggered emission behavior, there has not been a thorough analysis of triggered emissions during Siple’s later years of operation, when its transmitter was significantly more powerful and flexible. In this work, we consider 4650 triggered emissions analyzed from the 406 MDIAG transmissions and 63 STACO transmissions to provide a quantitative understanding of the behavior of generated triggered emissions. Descriptions of emission frequency change and initial frequency sweep rate, between -1 kHz and 2.5 kHz and within ± 2.5 kHz/s, and their observed dependence at triggering upon the transmitted signal element substantially improve the bounds for directing further theoretical and numerical work in explaining triggered emissions. Furthermore, the number of triggered emissions appears to depend on the total amplification of the transmitted signal and possibly with more active

geomagnetic conditions.

Because of the large amounts of data generated in the Siple experiment, a number of different detection methods were implemented as a pre-processing stage in order to select data with received transmissions for further analysis. Three methods were explored in this work: manual detection, signal amplitude thresholding, and machine learning classifiers using the Kp index. Manually identifying observations of transmitted signals generate ground truth detections but are time-consuming and difficult to scale to large amounts of data. Signal amplitude detection by a variable estimated noise threshold is more automated but is limited to detecting strongly amplified transmissions under quiet conditions. The two machine learning classifiers, a Naive Bayes with Laplace smoothing classifier and a Support Vector Machine classifier, are simple to implement and are quite accurate, with prediction accuracies of 80%-90%. The capability of these more sophisticated machine learning techniques indicate an underlying predictable dependence on the geomagnetic conditions as parameterized by the Kp index for conditions that allow for the reception of injected whistler-mode signals.

7.2 Suggestions for Future Work

While this work has significantly improved the statistical bounds from the data that constrain theoretical interpretation and numerical simulation, further analysis would extend the results to more general applications. At the moment, this work is limited by its timing in 1986, at a solar cycle minimum, and a methodical examination of more Siple data could address implications for any time in the solar cycle. However, that approach does also suffer from the historical realities of differences in the Siple transmitter capability over the fifteen years of operation of the experiment. These differences could be addressed as the data are analyzed, but a new transmitter experiment would be most ideal for further experimental work. Alternately, a coupled study between highly accurate lightning networks and ground-based receivers could resume observations of wave-particle interactions using whistler observations over a wider range of L-shells.

Continued work in theory and modeling should consider the statistical results described in this work and take advantage of the example provided by Chapter 4 in validating models with data. Further work should also utilize the ramp elements in many of the transmission formats for estimating the L -shell and equatorial electron density of receptions of Siple signals. At the very least, further simulations of emissions, triggered emissions or chorus emissions, should consider the bounds place on triggered emissions as described in Chapter 5. Finally, the machine learning classifiers or predictors are the quite promising for leverage large data sets for a large scale analysis and data mining. These predictors may have utility in retroactively examining past data sets or for future aid in conducting new wave injection experiments or in the operation of VLF transmitters at comparable latitudes.

Appendix A

1986 Data Spectrograms

Space is always limited in displaying spectrogram examples of data, and here we include several additional spectrogram examples to better illustrate the range of behavior observed in the data. The time of the transmission is provided in the title of each figure, and the time on the x-axis is the time from the time of transmission. Colorbars should be normalized and calibrated, although not to real units, but are mainly included to provide context for the range in amplitude in the spectrograms.

A.1 Mini-Diagnostic (MDIAG) Data

The MDIAG format is the most commonly transmitted format and is the format studied in Chapter 3 and in Chapter 5. Again, the format includes a long tone with a power ramp, 5 short tones in a descending staircase, two frequency ramps where the second ramp is weaker, and a paired tone called a doublet. Here, we present 12 sample MDIAG receptions spread out throughout most of 1986, covering a wide range of differences in amplification and in triggering. A brief description of the particular feature of interest is mentioned in each caption. Each reception is normalized to the local calibration tone, allowing for comparisons of relative amplitude between receptions.

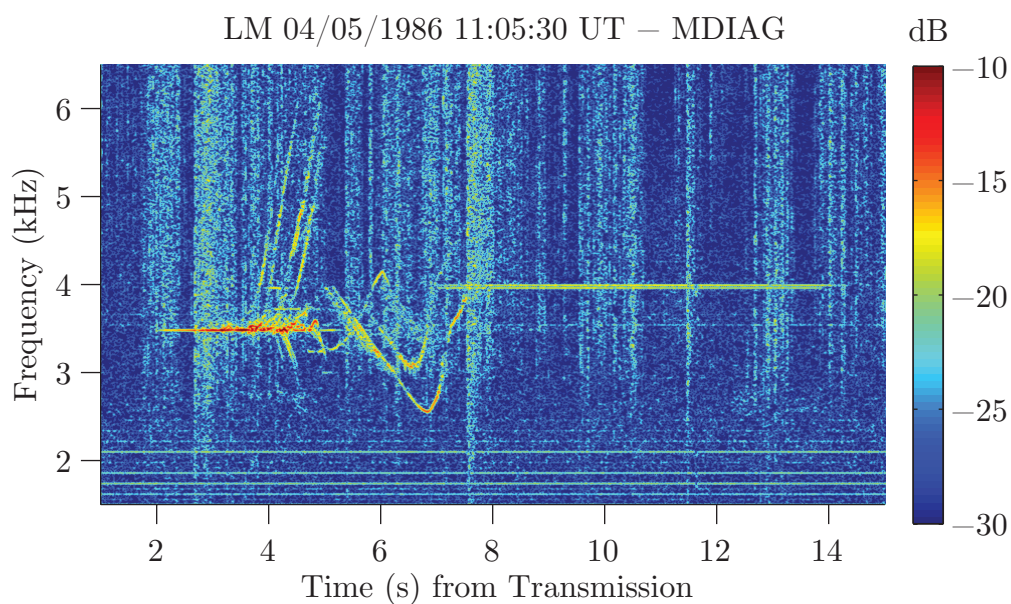


Figure A.1: A fairly typical example with most the of transmission elements present, and a number of different risers, fallers, and hook triggered emissions.

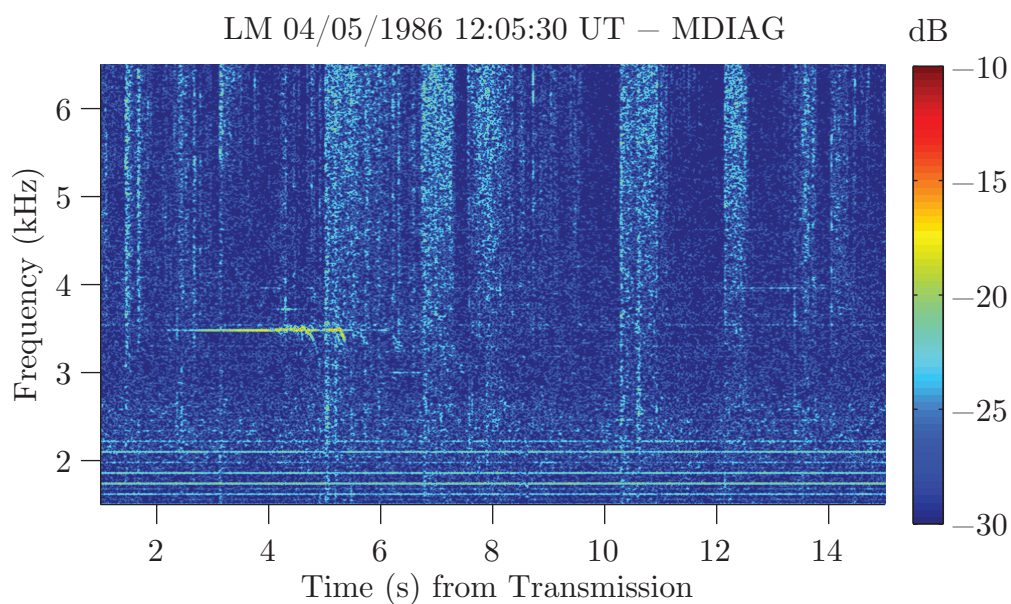


Figure A.2: Only the tones are detected and only the long tone is amplified strongly above the noise floor. Three small triggered fallers are present along the long tone.

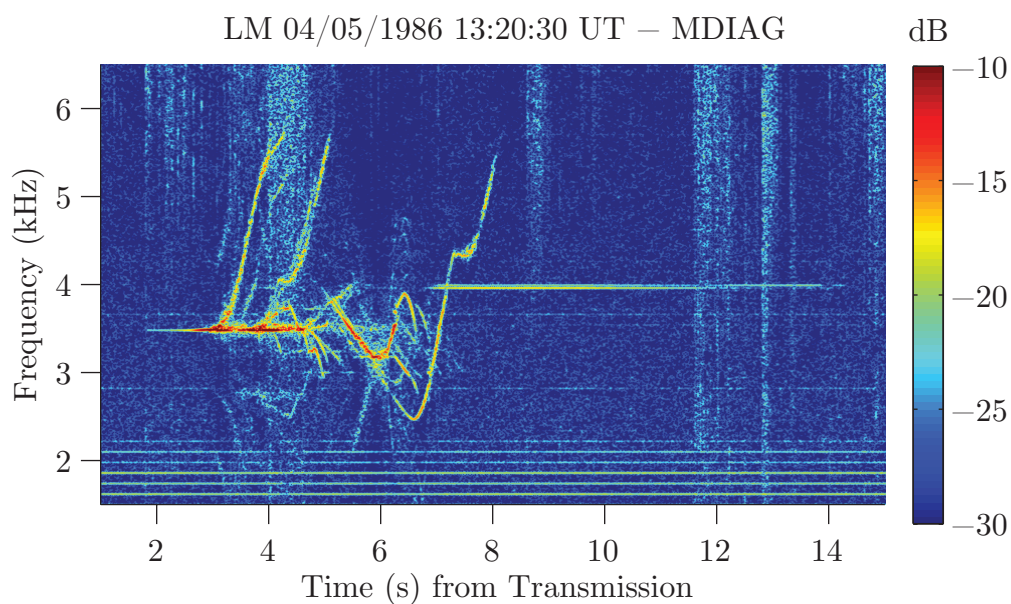


Figure A.3: Active reception with propagation occurring along several paths as illustrated by the additional ramp elements.

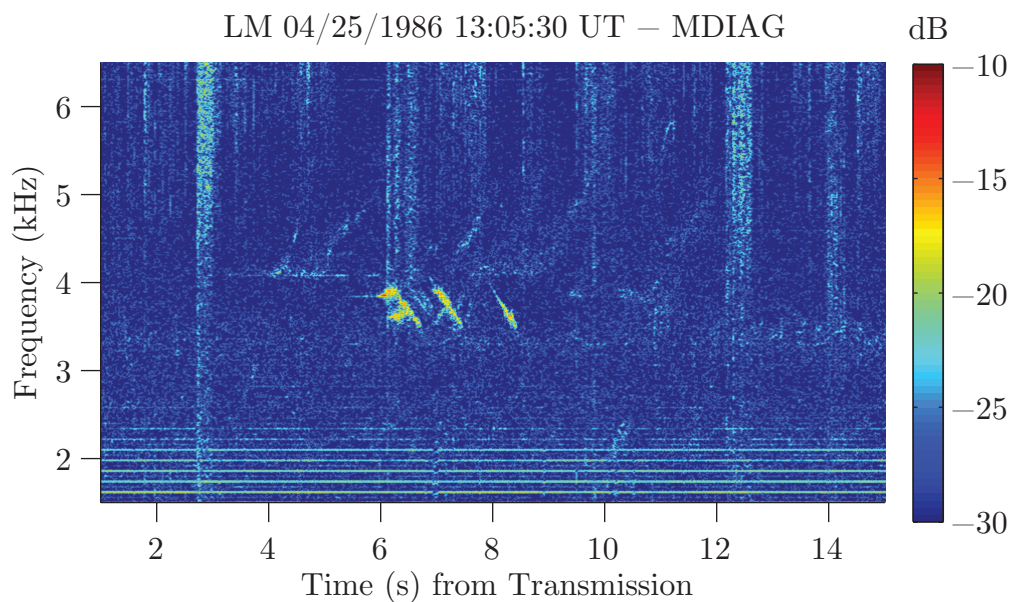


Figure A.4: Unusual reception where only lower frequency components of the transmission were amplified. The long tone is present, but greatly attenuated.

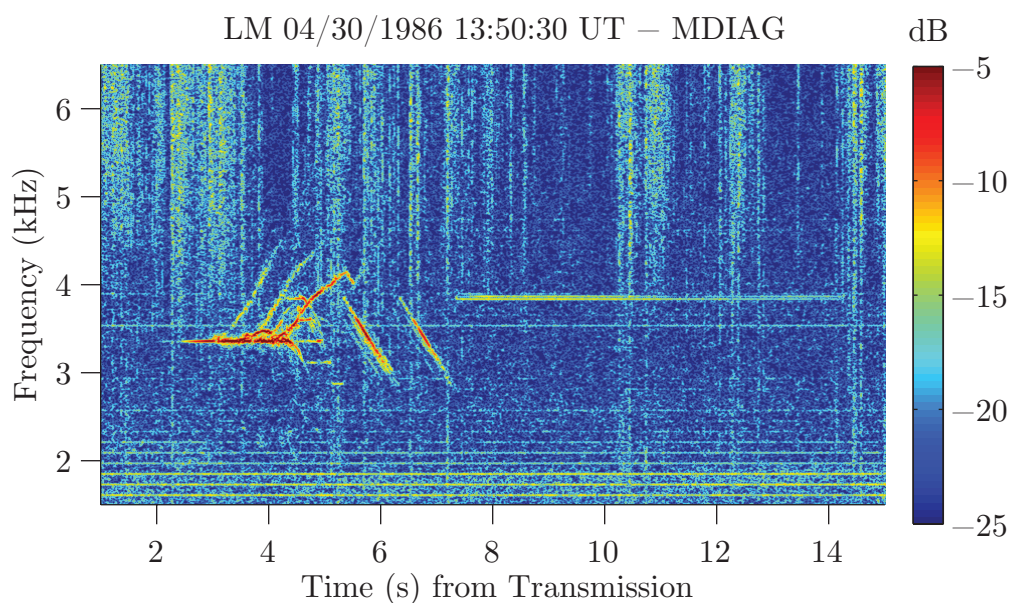


Figure A.5: The transmission elements are all amplified strongly. In particular, the doublets appear to exhibit sidebands and fading.

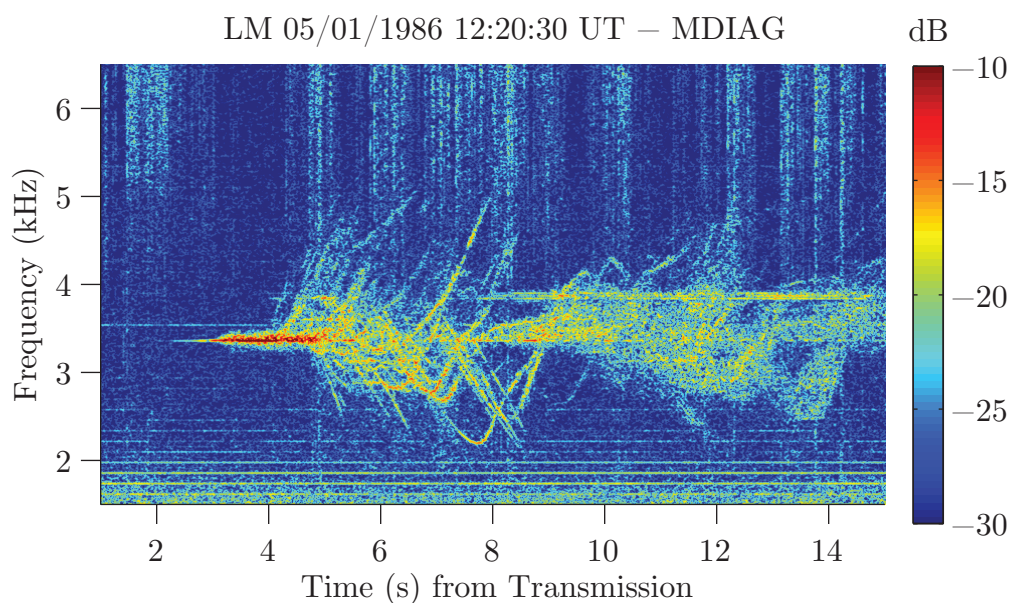


Figure A.6: One hop, three hop, and possibly a fifth hop reception of a transmission that echoed several times. In addition, the triggered emissions are also observed in the later echoes as well.

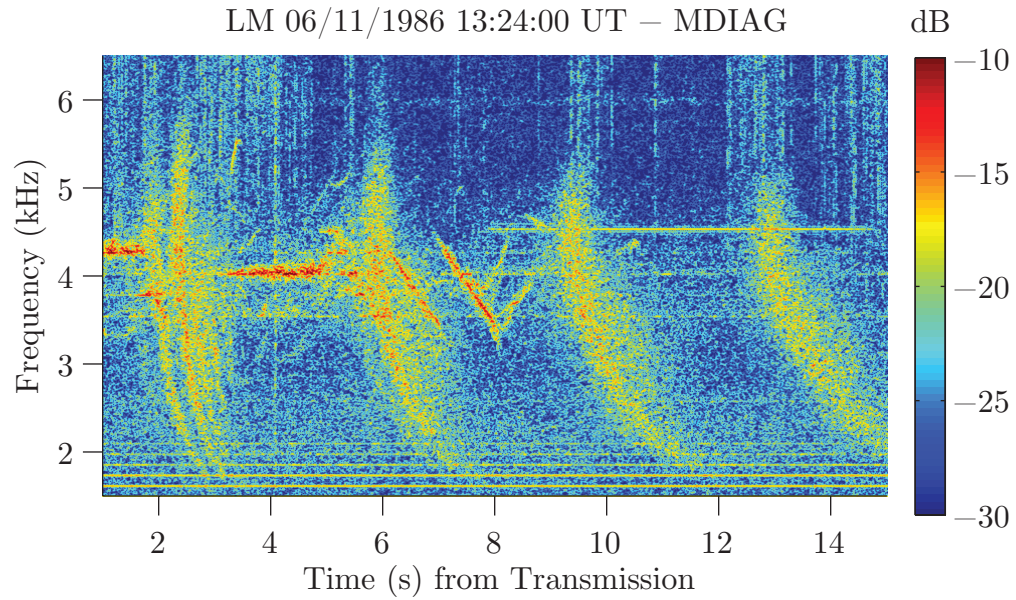


Figure A.7: A reception observed in the presence of a long whistler train.

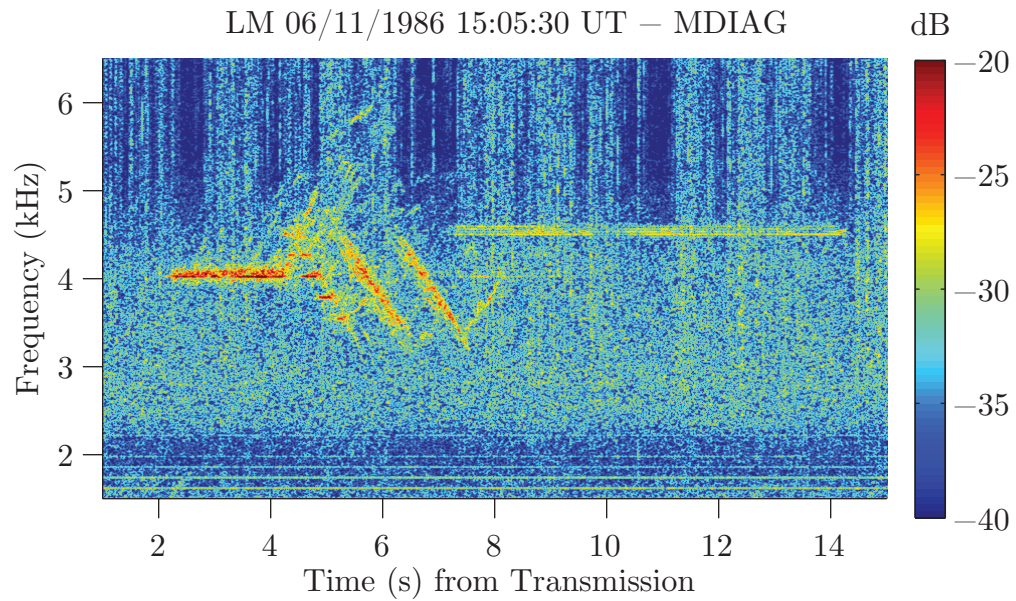


Figure A.8: This reception occurs in the presence of an incoherent, fairly broad band of noise.

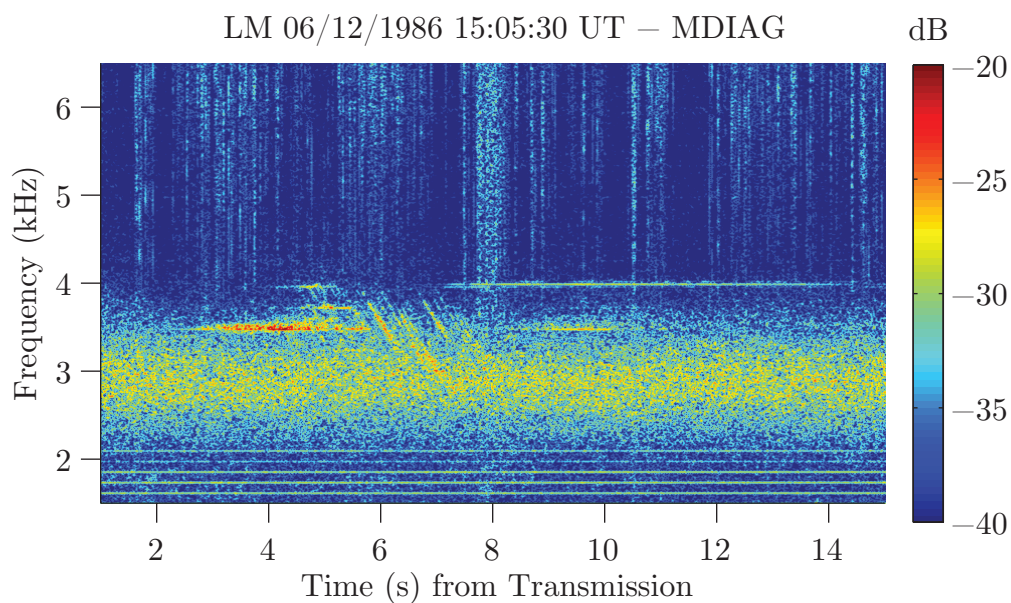


Figure A.9: An example of a common operator frequency selection where the f_{set} is chosen just above the band of chorus.

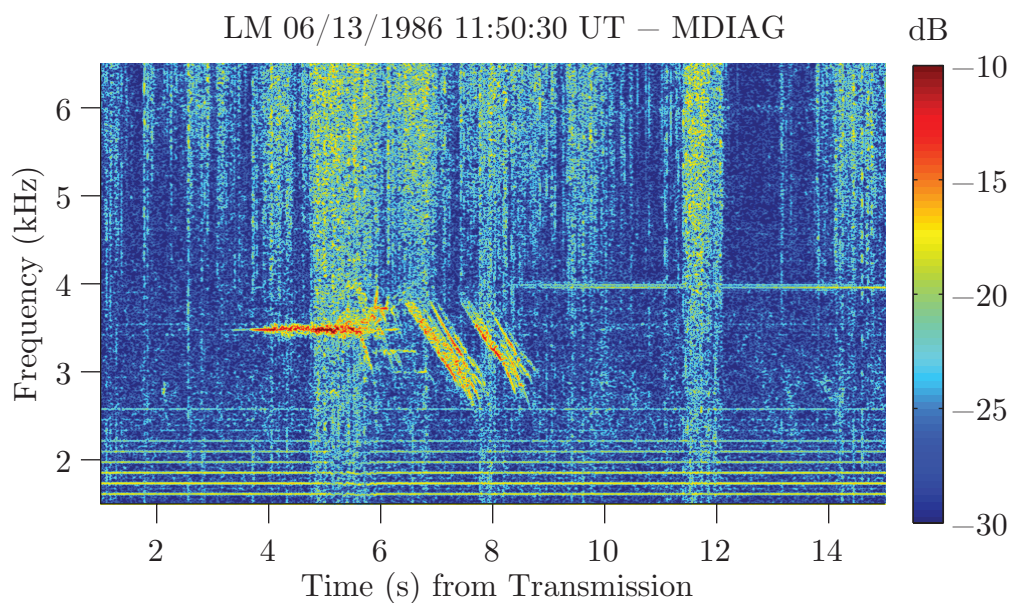


Figure A.10: The transmission propagated along a large number of different paths in this example, where the multipath can be observed with the large number of received ramp elements.

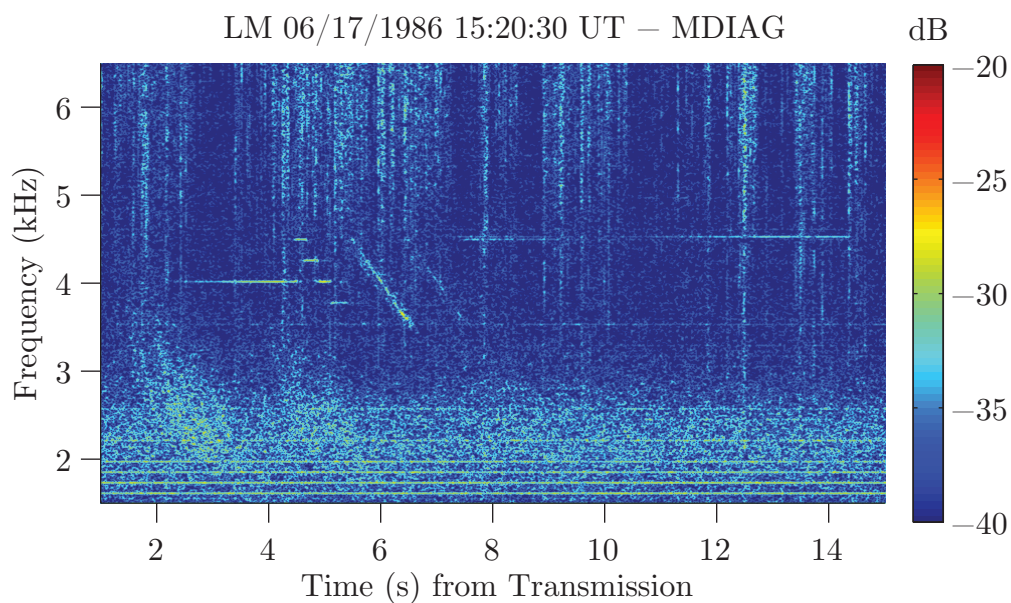


Figure A.11: An unusually quiet reception where the signal is very weakly amplified and only slightly above the noise floor. However, all transmission elements are also present.

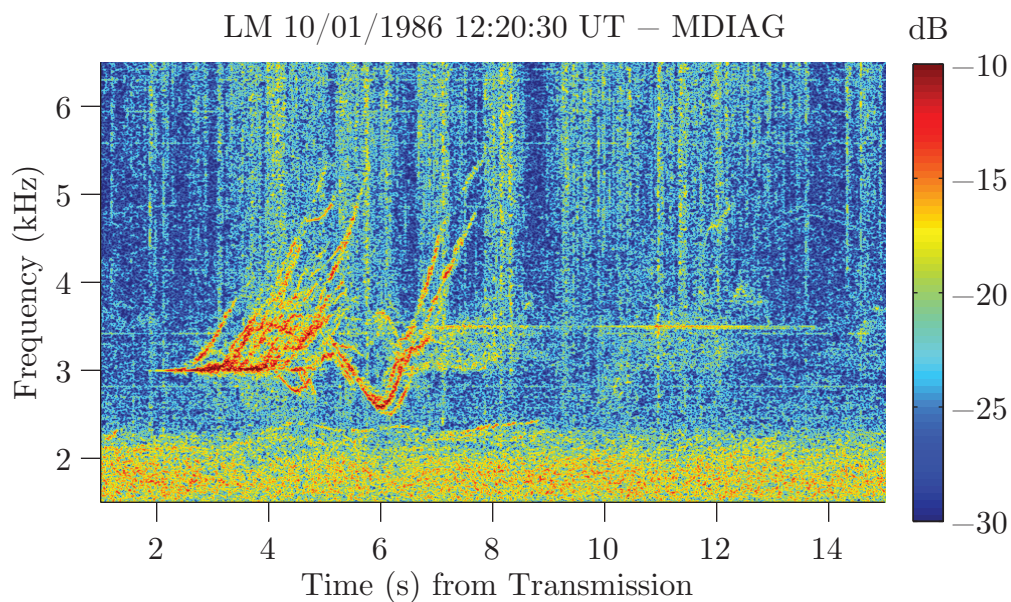


Figure A.12: Another example of an active reception with significant amounts of triggering, with a possible example of a triggered emission entraining into the doublet.

A.2 Staircase Coherence (STACO) Data

The STACO format was a specific format used to study the approximations of discrete staircase tones to a continuous frequency ramp and is the format studied in Chapter 4 and in Chapter 5. Again, while the format is composed of 2 consecutive sets each of rising and falling frequency ramps, each containing five ramp approximations with a frequency sweep rate of ± 1 kHz/s and of a 1-s duration, the focus in this work is on the rising or falling orientation of the ramp allowing us to ignore the approximations. However, as these examples show, the final ramp approximation using 100-ms long staircase tones is not valid and can be observed as distinct tones. Only the middle rising and falling sets of frequency ramps as shown for clarity in observing the various features. And as before, each reception is normalized to the local calibration tone, allowing for comparisons of relative amplitude between receptions.

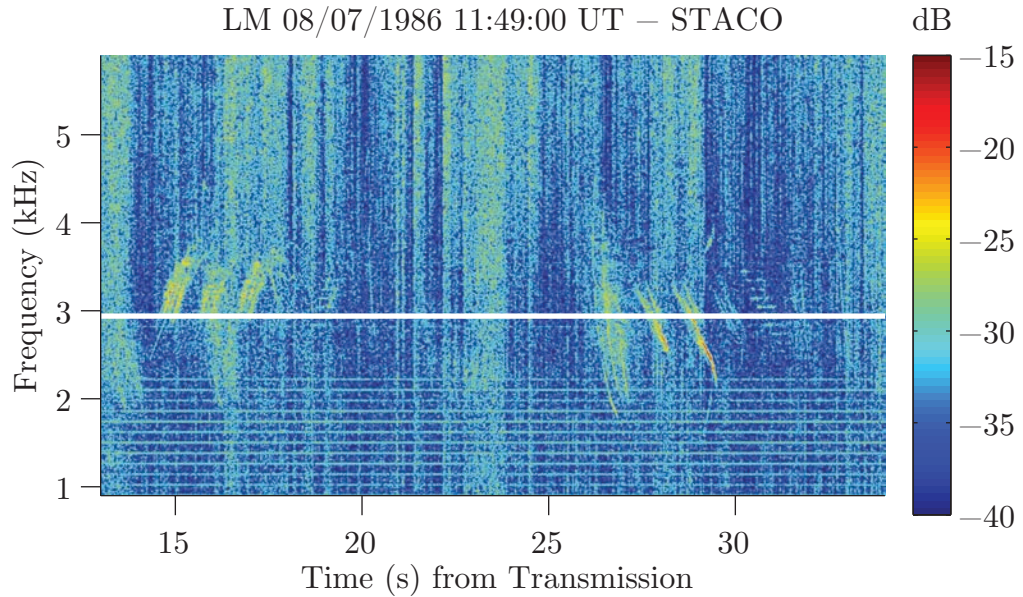


Figure A.13: A fairly typical example where the rising and falling ramps are detected. Some multipath is evident from the additional ramp elements, particularly in the rising ramps, and the 100-ms staircase approximations are rather distinct.

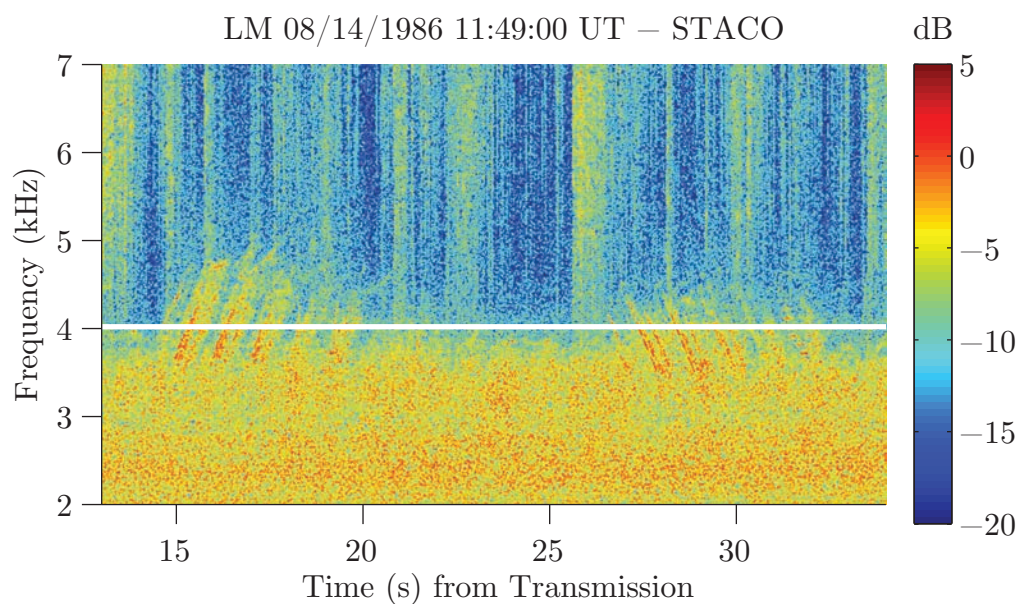


Figure A.14: This STACO reception occurs in the presence of a band of chorus or of incoherent noise and is more incoherent.

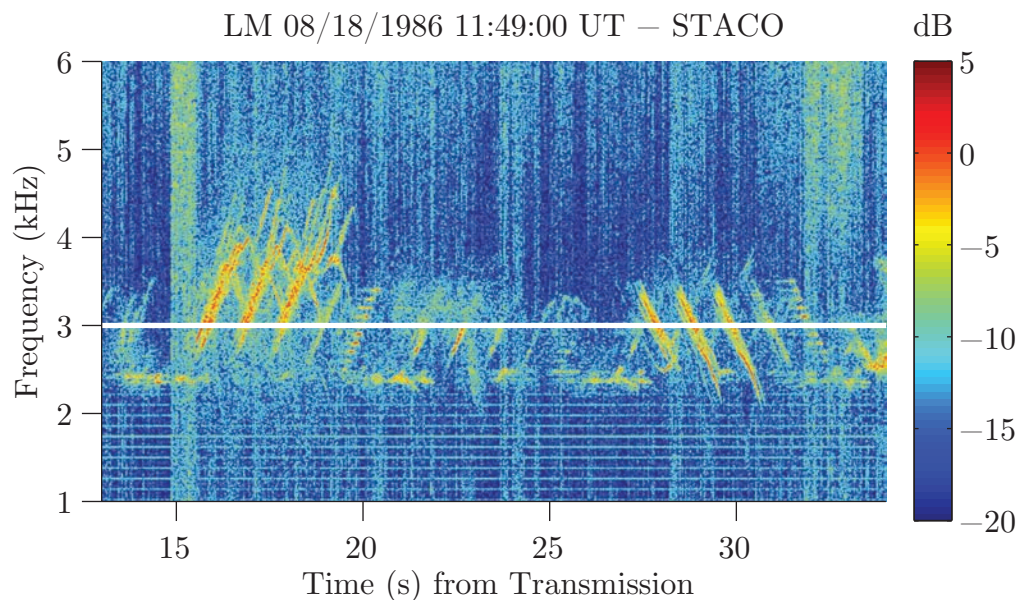


Figure A.15: This STACO reception occurs in the presence of a band of coherent noise, possibly chorus, that exhibit discrete emission elements.

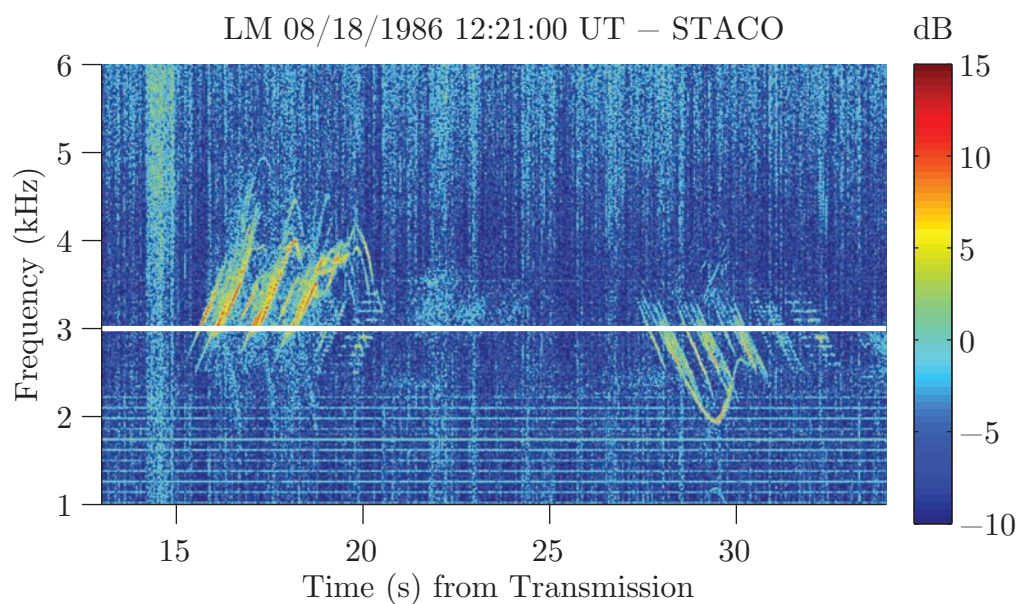


Figure A.16: Here, the rising ramps in the STACO format are amplified more and excite more triggered emissions than the falling ramps.

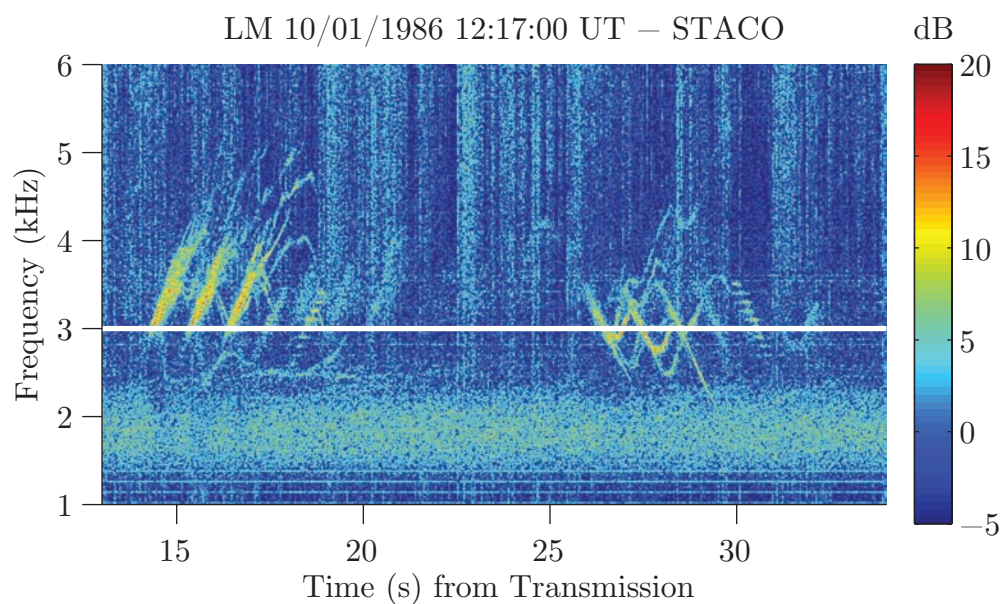


Figure A.17: Another typical example of a STACO reception, with a band of chorus and other emissions present.

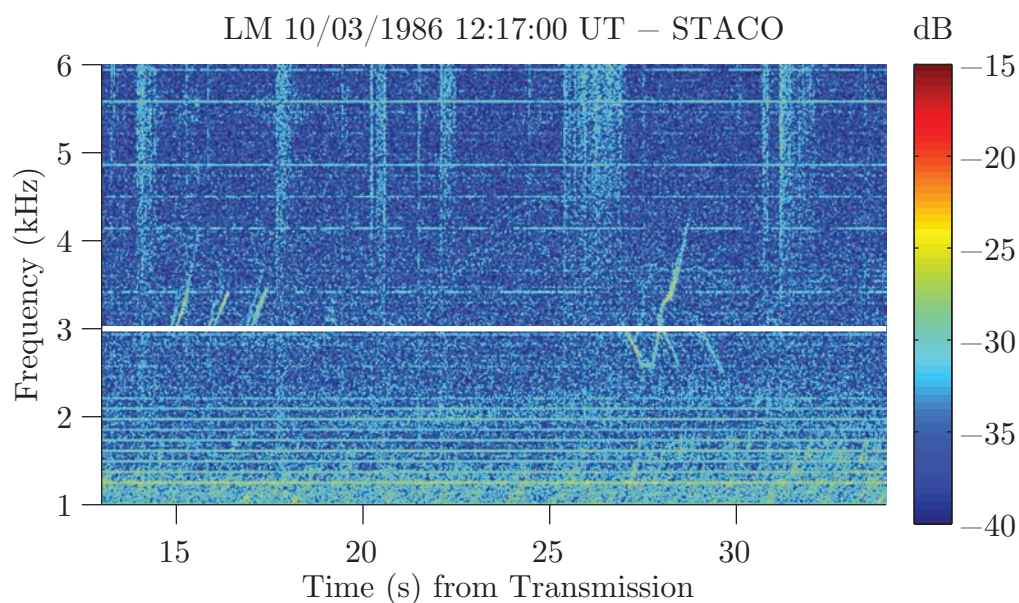


Figure A.18: A weak reception with little amplification of either set of ramps. Only upper frequencies for the rising ramps, and the low frequencies for the falling ramps, are observed.

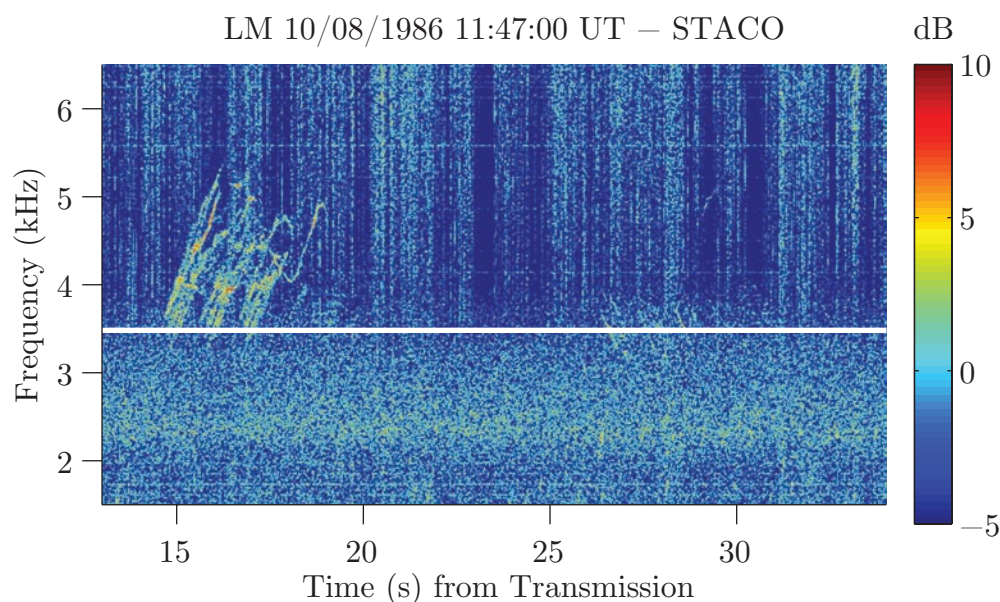


Figure A.19: Not an infinite ratio case, but a reception where the rising ramps are amplified significantly more than the falling ramps.

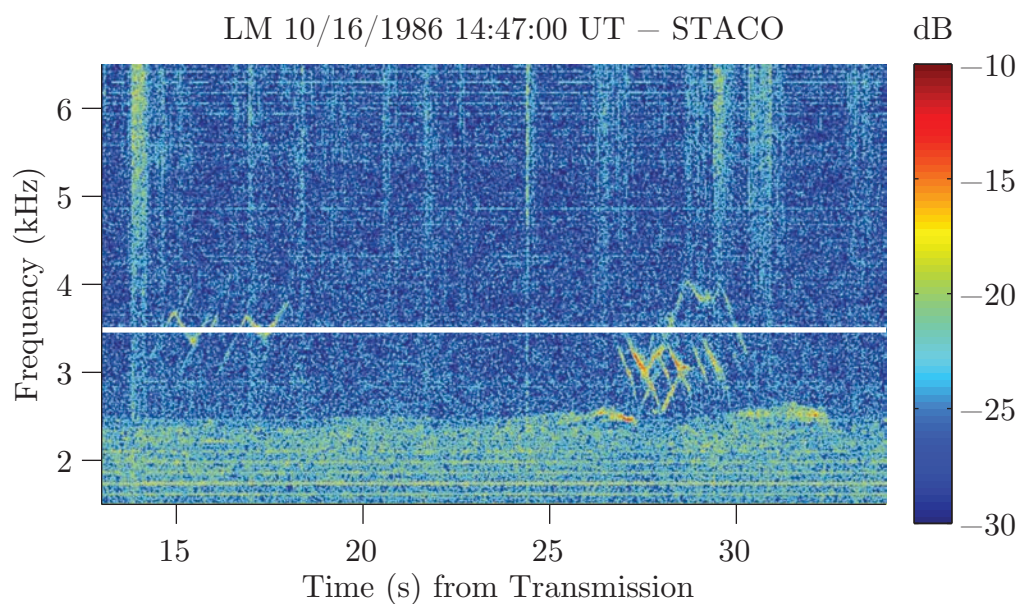


Figure A.20: The falling ramps are amplified more than the rising ramps in this reception. Entrainment is also observed in the triggering from the rising ramps.

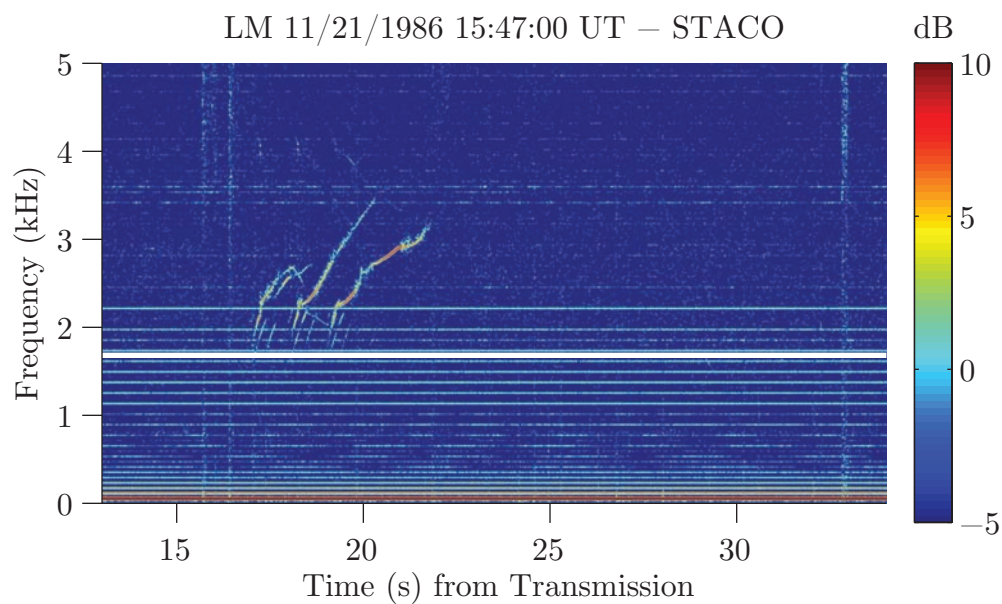


Figure A.21: An infinite ratio example where the falling ramps are not observed at all at the receiver.

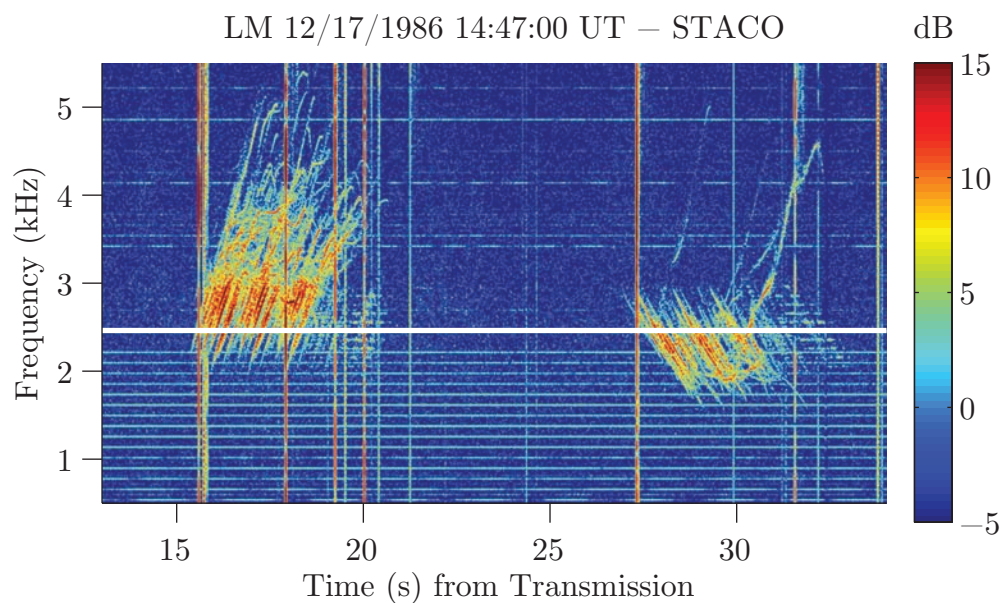


Figure A.22: A particularly active reception example with strong amplification and numerous triggered emissions along with strong multipath effects.

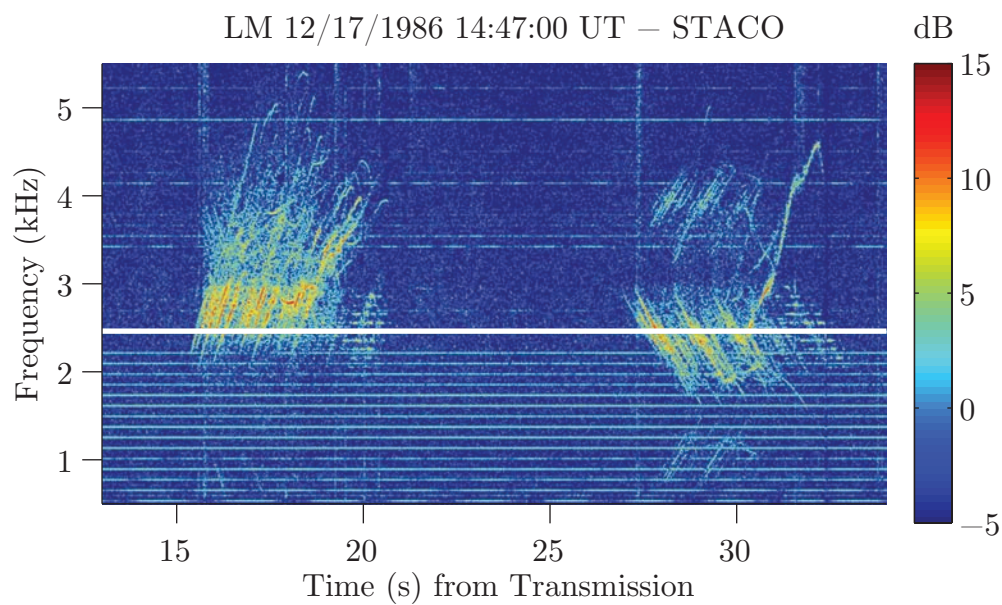


Figure A.23: A cleaned version of Figure A.22 above where the sferics have been removed. This example is included to illustrate some artifacts introduced by the preprocessing.

Appendix B

Spectral Forms of Triggered Emissions

Helliwell [1979] as well as *Helliwell* [1965, Ch. 7] describe the different types of triggered emissions and tend to give hand-drawn examples of their frequency-time format. Here, to provide improved examples of real data, we present several triggered emission examples for each type of triggered emission. The transmission formats shown are all MDIAG transmissions, but as described by Chapter 5, other transmission formats excite similar types of triggered emissions.

B.1 Riser

The riser is a triggered emission that rises in frequency. While it can sometimes terminate with a short change in frequency at the end, we consider those as hook emissions instead.

B.2 Faller

The faller is a triggered emission that falls in frequency. They tend to occur at the termination of the transmitted signal but can trigger during the transmission as well.

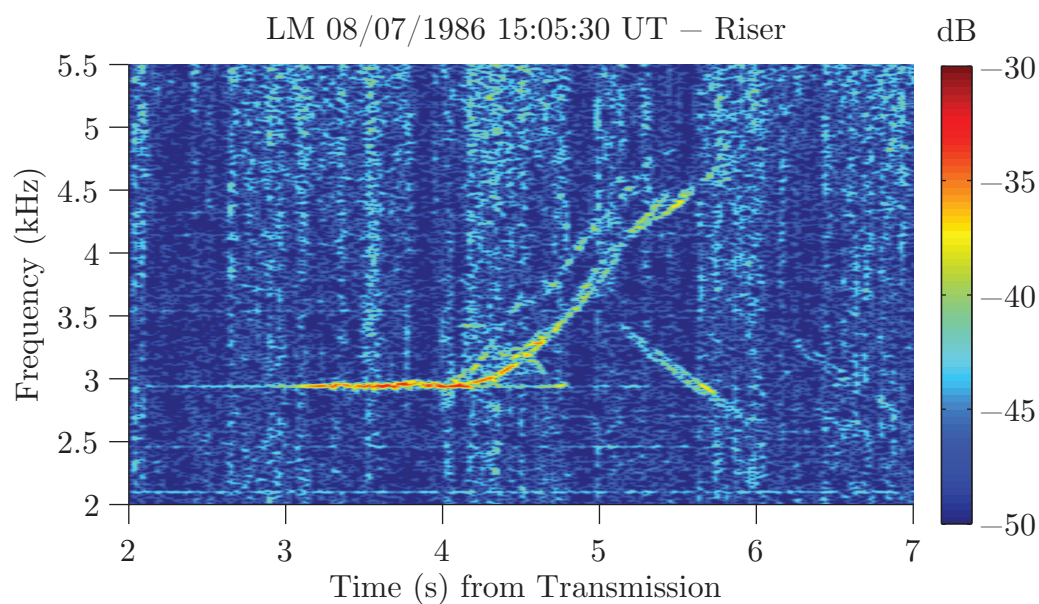


Figure B.1: A rather canonical example of a riser where the triggered emission begins after the transmitted signal saturates and rises in frequency.

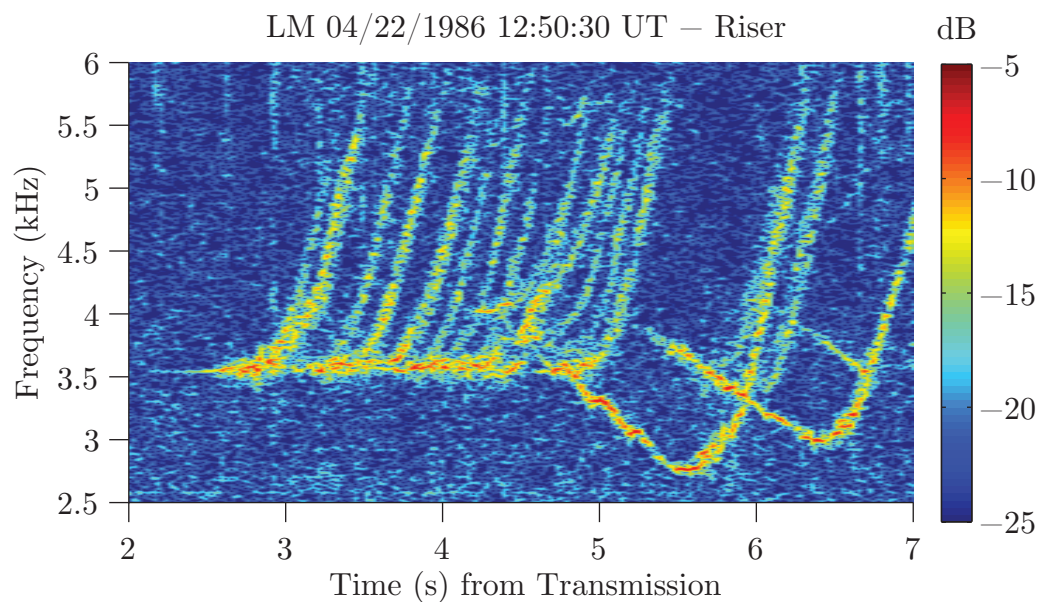


Figure B.2: An example of a train of risers triggered from the MDIAG long tone. Note that within this duration, the emission frequency-time behavior is quite similar.

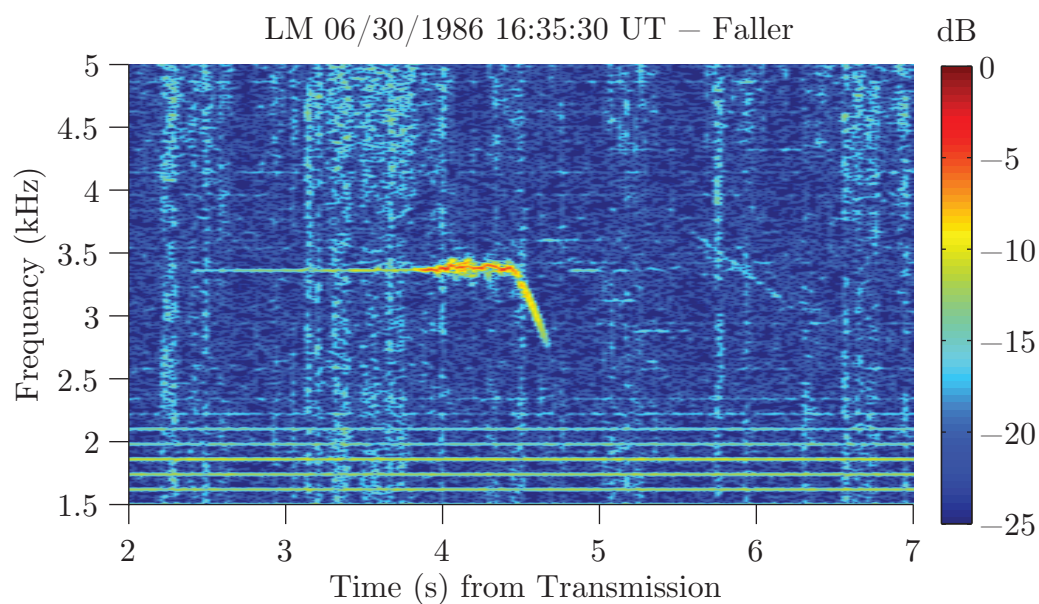


Figure B.3: A rather canonical example of a faller where the triggered emission begins when the transmitted signal terminates and falls in frequency.

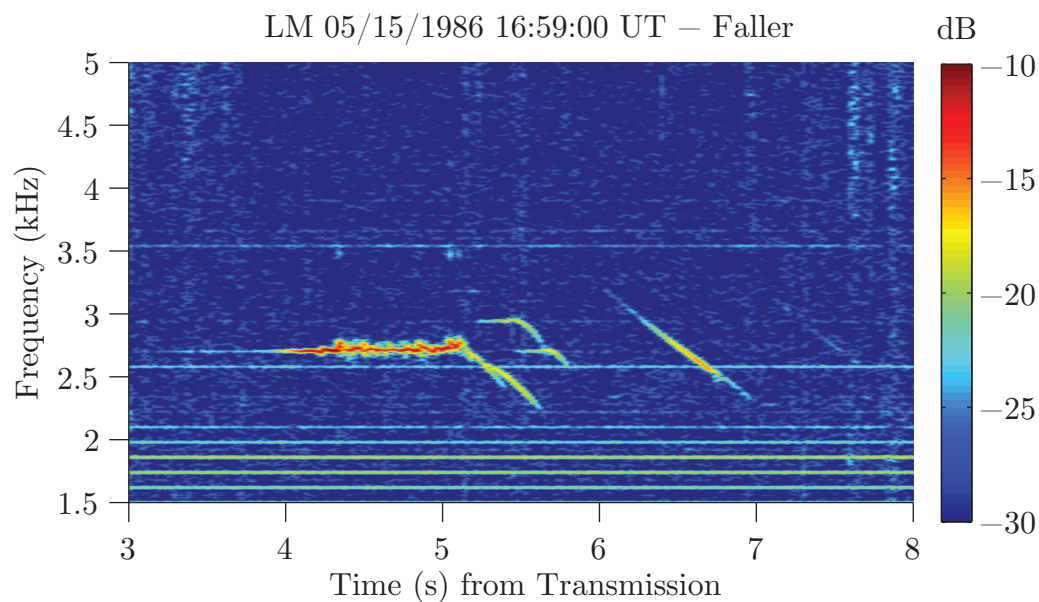


Figure B.4: An example with several fallers, each of which trigger upon the termination of the transmitted tones, here the long tone and the two observed short tones.

B.3 Hooks

A hook is a triggered emission that undergoes at least one change in frequency sweep rate and is classified as a positive or negative hook. Positive hooks begin like a riser, before falling in frequency, while negative hooks begin like a faller before rising in frequency. Hooks exhibit more complex frequency-time structure with some examples undergoing multiple reversals in frequency sweep rate and can persist for a longer duration.

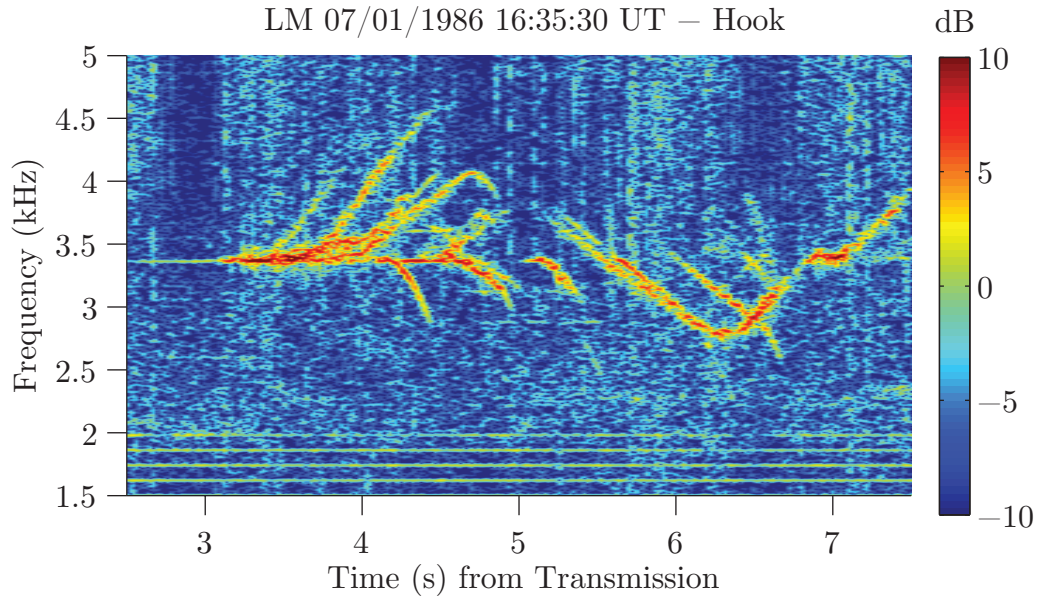


Figure B.5: An example with several hooks, both positive and negative. The positive hook triggers from the long tone by beginning as a riser before falling in frequency around $t = 4.5\text{s}$. The negative hook begins as a faller continuing from the first falling ramp before rising in frequency around $t = 6.4\text{s}$.

B.4 Band-Limited Impulse (BLI)

A less common type of triggered emission is the band-limited impulse, or BLI. This type of triggered emission appears as a brief impulse extending from the transmitted signal in frequency and can trigger additional triggered emissions that then trigger

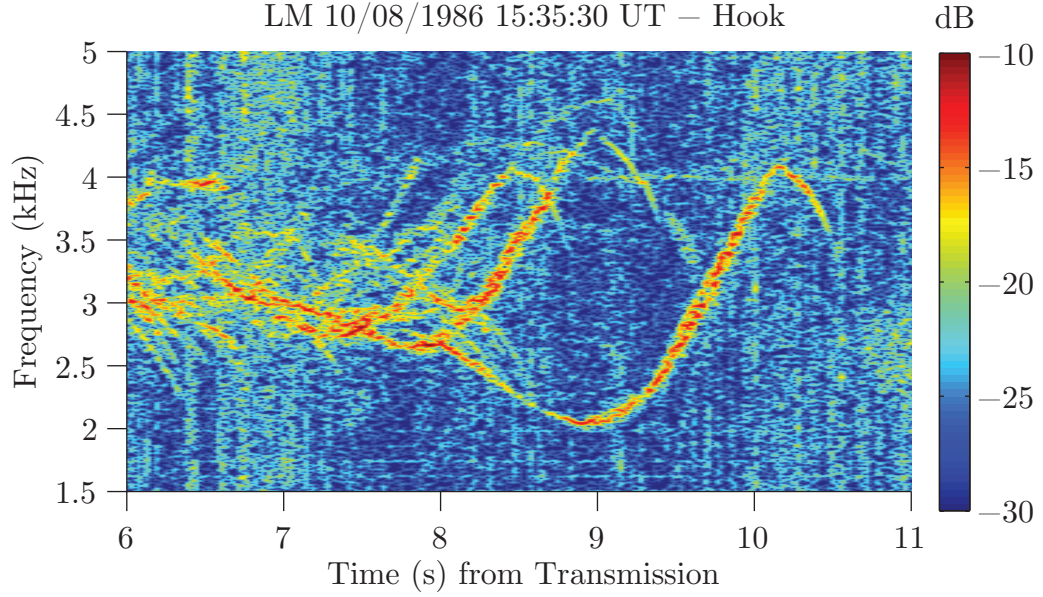


Figure B.6: A dramatic example of the complex behavior of hooks. The negative hook begins around $t = 7s$ as a faller and gradually falls in frequency by ~ 1 kHz. At $t = 9s$, the hook reverses and rises in frequency by ~ 2 kHz, before changing direction again $t = 10.2s$ and falling in frequency.

at an offset initial frequency.

B.5 Early Riser

Early risers are triggered emissions that appear to trigger near or before the occurrence of saturation and tend to rise at a higher frequency sweep rate than later emissions triggered from the same transmission. While it is uncertain whether this is truly another type of triggered emission, early risers do appear to exhibit significantly different frequency-time behavior than other triggered emissions from the same transmission.

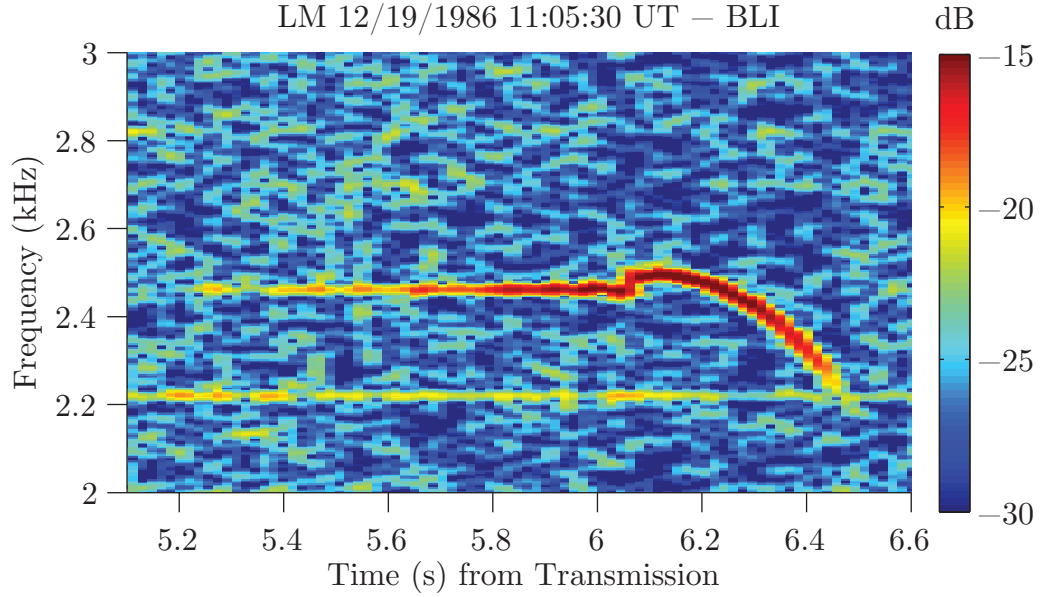


Figure B.7: An example of a BLI and an offset faller. The BLI is the short impulse at about $t = 6.1$ s, resulting in an offset faller triggering at the upper frequency of the BLI.

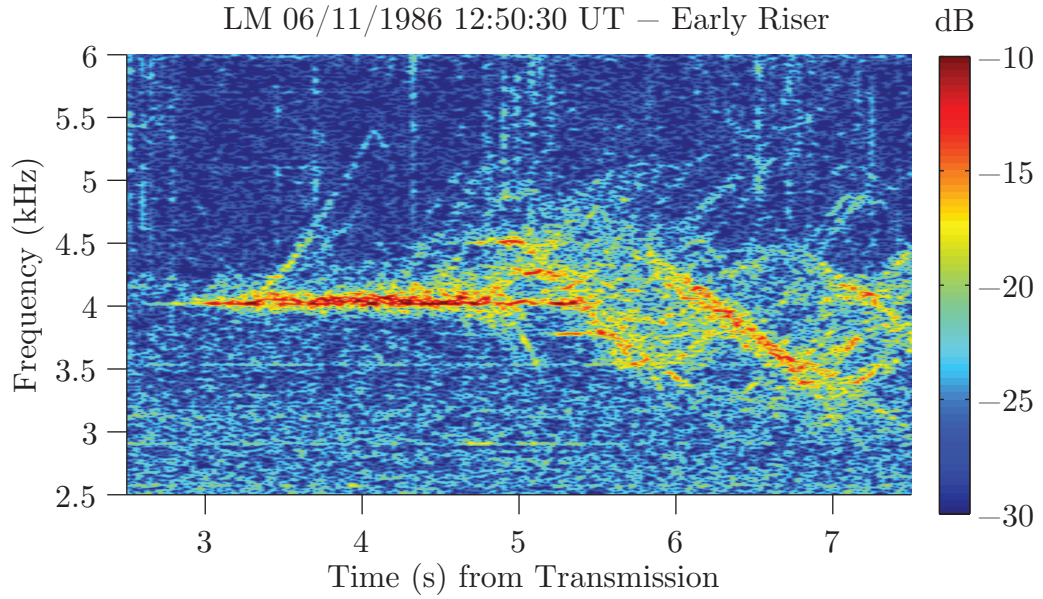


Figure B.8: A possible example of an early riser event, where a single triggered emission begins at about $t = 3.2$ in advance of any other triggered emissions.

Bibliography

- Angerami, J. J. (1970), Whistler Duct Properties Deduced from VLF Observations Made with the Ogo 3 Satellite near the Magnetic Equator, *Journal of Geophysical Research*, *75*, 6115–6135, doi:10.1029/JA075i031p06115.
- Baker, D. N., S. G. Kanekal, V. C. Hoxie, M. G. Henderson, X. Li, H. E. Spence, S. R. Elkington, R. H. W. Friedel, J. Goldstein, M. K. Hudson, G. D. Reeves, R. M. Thorne, C. A. Kletzing, and S. G. Claudepierre (2013), A Long-Lived Relativistic Electron Storage Ring Embedded in Earths Outer Van Allen Belt, *Science*, *340*(6129), 186–190, doi:10.1126/science.1233518.
- Bell, T. F., and U. S. Inan (1981), Transient nonlinear pitch angle scattering of energetic electrons by coherent VLF wave packets in the magnetosphere, *Journal of Geophysical Research*, *86*, 9047–9063, doi:10.1029/JA086iA11p09047.
- Bell, T. F., U. S. Inan, R. A. Helliwell, and J. D. Scudder (2000), Simultaneous triggered VLF emissions and energetic electron distributions observed on POLAR with PWI and HYDRA, *Geophysical Research Letters*, *27*(2), 165–168, doi:10.1029/1999GL003673.
- Bell, T. F., U. S. Inan, N. Haque, and J. S. Pickett (2009), Source regions of banded chorus, *Geophysical Research Letters*, *36*, 11,101, doi:10.1029/2009GL037629.
- Bittencourt, J. A. (2013), *Fundamentals of Plasma Physics*, Springer New York.
- Brinca, A. L. (1972), Whistler side-band growth due to nonlinear wave-particle interaction, *Journal of Geophysical Research*, *77*(19), 3508–3523, doi:10.1029/JA077i019p03508.

- Burtis, W. J., and R. A. Helliwell (1975), Magnetospheric chorus - Amplitude and growth rate, *Journal of Geophysical Research*, *80*, 3265–3270, doi:10.1029/JA080i022p03265.
- Burtis, W. J., and R. A. Helliwell (1976), Magnetospheric chorus - Occurrence patterns and normalized frequency, *Planetary and Space Science*, *24*, 1007–1024, doi:10.1016/0032-0633(76)90119-7.
- Carlson, C. R., R. A. Helliwell, and D. L. Carpenter (1985a), Variable frequency VLF signals in the magnetosphere Associated phenomena and plasma diagnostics, *Journal of Geophysical Research*, *90*, 1507–1521, doi:10.1029/JA090iA02p01507.
- Carlson, C. R., R. A. Helliwell, and D. L. Carpenter (1985b), Correction to “Variable Frequency VLF Signals in the Magnetosphere: Associated Phenomena and Plasma Diagnostics”, *Journal of Geophysical Research*, *90*, 6689, doi:10.1029/JA090iA07p06689.
- Carlson, C. R., R. A. Helliwell, and U. S. Inan (1990), Space-time evolution of whistler mode wavegrowth in the magnetosphere, *Journal of Geophysical Research*, *95*, 15,073–15,089, doi:10.1029/JA095iA09p15073.
- Carpenter, D. L. (1963), Whistler Evidence of a ‘Knee’ in the Magnetospheric Ionization Density Profile, *Journal of Geophysical Research*, *68*, 1675–1682, doi:10.1029/JZ068i006p01675.
- Carpenter, D. L. (1966), Whistler Studies of the Plasmapause in the Magnetosphere, 1, Temporal Variations in the Position of the Knee and Some Evidence on Plasma Motions near the Knee, *Journal of Geophysical Research*, *71*, 693.
- Carpenter, D. L. (1968), Ducted Whistler-Mode Propagation in the Magnetosphere: A Half-Gyrofrequency Upper Intensity Cutoff and Some Associated Wave Growth Phenomena, *Journal of Geophysical Research*, *73*, 2919, doi:10.1029/JA073i009p02919.

- Carpenter, D. L. (1978), Whistlers and VLF noises propagating just outside the plasmopause, *Journal of Geophysical Research*, *83*, 45–57, doi:10.1029/JA083iA01p00045.
- Carpenter, D. L. (1988), Remote sensing of the magnetospheric plasma by means of whistler mode signals, *Reviews of Geophysics*, *26*, 535–549, doi:10.1029/RG026i003p00535.
- Carpenter, D. L. (2014), The Early History of Very Low Frequency (VLF) Radio Research at Stanford.
- Carpenter, D. L., and Z. T. Bao (1983), Occurrence properties of ducted whistler-mode signals from the new VLF transmitter at Siple Station, Antarctica, *Journal of Geophysical Research*, *88*, 7051–7057, doi:10.1029/JA088iA09p07051.
- Carpenter, D. L., and S. Lasch (1969), An Effect of a Transmitter Frequency Increase on the Occurrence of VLF Noise Triggered near $L = 3$ in the Magnetosphere, *Journal of Geophysical Research*, *74*, 1859, doi:10.1029/JA074i007p01859.
- Carpenter, D. L., and T. R. Miller (1976), Ducted magnetospheric propagation of signals from the Siple, Antarctica, VLF transmitter, *Journal of Geophysical Research*, *81*, 2692–2700, doi:10.1029/JA081i016p02692.
- Carpenter, D. L., and T. R. Miller (1983), Rare ground-based observations of Siple VLF transmitter signals outside the plasmopause, *Journal of Geophysical Research*, *88*, 10,227–10,232, doi:10.1029/JA088iA12p10227.
- Carpenter, D. L., and R. E. Orville (1989), The excitation of active whistler mode signal paths in the magnetosphere by lightning - Two case studies, *Journal of Geophysical Research*, *94*, 8886–8894, doi:10.1029/JA094iA07p08886.
- Carpenter, D. L., and D. M. Sulic (1988), Ducted whistler propagation outside the plasmopause, *Journal of Geophysical Research*, *93*, 9731–9742, doi:10.1029/JA093iA09p09731.

- Carpenter, D. L., K. Stone, and S. Lasch (1969), A Case of Artificial Triggering of VLF Magnetospheric Noise during the Drift of a Whistler Duct across Magnetic Shells, *Journal of Geophysical Research*, *74*, 1848, doi:10.1029/JA074i007p01848.
- Carpenter, D. L., T. F. Bell, T. R. Miller, and R. R. Anderson (1981), A comparison of equatorial electron densities measured by whistlers and by a satellite radio technique, *Geophysical Research Letters*, *8*, 1107–1110, doi:10.1029/GL008i010p01107.
- Carpenter, D. L., T. F. Bell, and A. J. Smith (1988), The Siple VLF transmitter as a multi-frequency probe of the earth-ionosphere waveguide, *Journal of Atmospheric and Terrestrial Physics*, *50*, 105–109.
- Carpenter, D. L., V. S. Sonwalkar, R. A. Helliwell, M. Walt, U. S. Inan, M. Ikeda, and D. L. Caudle (1997), Probing properties of the magnetospheric hot plasma distribution by whistler mode wave injection at multiple frequencies: Evidence of spatial as well as temporal wave growth, *Journal of Geophysical Research*, *102*, 14,355–14,362, doi:10.1029/96JA03046.
- Chang, C.-C., and C.-J. Lin (2011), {LIBSVM}: A library for support vector machines, *ACM Transactions on Intelligent Systems and Technology*, *2*(3), 27:1—27:27.
- Chang, D. C. D., and R. A. Helliwell (1979), Emission triggering in the magnetosphere by controlled interruption of coherent VLF signals, *Journal of Geophysical Research*, *84*, 7170–7176, doi:10.1029/JA084iA12p07170.
- Chang, D. C. D., R. A. Helliwell, and T. F. Bell (1980), Side-band mutual interactions in the magnetosphere, *Journal of Geophysical Research*, *85*, 1703–1712, doi:10.1029/JA085iA04p01703.
- Chang, H. C., U. S. Inan, and T. F. Bell (1983), Energetic electron precipitation due to gyroresonant interactions in the magnetosphere involving coherent VLF waves with slowly varying frequency, *Journal of Geophysical Research*, *88*, 7037–7050, doi:10.1029/JA088iA09p07037.

- Chrissan, D. A., and A. C. Fraser-Smith (1996), Seasonal variations of globally measured ELF/VLF radio noise, *Radio Science*, *31*(5), 1141–1152, doi:10.1029/96RS01930.
- Cohen, M. B., and M. Golkowski (2013), 100 Days of ELF/VLF Generation via HF Heating with HAARP, *Journal of Geophysical Research: Space Physics*, pp. n/a—n/a, doi:10.1002/jgra.50558.
- Cohen, M. B., U. S. Inan, M. Golkowski, and M. J. McCarrick (2010a), ELF/VLF wave generation via ionospheric HF heating: Experimental comparison of amplitude modulation, beam painting, and geometric modulation, *Journal of Geophysical Research (Space Physics)*, *115*, 2302, doi:10.1029/2009JA014410.
- Cohen, M. B., U. S. Inan, and E. W. Paschal (2010b), Sensitive Broadband ELF/VLF Radio Reception With the AWESOME Instrument, *IEEE Transactions on Geoscience and Remote Sensing*, *48*, 3–17, doi:10.1109/TGRS.2009.2028334.
- Cortes, C., and V. Vapnik (1995), Support-vector networks, *Machine learning*, *20*(3), 273–297.
- Cully, C. M., V. Angelopoulos, U. Auster, J. W. Bonnell, and O. Le Contel (2011), Observational evidence of the generation mechanism for rising-tone chorus, *Geophysical Research Letters*, *38*(1), n/a—n/a, doi:10.1029/2010GL045793.
- Das, A. C. (1968), A mechanism for VLF emissions, *Journal of Geophysical Research*, *73*(23), 7457–7471, doi:10.1029/JA073i023p07457.
- Dowden, R. L., A. D. McKay, L. E. S. Amon, H. C. Koons, and M. H. Dazey (1978), Linear and nonlinear amplification in the magnetosphere during a 6.6-kHz transmission, *Journal of Geophysical Research: Space Physics*, *83*(A1), 169–181, doi:10.1029/JA083iA01p00169.
- Dysthe, K. B. (1971), Some studies of triggered whistler emissions, *Journal of Geophysical Research*, *76*(28), 6915–6931, doi:10.1029/JA076i028p06915.

- Edgar, B. C. (1976), The upper- and lower-frequency cutoffs of magnetospherically reflected whistlers, *Journal of Geophysical Research*, *81*, 205–211, doi:10.1029/JA081i001p00205.
- Filbet, F., and E. Sonnendrücker (2003), Comparison of eulerian Vlasov solvers, *Computer Physics Communications*, *150*(3), 247–266.
- Gail, W. B., and D. L. Carpenter (1984), Whistler induced suppression of VLF noise, *Journal of Geophysical Research*, *89*, 1015–1022, doi:10.1029/JA089iA02p01015.
- Gavrishchaka, V. V., and S. B. Ganguli (2001), Support vector machine as an efficient tool for high-dimensional data processing: Application to substorm forecasting, *Journal of Geophysical Research: Space Physics*, *106*(A12), 29,911–29,914, doi:10.1029/2001JA900118.
- Gibby, A. R. (2008), Saturation Effects in VLF Triggered Emissions, Ph.d. dissertation, Stanford University.
- Gibby, A. R., U. S. Inan, and T. F. Bell (2008), Saturation effects in the VLF-triggered emission process, *Journal of Geophysical Research (Space Physics)*, *113*(A12), 11,215, doi:10.1029/2008JA013233.
- Golkowski, M. (2009), Magnetospheric Wave Injection by Modulated HF Heating of the Auroral Electrojet, Ph.d. dissertation, Stanford University.
- Golkowski, M., U. S. Inan, A. R. Gibby, and M. B. Cohen (2008), Magnetospheric amplification and emission triggering by ELF/VLF waves injected by the 3.6 MW HAARP ionospheric heater, *Journal of Geophysical Research (Space Physics)*, *113*(A12), 10,201, doi:10.1029/2008JA013157.
- Golkowski, M., U. S. Inan, M. B. Cohen, and A. R. Gibby (2010), Amplitude and phase of nonlinear magnetospheric wave growth excited by the HAARP HF heater, *Journal of Geophysical Research (Space Physics)*, *115*(A14), doi:10.1029/2009JA014610.

- Golkowski, M., M. B. Cohen, D. L. Carpenter, and U. S. Inan (2011), On the occurrence of ground observations of ELF/VLF magnetospheric amplification induced by the HAARP facility, *Journal of Geophysical Research*, *116*, doi:10.1029/2010JA016261.
- Graf, K. L., N. G. Lehtinen, M. Spasojevic, M. B. Cohen, R. A. Marshall, and U. S. Inan (2013), Analysis of experimentally validated trans-ionospheric attenuation estimates of VLF signals, *Journal of Geophysical Research: Space Physics*, pp. n/a – n/a, doi:10.1002/jgra.50228.
- Haque, N., U. S. Inan, T. F. Bell, J. S. Pickett, J.-G. Trotignon, and G. Facsko (2011), Cluster Observations of Whistler Mode Ducts and Banded Chorus, *Geophysical Research Letters*, doi:10.1029/2011GL049112.
- Harid, V. (2015), Coherent Interactions Between Whistler Mode Waves and Energetic Electrons in the Earth's Radiation Belts, Ph.d. dissertation, Stanford University.
- Harid, V., M. Golkowski, T. F. Bell, J. D. Li, and U. S. Inan (2014a), Finite Difference Modeling of Coherent Wave Amplification in the Earth's Radiation Belts, *Geophysical Research Letters*, pp. n/a—n/a, doi:10.1002/2014GL061787.
- Harid, V., M. Golkowski, T. F. Bell, and U. S. Inan (2014b), Theoretical and numerical analysis of radiation belt electron precipitation by coherent whistler mode waves, *Journal of Geophysical Research: Space Physics*, *119*(6), 4370–4388, doi: 10.1002/2014JA019809.
- Harriman, S. K., E. W. Paschal, and U. S. Inan (2010), Magnetic Sensor Design for Femtotesla Low-Frequency Signals, *IEEE Transactions on Geoscience and Remote Sensing*, *48*, 396–402, doi:10.1109/TGRS.2009.2027694.
- Helliwell, R. A. (1962), Artificially stimulated VLF electromagnetic radiation from the earth's atmosphere, *URSI/IRE Meeting*.
- Helliwell, R. A. (1965), *Whistlers and related ionospheric phenomena*, Stanford University Press.

- Helliwell, R. A. (1967), A Theory of Discrete VLF Emissions from the Magnetosphere, *Journal of Geophysical Research*, *72*, 4773, doi:10.1029/JZ072i019p04773.
- Helliwell, R. A. (1970), The upper atmosphere as seen from Antarctica, *Bulletin of the Atomic Scientists*, *26*(10), 55–61.
- Helliwell, R. A. (1979), Siple station experiments on wave-particle interactions in the magnetosphere, in *Wave instabilities in space plasmas; Proceedings of the Symposium, Helsinki, Finland, July 31-August 8, 1978. (A80-21196 07-46) Dordrecht, D. Reidel Publishing Co., 1979, p. 191-203.*, edited by P. J. Palmadesso and K. Papadopoulos, pp. 191–203.
- Helliwell, R. A. (1983), Controlled stimulation of VLF emissions from Siple Station, Antarctica, *Radio Science*, *18*, 801–814, doi:10.1029/RS018i006p00801.
- Helliwell, R. A. (1988a), VLF wave stimulation experiments in the magnetosphere from Siple Station, Antarctica, *Reviews of Geophysics*, *26*, 551–578, doi:10.1029/RG026i003p00551.
- Helliwell, R. A. (1988b), VLF wave-injection experiments from Siple Station, Antarctica, *Advances in Space Research*, *8*, 279–289, doi:10.1016/0273-1177(88)90373-0.
- Helliwell, R. A. (2000), Triggering of whistler mode emissions by the band-limited impulse(BLI) associated with amplified Vlf signals from Siple Station, Antarctica, *Geophysical Research Letters*, *27*, 1455, doi:10.1029/1999GL003676.
- Helliwell, R. A., and D. L. Carpenter (1961), Whislter-West IGY-IGC Synoptic Program, *Tech. rep.*, Stanford Electronics Laboratory, Stanford University, Stanford.
- Helliwell, R. A., and D. L. Carpenter (1962), Whistler-west results from the IGY-IGC-59 synoptic program, *Trans. AGU*, *43*, 125.
- Helliwell, R. A., and T. L. Crystal (1973), A Feedback Model of Cyclotron Interaction between Whistler-Mode Waves and Energetic Electrons in the Magnetosphere, *Journal of Geophysical Research*, *78*, 7357–7371, doi:10.1029/JA078i031p07357.

- Helliwell, R. A., and E. Gehrels (1958), Observations of magneto-ionic duct propagation using man-made signals of very low frequency.
- Helliwell, R. A., and J. P. Katsufakis (1974), VLF Wave Injection into the Magnetosphere from Siple Station, Antarctica, *J. Geophys. Res.*, *79*(16), 2511–2518, doi:10.1029/JA079i016p02511.
- Helliwell, R. A., and J. P. Katsufakis (1978), *Controlled wave-particle interaction experiments, Paper 5 in Upper Atmosphere Research in Antarctica, Antarctic Research Series*, vol. 29, pp. 100–129.
- Helliwell, R. A., J. P. Katsufakis, M. L. Trimpi, and N. M. Brice (1964), Artificially Stimulated Very Low Frequency Radiation from the Ionosphere, *Journal of Geophysical Research*, *69*, 2391–2394, doi:10.1029/JZ069i011p02391.
- Helliwell, R. A., D. L. Carpenter, and T. R. Miller (1980), Power threshold for growth of coherent VLF signals in the magnetosphere, *Journal of Geophysical Research*, *85*, 3360–3366, doi:10.1029/JA085iA07p03360.
- Helliwell, R. A., U. S. Inan, J. P. Katsufakis, and D. L. Carpenter (1986), Beat excitation of whistler mode sidebands using the Siple VLF transmitter, *Journal of Geophysical Research*, *91*, 143–153, doi:10.1029/JA091iA01p00143.
- Helliwell, R. A., T. A. Mielke, and U. S. Inan (1990), Rapid whistler-mode wave growth resulting from frequency-time curvature, *Geophysical Research Letters*, *17*, 599–602, doi:10.1029/GL017i005p00599.
- Hikishima, M., and Y. Omura (2012), Particle simulations of whistler-mode rising-tone emissions triggered by waves with different amplitudes, *Journal of Geophysical Research: Space Physics*, *117*(A4), n/a—n/a, doi:10.1029/2011JA017428.
- Hikishima, M., Y. Omura, and D. Summers (2010), Self-consistent particle simulation of whistler mode triggered emissions, *Journal of Geophysical Research: Space Physics*, *115*(A12), n/a—n/a, doi:10.1029/2010JA015860.

- Ho, D. (1973), Interaction between Whistlers and Quasi-Periodic VLF Emissions, *Journal of Geophysical Research*, *78*, 7347–7356, doi:10.1029/JA078i031p07347.
- Imhof, W. L., R. R. Anderson, J. B. Reagan, and E. E. Gaines (1981), The significance of VLF transmitters in the precipitation of inner belt electrons, *Journal of Geophysical Research: Space Physics*, *86*(A13), 11,225–11,234, doi:10.1029/JA086iA13p11225.
- Imhof, W. L., J. B. Reagan, H. D. Voss, E. E. Gaines, D. W. Datlowe, J. Mobilia, R. A. Helliwell, U. S. Inan, J. P. Katsufakis, and R. G. Joiner (1983a), Direct observation of radiation belt electrons precipitated by the controlled injection of VLF signals from a ground-based transmitter, *Geophysical Research Letters*, *10*, 361–364, doi:10.1029/GL010i004p00361.
- Imhof, W. L., J. B. Reagan, H. D. Voss, E. E. Gaines, D. W. Datlowe, J. Mobilia, R. A. Helliwell, U. S. Inan, J. P. Katsufakis, and R. G. Joiner (1983b), The modulated precipitation of radiation belt electrons by controlled signals from VLF transmitters, *Geophysical Research Letters*, *10*, 615–618, doi:10.1029/GL010i008p00615.
- Imhof, W. L., E. E. Gaines, H. D. Voss, J. B. Reagan, D. W. Datlowe, J. Mobilia, R. A. Helliwell, U. S. Inan, J. P. Katsufakis, and R. G. Joiner (1985), Results from the SEEP active space plasma experiment - Effects on the ionosphere, *Radio Science*, *20*, 511–518, doi:10.1029/RS020i003p00511.
- Inan, U. S., and T. F. Bell (1977), The plasmopause as a VLF wave guide, *Journal of Geophysical Research*, *82*, 2819–2827, doi:10.1029/JA082i019p02819.
- Inan, U. S., T. F. Bell, and R. R. Anderson (1977a), Cold plasma diagnostics using satellite measurements of VLF signals from ground transmitters, *Journal of Geophysical Research*, *82*, 1167–1176, doi:10.1029/JA082i007p01167.
- Inan, U. S., T. F. Bell, D. L. Carpenter, and R. R. Anderson (1977b), Explorer 45 and Imp 6 observations in the magnetosphere of injected waves from the Siple Station VLF transmitter, *Journal of Geophysical Research*, *82*, 1177–1187, doi:10.1029/JA082i007p01177.

- Inan, U. S., T. F. Bell, and R. A. Helliwell (1978), Nonlinear pitch angle scattering of energetic electrons by coherent VLF waves in the magnetosphere, *Journal of Geophysical Research*, *83*, 3235–3253, doi:10.1029/JA083iA07p03235.
- Inan, U. S., T. F. Bell, and H. C. Chang (1982), Particle precipitation induced by short-duration VLF waves in the magnetosphere, *Journal of Geophysical Research*, *87*, 6243–6264, doi:10.1029/JA087iA08p06243.
- Inan, U. S., H. C. Chang, R. A. Helliwell, J. P. Katsufakis, and W. L. Imhof (1985), Wave-induced precipitation as a loss process for radiation belt particles, *Advances in Space Research*, *5*, 243–245, doi:10.1016/0273-1177(85)90146-2.
- Inan, U. S., M. Walt, H. D. Voss, and W. L. Imhof (1989), Energy spectra and pitch angle distributions of lightning-induced electron precipitation - Analysis of an event observed on the S81-1 (SEEP) satellite, *Journal of Geophysical Research*, *94*, 1379–1401, doi:10.1029/JA094iA02p01379.
- Ji, E.-Y., Y.-J. Moon, J. Park, J.-Y. Lee, and D.-H. Lee (2013), Comparison of neural network and support vector machine methods for Kp forecasting, *Journal of Geophysical Research: Space Physics*, *118*(8), 5109–5117, doi:10.1002/jgra.50500.
- Jin, G., M. Spasojevic, M. B. Cohen, U. S. Inan, and N. G. Lehtinen (2011), The relationship between geophysical conditions and ELF amplitude in modulated heating experiments at HAARP: Modeling and experimental results, *Journal of Geophysical Research*, *116*, doi:10.1029/2011JA016664.
- Katoh, Y., and Y. Omura (2006), A study of generation mechanism of VLF triggered emission by self-consistent particle code, *Journal of Geophysical Research: Space Physics*, *111*(A12), n/a—n/a, doi:10.1029/2006JA011704.
- Katoh, Y., and Y. Omura (2011), Amplitude dependence of frequency sweep rates of whistler mode chorus emissions, *Journal of Geophysical Research: Space Physics*, *116*(A7), n/a—n/a, doi:10.1029/2011JA016496.

- Katsufrakis, J. P., R. A. Helliwell, and G. James (1980), Observations of Siple transmitter signals on the ISIS satellites, *Antarctic Journal*, *XV*, 212–213.
- Kennel, C. F., and H. E. Petschek (1966), Limit on stably trapped particle fluxes, *Journal of Geophysical Research*, *71*(1), 1–28, doi:10.1029/JZ071i001p00001.
- Kimura, I. (1967), On observations and theories of the VLF emissions, *Planetary and Space Science*, *15*(9), 1427–1462, doi:10.1016/0032-0633(67)90115-8.
- Kimura, I. (1968), Triggering of VLF magnetospheric noise by a low-power (100 watts) transmitter, *Journal of Geophysical Research*, *73*(1), 445–447, doi:10.1029/JA073i001p00445.
- Kintner, P. M., R. Brittain, M. C. Kelley, D. L. Carpenter, and M. J. Rycroft (1983), In situ measurements of transionospheric VLF wave injection, *Journal of Geophysical Research*, *88*, 7065–7073, doi:10.1029/JA088iA09p07065.
- Koons, H. C., and M. H. Dazey (1983), High-power VLF transmitter facility utilizing a balloon lofted antenna, *Antennas and Propagation, IEEE Transactions on*, *31*(2), 243–248, doi:10.1109/TAP.1983.1143044.
- Koons, H. C., M. H. Dazey, R. L. Dowden, and L. E. S. Amon (1976), A controlled VLF Phase Reversal Experiment in the magnetosphere, *Journal of Geophysical Research*, *81*(31), 5536–5540, doi:10.1029/JA081i031p05536.
- Lasch, S. (1969), Unique Features of VLF Noise Triggered in the Magnetosphere by Morse-Code Dots from NAA, *Journal of Geophysical Research*, *74*, 1856–1858, doi:10.1029/JA074i007p01856.
- Li, J. D., M. Spasojevic, V. Harid, M. B. Cohen, M. Golkowski, and U. S. Inan (2014), Analysis of magnetospheric ELF/VLF wave amplification from the Siple Transmitter experiment, *Journal of Geophysical Research: Space Physics*, *119*(3), 1837–1850, doi:10.1002/2013JA019513.

- Li, J. D., V. Harid, M. Spasojevic, M. Golkowski, and U. S. Inan (2015a), Preferential amplification of rising versus falling frequency whistler mode signals, *Geophysical Research Letters*, *42*(2), 207–214, doi:10.1002/2014GL062359.
- Li, J. D., M. Spasojevic, and U. S. Inan (2015b), An Empirical Profile of VLF Triggered Emissions, *Journal of Geophysical Research*., *In Review*.
- Li, J. D., M. Spasojevic, and U. S. Inan (2015c), Predicting Conditions for the Reception of One Hop Signals from the Siple Transmitter Experiment using the Kp index, *Journal of Geophysical Research: Space Physics*, *In Review*.
- Li, W., R. M. Thorne, J. Bortnik, Y. Y. Shprits, Y. Nishimura, V. Angelopoulos, C. Chaston, O. Le Contel, and J. W. Bonnell (2011), Typical properties of rising and falling tone chorus waves, *Geophysical Research Letters*, *38*(14), n/a—n/a, doi:10.1029/2011GL047925.
- Likhter, Y. I., O. A. Molchanov, and V. M. Chmyrev (1971), Modulation of Spectrum and Amplitudes of Low-frequency Signal in the Magnetosphere Plasma, *Soviet Journal of Experimental and Theoretical Physics Letters*, *14*(8), 325.
- Matsumoto, H. (1979), Nonlinear whistler-mode interaction and triggered emissions in the magnetosphere: a review, in *Wave instabilities in space plasmas*, pp. 163–190, Springer.
- Matsumoto, H. (1985), Coherent nonlinear effects on electromagnetic wave-particle interactions, *\ssr*, *42*, 429–448, doi:10.1007/BF00214997.
- Matsumoto, H., and Y. Omura (1981), Cluster and channel effect phase bunchings by whistler waves in the nonuniform geomagnetic field, *Journal of Geophysical Research: Space Physics*, *86*(A2), 779–791, doi:10.1029/JA086iA02p00779.
- McPherson, D. A., H. C. Koons, M. H. Dazey, R. L. Dowden, L. E. S. Amon, and N. R. Thomson (1974), Conjugate magnetospheric transmissions at VLF from Alaska to New Zealand, *Journal of Geophysical Research*, *79*(10), 1555–1557, doi:10.1029/JA079i010p01555.

- Mielke, T. A. (1993), Aspects of the Magnetospheric Amplification Phenomenon in Ducted Whistler-mode Waves, Ph.d. dissertation, Stanford University.
- Mielke, T. A., and R. A. Helliwell (1992), An experiment on the threshold effect in the coherent wave instability, *Geophysical Research Letters*, *19*, 2075–2078, doi:10.1029/92GL02179.
- Mielke, T. A., and R. A. Helliwell (1993), Siple Station, Antarctica, experiments on staircase frequency ramps as approximations to continuous ramps, *Journal of Geophysical Research*, *98*, 4053–4061, doi:10.1029/92JA02562.
- Mielke, T. A., C. J. Elkins, R. A. Helliwell, and U. S. Inan (1992), Excitation of whistler mode signals via injection of polarized VLF waves with the Siple transmitter, *Radio Science*, *27*, 31–46, doi:10.1029/91RS02457.
- Newman, C. E. (1977), Theoretical study of amplitude pulsations of Key-Down whistler mode signals in the geomagnetosphere, *Journal of Geophysical Research*, *82*(1), 105–116, doi:10.1029/JA082i001p00105.
- Nunn, D. (1974), A self-consistent theory of triggered VLF emissions, *Planetary and Space Science*, *22*(3), 349–378, doi:http://dx.doi.org/10.1016/0032-0633(74)90070-1.
- Nunn, D. (1990), The numerical simulation of VLF nonlinear wave-particle interactions in collision-free plasmas using the Vlasov hybrid simulation technique, *Computer Physics Communications*, *60*(1), 1–25, doi:http://dx.doi.org/10.1016/0010-4655(90)90074-B.
- Nunn, D. (1993), A Novel Technique for the Numerical Simulation of Hot Collision-Free Plasma; Vlasov Hybrid Simulation, *Journal of Computational Physics*, *108*(1), 180–196, doi:http://dx.doi.org/10.1006/jcph.1993.1173.
- Nunn, D., and Y. Omura (2012), A computational and theoretical analysis of falling frequency VLF emissions, *Journal of Geophysical Research: Space Physics*, *117*(A8), n/a—n/a, doi:10.1029/2012JA017557.

- Nunn, D., A. G. Demekhov, V. Y. Trakhtengerts, and M. J. Rycroft (2003), VLF emission triggering by a highly anisotropic energetic electron plasma, *Annales Geophysicae*, *21*(2), 481–492, doi:10.5194/angeo-21-481-2003.
- Nunn, D., M. J. Rycroft, and V. Y. Trakhtengerts (2005), A parametric study of the numerical simulations of triggered VLF emissions, *Annales Geophysicae*, *23*(12), 3655–3666, doi:10.5194/angeo-23-3655-2005.
- Omura, Y., and H. Matsumoto (1982), Computer simulations of basic processes of coherent whistler wave-particle interactions in the magnetosphere, *Journal of Geophysical Research: Space Physics*, *87*(A6), 4435–4444, doi:10.1029/JA087iA06p04435.
- Omura, Y., and D. Nunn (2011), Triggering process of whistler mode chorus emissions in the magnetosphere, *Journal of Geophysical Research: Space Physics*, *116*(A5), n/a—n/a, doi:10.1029/2010JA016280.
- Omura, Y., D. Nunn, H. Matsumoto, and M. J. Rycroft (1991), A review of observational, theoretical and numerical studies of VLF triggered emissions, *Journal of Atmospheric and Terrestrial Physics*, *53*(5), 351–368, doi:10.1016/0021-9169(91)90031-2.
- Omura, Y., Y. Katoh, and D. Summers (2008), Theory and simulation of the generation of whistler-mode chorus, *Journal of Geophysical Research: Space Physics*, *113*(A4), n/a—n/a, doi:10.1029/2007JA012622.
- Park, C. G. (1981), Generation of whistler-mode sidebands in the magnetosphere, *Journal of Geophysical Research*, *86*, 2286–2294, doi:10.1029/JA086iA04p02286.
- Park, C. G., and D. C. D. Chang (1978), Transmitter simulation of power line radiation effects in the magnetosphere, *Geophysical Research Letters*, *5*, 861–864, doi:10.1029/GL005i010p00861.
- Park, C. G., and R. A. Helliwell (1977), Whistler precursors - A possible catalytic role of power line radiation, *Journal of Geophysical Research*, *82*, 3634–3642, doi:10.1029/JA082i025p03634.

- Park, C. G., and T. R. Miller (1979), Sunday decreases in magnetospheric VLF wave activity, *Journal of Geophysical Research*, *84*, 943–950, doi:10.1029/JA084iA03p00943.
- Paschal, E. W. (1988), Phase Measurements of Very Low Frequency Signals from the Magnetosphere, Ph.d. dissertation, Stanford University.
- Paschal, E. W. (1990), Whistler precursors on a VLF transmitter signal, *Journal of Geophysical Research*, *95*, 225–231, doi:10.1029/JA095iA01p00225.
- Paschal, E. W., and R. A. Helliwell (1984), Phase measurements of whistler mode signals from the Siple VLF transmitter, *Journal of Geophysical Research*, *89*, 1667–1674, doi:10.1029/JA089iA03p01667.
- Platino, M., U. S. Inan, T. F. Bell, M. Parrot, and E. J. Kennedy (2006), DEMETER observations of ELF waves injected with the HAARP HF transmitter, *Geophysical Research Letters*, *33*, 16,101, doi:10.1029/2006GL026462.
- Raghuram, R., R. L. Smith, and T. F. Bell (1974), VLF Antarctic antenna: Impedance and efficiency, *IEEE Transactions on Antennas and Propagation*, *22*, 334–338, doi:10.1109/TAP.1974.1140777.
- Raghuram, R., T. F. Bell, R. A. Helliwell, and J. P. Katsufakis (1977), Echo-induced suppression of coherent VLF transmitter signals in the magnetosphere, *Journal of Geophysical Research*, *82*, 2787–2796, doi:10.1029/JA082i019p02787.
- Rastani, K., U. S. Inan, and R. A. Helliwell (1985), DE 1 observations of Siple transmitter signals and associated sidebands, *Journal of Geophysical Research*, *90*, 4128–4140, doi:10.1029/JA090iA05p04128.
- Rish, I. (2001), An empirical study of the naive Bayes classifier, in *IJCAI 2001 workshop on empirical methods in artificial intelligence*, vol. 3, pp. 41–46, IBM New York.

- Sa, L. A. D. (1990), A wave-particle-wave interaction mechanism as a cause of VLF triggered emissions, *Journal of Geophysical Research*, *95*, 12,277–12,286, doi:10.1029/JA095iA08p12277.
- Sa, L. A. D., and R. A. Helliwell (1988), Structure of VLF whistler mode sideband waves in the magnetosphere, *Journal of Geophysical Research*, *93*, 1987–1992, doi:10.1029/JA093iA03p01987.
- Sazhin, S. S., and M. Hayakawa (1992), Magnetospheric chorus emissions: A review, *Planetary and Space Science*, *40*(5), 681–697, doi:http://dx.doi.org/10.1016/0032-0633(92)90009-D.
- Serra, F. M. (1984), VLF two-wave-electron interactions in the magnetosphere, *Planetary and Space Science*, *32*(8), 985–1005, doi:http://dx.doi.org/10.1016/0032-0633(84)90055-2.
- Smith, A. J., D. L. Carpenter, and M. Lester (1981), Longitudinal variations of plasmapause radius and the propagation of VLF noise within small ΔL approximately 0.5 extensions of the plasmasphere, *Geophysical Research Letters*, *8*, 980–983, doi:10.1029/GL008i009p00980.
- Smith, R. L., and J. J. Angerami (1968), Magnetospheric Properties Deduced fromOGO 1 Observations of Ducted and Nonducted Whistlers, *Journal of Geophysical Research*, *73*, 1, doi:10.1029/JA073i001p00001.
- Sonwalkar, V. S., D. L. Carpenter, R. A. Helliwell, M. Walt, U. S. Inan, D. L. Caudle, and M. Ikeda (1997), Properties of the magnetospheric hot plasma distribution deduced from whistler mode wave injection at 2400 Hz: Ground-based detection of azimuthal structure in magnetospheric hot plasmas, *Journal of Geophysical Research*, *102*, 14,363–14,380, doi:10.1029/96JA03047.
- Stiles, G. S., and R. A. Helliwell (1975), Frequency-time behavior of artificially stimulated VLF emissions, *Journal of Geophysical Research*, *80*, 608–618, doi:10.1029/JA080i004p00608.

- Stiles, G. S., and R. A. Helliwell (1977), Stimulated growth of coherent VLF waves in the magnetosphere, *Journal of Geophysical Research*, *82*, 523–530, doi:10.1029/JA082i004p00523.
- Storey, L. R. O. (1953), An Investigation of Whistling Atmospherics, *Philosophical Transactions of the Royal Society of London. Series A, Mathematical and Physical Sciences*, *246*(908), 113–141, doi:10.1098/rsta.1953.0011.
- Strauss, D. (2013), Electromagnetic Subsurface Imaging at VLF with Distributed Optimization, Ph.d. dissertation, Stanford University.
- Tao, X., W. Li, J. Bortnik, R. M. Thorne, and V. Angelopoulos (2012), Comparison between theory and observation of the frequency sweep rates of equatorial rising tone chorus, *Geophysical Research Letters*, *39*(8), n/a—n/a, doi:10.1029/2012GL051413.
- Tao, X., J. Bortnik, J. M. Albert, R. M. Thorne, and W. Li (2013), The importance of amplitude modulation in nonlinear interactions between electrons and large amplitude whistler waves, *Journal of Atmospheric and Solar-Terrestrial Physics*, *99*(0), 67–72, doi:http://dx.doi.org/10.1016/j.jastp.2012.05.012.
- Tascione, T. F. (1994), *Introduction to the Space Environment*, Orbit, a foundation series, Krieger Publishing Company.
- Trabucco, W. J., and E. W. Paschal (1978), Jupiter: A new tool for magnetospheric research, *Antarctic Journal*, *XIII*, 208.
- Trakhtengerts, V. Y., A. G. Demekhov, Y. Hobara, and M. Hayakawa (2003), Phase-bunching effects in triggered VLF emissions: Antenna effect, *Journal of Geophysical Research: Space Physics*, *108*(A4), n/a—n/a, doi:10.1029/2002JA009415.
- Vomvoridis, J. L., and J. Denavit (1979), Test particle correlation by a whistler wave in a nonuniform magnetic field, *PHYSICS OF FLUIDS*, *22*(2), 367–377, doi:10.1063/1.862589.

- Walt, M. (1994), *Introduction to geomagnetically trapped radiation*, *Cambridge Atmospheric and Space Sciences Series*, vol. 10.
- Watt, A. D. (1967), *VLF radio engineering*, International series of monographs on electromagnetic waves, Pergamon Press.
- Yue, C., C.-P. Wang, L. Lyons, Y. Wang, T.-S. Hsu, M. Henderson, V. Angelopoulos, A. T. Y. Lui, and T. Nagai (2015), A 2-D empirical plasma sheet pressure model for substorm growth phase using the Support Vector Regression Machine, *Journal of Geophysical Research: Space Physics*, *120*(3), 1957–1973, doi: 10.1002/2014JA020787.